Solubilization and Partitioning of Aroma Compounds into Short-Chain Lecithin and Nonionic Micelles Measured by Headspace Solid-Phase Microextraction

By

ANDREW PATRICK KARMAN
DISSERTATION

Submitted in partial satisfaction of the requirements for the degree of

DOCTOR OF PHILOSOPHY

in

Chemical Engineering

in the

OFFICE OF GRADUATE STUDIES

of the

UNIVERSITY OF CALIFORNIA

DAVIS

Approved:

Stephanie R. Dungan, Chair

Susan E. Ebeler

Nitin Nitin

Committee in Charge

2022

CONTENTS

LIST OF FIGURES

LIST OF TABLES

ABSTRACT OF THE DISSERTATION

In order to advance overall understanding of solubilization phenomena within micelles, this work examines the equilibrium partitioning behavior of hydrophobic aroma compounds using headspace solid-phase microextraction (HS-SPME) techniques. The first focus of this research was to develop a robust analytical method to characterize d-limonene's distribution between water and air over a 15–40˚C temperature interval. Vapor-water partition coefficients (Henry's coefficients) were evaluated for limonene in well-sealed vials representing a closed system. Through these experimental measurements, we were also able to quantify the enthalpy of volatilization of limonene. In addition, we determined the solubility concentrations of decane, limonene, and 1-octanol, which collectively spanned four orders in magnitude.

Second, HS-SPME was used to quantify micellar partitioning of limonene within aqueous mixtures containing diacyl, short-chain phosphatidylcholine with acyl chains of 6–8 carbons, as a function of temperature, solute concentration, and tail length. The three phospholipids studied were 1,2 dihexanoyl-*sn*-glycero-3-phosphocholine (diC_6PC), 1,2 diheptanoyl-*sn*-glycero-3-phosphocholine (diC_7PC), and 1,2 dioctanoyl-*sn*-glycero-3-phosphocholine (diC_8PC). By varying phospholipid concentration above the appropriate critical micelle concentration, at fixed dilute limonene concentration, the micelle partition coefficient $K_{mw} = x_{i,m}/c_{i,w}$ was evaluated using the pseudo-phase model, with $x_{i,m}$ the mole fraction of solute i within micelles and $c_{i,w}$ the solute concentration within the water continuum. Additional studies were conducted at fixed phospholipid concentration but varying limonene concentrations. For all lecithins studied, our findings show enhanced micellar

partitioning occurred with increases in tail length, but reduced with an increase in temperature. In diC_6PC or diC_7PC micellar solutions, the partition coefficient was constant at lower limonene concentrations, indicating negligible effects of non-ideal solute interactions or solute induced micellar rearrangements. However, at higher limonene concentrations, K_{mw} increased with increasing solute. The effect of limonene on the phase behavior of the longest studied short-chain lecithin, diC_8PC, was studied and it was observed that the addition of limonene resulted in the depression of diC_8PC's upper consulate temperature.

In the last focus of this dissertation, the partitioning behavior of several aroma compounds within aqueous nonionic surfactant solutions was examined. These measurements were related to a solubilization framework grounded in fundamental thermodynamic principles. It was determined that solute molecular volume alone was a strong predictor of the maximum amount of solute that could be dissolved for a given concentration of surfactant. Comparing limonene partition coefficients for various types of micelles as measured by us or reported in literature, we find that K_{mw} falls in the range of 1–6 M^{-1}, regardless of the surfactant structure. Measurements of solute vapor concentration were also used to determine the chemical potential of solute i within the micelle solution. Based on the thermodynamics of mixing, the chemical potential of studied mixtures could be related to the mole ratio of solute-to-surfactant and partition coefficient K_{mw}. For solutes limonene and octanol, the data indicated that K_{mw} was nearly constant at all molar ratios, consistent with a dilute pseudo-phase model. However, at higher mole ratios in which decane was the solute, we observed micelles lowered the chemical potential of solute below predictions of dilute theory. Thus, enhanced micellar partitioning occurred as the decane concentration was varied up to its solubility limit. Finally, through these measurements, the molar Gibbs energy of dissolution for 1-octanol, decane, and limonene was determined.

ACKNOWLEDGEMENTS

The completion of this dissertation would not have been possible without the help and support of those around me. I would like to express my sincerest gratitude to my PhD advisors, Prof. Stephanie R. Dungan, Prof. Susan E. Ebeler, and Prof. Nitin Nitin for their guidance throughout my PhD studies. In particular, I thank Prof. Dungan for helping me to articulate my thoughts in the writing of this dissertation, for her significant contributions in shaping my focus and research philosophy, and for her willingness to always listen to my ideas. Special thanks to Prof. Ebeler for introducing me to the world of analytical chemistry and for trusting me with her hard-earned equipment. Her guidance has helped me become a better experimentalist, which I will carry with me into my future career. I also appreciate the invaluable insights, unique perspective, and feedback offered by Prof. Nitin. Our weekly group meetings will be greatly missed.

I would like to thank the members of my lab groups that I was fortunate enough to have met. There was Nathan Alexander, Jennifer Staton, Penny Xu, Joel Christenson, Dorie Webley, Yiyi Li (super undergrad), Larry Lerno, Courtney Tanabe, and Mitchell McCartney. It was really inspiring to be surrounded by such talented colleagues. I also appreciate the friendship given to me by my cohort during my early years of graduate school. Additionally, I would like to express my appreciation to Prof. Phillips, Prof. Moule, and Prof. Wan for giving me the opportunity to serve as their teaching assistant during my last years at UC Davis. It was a pleasure listening to their lectures.

I am deeply indebted to members of my family and friends for their patience and emotional support throughout this journey. I thank my wife and best friend, Yazhi, my brother, Mark, my good friend, Y, and all other close family and friends. Lastly, I would like to thank my parents, Patrick and Wilawan, to whom I dedicate this research.

Chapter 1

Introduction

1.1 Overview

The presence of *aroma* compounds in food matrices, together with their release, strongly impacts our perception of flavor. Such compounds have generated considerable interest within the food industry, as knowledge of flavor-binding properties in food ingredients would allow for systematic developments in food product formulation. Moreover, key aroma compounds are known to provide important contributions to characteristic flavors appreciated by consumers. Research into solubilization of aroma compounds within micellar solutions addresses some important challenges related to flavor delivery. This dissertation explores solubilization in surfactant solutions by focusing on analytical method development, experimental data acquisition, and modeling of thermodynamic behavior of volatile compounds in vapor–liquid systems.

Incorporation of aroma compounds into food and beverages is an area of active research in the food industry. Desired attributes such as controlled release, stability, thermal protection, and suitable sensory profiles are frequently made possible through state of the art microencapsulation technologies (Đorđević et al., 2014). Spray drying, microgels, and emulsions fall under this domain and represent some of the most well-known delivery systems for nutrients and bioactive compounds. Emulsions, for example, are especially useful for the in the entrapment of polyphenols and essential oils. Here, food grade surfactants stabilize the interfacial layer between encapsulated compound and the surrounding solvent phase. Examples of food grade surfactants include sorbitans, polysorbates,

sucrose esters, and soybean lecithin. Common foods, including mayonnaise, ice cream, and milk, contain oil droplets dispersed within an aqueous phase and are therefore examples of O/W (oil-in-water) emulsions. Conversely, W/O (water-in-oil) emulsions are also seen in foods such as butter. Emulsions are considered only to be kinetically stable, as they will eventually phase separate in time.

As an alternative to emulsions, micelle-containing solutions are used to host aroma compounds in aqueous mixtures. Micelles are thermodynamically stable aggregates composed of surfactant monomers with overall sizes of 1–10 nm which form at surfactant concentrations beyond their critical micelle concentration (cmc). Formation is attributed to the amphiphilic nature of these surfactant structures: they self-assemble spontaneously to form micellar aggregates, driven primarily by the need to minimize the hydrophobic effect between surfactant tails and water. Once formed, micelles provide a thermodynamically favorable domain in which hydrophobic solutes may reside. If dissolved in water, for example, the oily interior of micelles can host other hydrophobic compounds in a process known as micellar solubilization.

Progressive solubilization of solute causes micelles to swell to an oil-swollen micelle, with further incorporation leading eventually to formation of a microemulsion. A microemulsion comprises a one phase mixture of two immiscible liquids that are stabilized by surfactants in the form of tiny droplets. These droplets have interfaces which are much more highly curved than those in emulsions. Advantages of microemulsions over emulsions include enhanced stability, optically clear solutions, and low input energy requirements for mixture formation. These advantages pertain as well to oil-swollen micellar solutions. In addition to acting as delivery vehicles that control kinetics of solute transport, microemulsions and micelles provide enhanced solubility and can protect the solute droplet from the surrounding solvent, where reactions such as lipid oxidation may degrade the compound. Furthermore, the addition of micelles and/or formation of microemulsion droplets can dramatically

shift the equilibrium distribution of solutes in multi-phase systems. Such shifts can radically alter the perception of flavor in food systems.

Development of analytical methods to measure solute distribution of aroma compounds in micelle-forming solutions allows for comparison of surfactant solubilization properties. Method choices include fluorescence spectroscopy, NMR, ultracentrifugation, vapor pressure, solubility, and chromatographic methods. A review of some of the approaches are given in the sections below. The selection of the method is largely driven by the system of interest, and vapor pressure type measurements are especially well-suited for aroma compounds. These measurements can be taken *in situ*, without the need to disturb chemical equilibrium, and do not require special properties of solute apart from measurable volatility. The method used in the approach taken in this dissertation, headspace solid phase micro-extraction (HS-SPME), falls under this category.

Solute distribution between vapor and liquid, as measured by vapor pressure methods, is frequently characterized through the aid of a vapor-liquid partition coefficient. A general strategy is to first relate the vapor pressure to its vapor concentration and to subsequently calculate the solute remaining in liquid via a total mole balance. The vapor-liquid partition coefficient is calculated as the ratio of vapor concentration to liquid concentration. Using methods developed in this lab, in Chapter 2 we discuss application of HS-SPME to capture the temperature dependencies associated with vapor-liquid partitioning. In doing so, we develop a technique for measuring the enthalpy of volatilization for the solute limonene.

Some researchers have used HS-SPME to measure aroma in the presence of a micellar solutions or other model food systems (Philippe et al., 2003; Yang et al., 2010). In these studies, the authors have essentially treated the system as pseudo-binary, in which a single "effective" partition coefficient was used to describe the solute distribution between vapor and the entire aqueous matrix with the given concentration of surfactant and/or other components. A focus of this dissertation is to move

away from such "try-and-see" approaches. As presented in Chapters 3 and 4, we quantify local solute distributions within the micellar solution using a micelle-liquid partition coefficient. The role that solute and surfactant concentration, structure, and temperature effects, have on the micelle-liquid partition coefficient is explored.

1.2 Thermodynamics of Vapor-Liquid and Micelle-Liquid Partitioning

1.2.1 Vapor-Liquid Equilibria

A well-known criterion for closed, multi-component systems is that the Gibbs free energy (G) is minimized at equilibrium. This minimization is attained through the system's adjustments to its composition until the chemical potential, μ, is equal between all phases. Thus, for constant temperature (T) and pressure (p),

$$\begin{pmatrix} \mu_{i,\alpha} = \mu_{i,\beta} = & \cdots & = \mu_{i,\phi} \\ \mu_{j,\alpha} = \mu_{j,\beta} = & \cdots & = \mu_{j,\phi} \\ \vdots & & \vdots \\ \mu_{k,\alpha} = \mu_{k,\beta} = & \cdots & \mu_{k,\phi} \end{pmatrix}_{T,p} . \tag{1.1}$$

In the above, the first subscript on μ indicates the identity of the component while the second subscript indicates the identity of phase. By definition, $\mu_i = (\partial G/\partial n_i)_{T,p,n_j \ldots n_k}$, which represents the change in the Gibbs free energy with respect to the change in number of moles of component i (n_i). The chemical potential, while abstract, is useful for relating physically measurable quantities such as temperature, pressure, and composition. Chemical potentials are generally evaluated with respect to a chosen reference point, commonly denoted as a standard state. We will here obtain insight in μ_i using classical thermodynamics.

Consider a pure and ideal gas. Its chemical potential is related to temperature and pressure by the differential equation:

$$d\mu = -sdT + \vartheta dp, \tag{1.2}$$

where s and ϑ are the molar entropy and volume of the substance, respectively. Differentiating the above with respect to pressure for an isothermal change gives

$$\left(\frac{\partial \mu}{\partial p}\right)_T = \vartheta. \tag{1.3}$$

For an ideal gas, $\vartheta = \frac{RT}{p}$, and so substitution and integration at constant temperature gives

$$\mu - \mu^o = RTln\frac{p}{p^o}, \tag{1.4}$$

where μ^o represents a generalized standard chemical potential at standard state pressure (p^o). In effect, Equation (1.4) describes the change in chemical potential for one mole of pure gas from pressure p^o to p. The choice of standard state is often picked as a matter of convenience depending on the system of interest.

Similar expressions to Equation (1.4) are also obtained for ideal gas and ideal solution *mixtures*. If the entropy of mixing is considered, one obtains

$$\mu_{i,v} - \mu_{i,v}^o = RTln\frac{p_i}{p_i^o} \tag{1.5}$$

for component i in a vapor mixture (v) and

$$\mu_{i,w} - \mu_{i,w}^o = RTlnx_{i,w}. \tag{1.6}$$

for solute i in a liquid solvent (w). These expressions can be derived using a lattice model as discussed by Dill and Bromberg (2011). In Equations (1.5) and (1.6), p_i and $x_{i,w}$ represent the partial pressure and solvent mole fraction of component i, respectively.

Next, we consider the situation in which gas and liquid mixtures are combined within a closed system. Here, various amounts of solute i are mixed with a solvent and placed into a closed system containing air. Assume that the solute and solvent are completely miscible at all concentrations and

that the gas behaves ideally. If partial pressures were measurable, two important limiting cases would emerge. At solute mole fractions in the liquid near unity, experimental measurements would show that $p_i = p_i^* x_{i,w}$, where p_i^* is the partial pressure of i above pure solute. Moreover, at very dilute solute concentrations one would find $p_i = K_{px} x_{i,w}$, where K_{px} is a version of the Henry's constant.[*] These two equations are known as Raoult's law and Henry's law, respectively. An example figure showcasing this scenario is provided in Figure 1.1 below. The solid black curve represents true partial pressures of solute, the dotted line describes changes in partial pressure as extrapolated from the infinitely dilute limit, and the dashed line represents ideality.

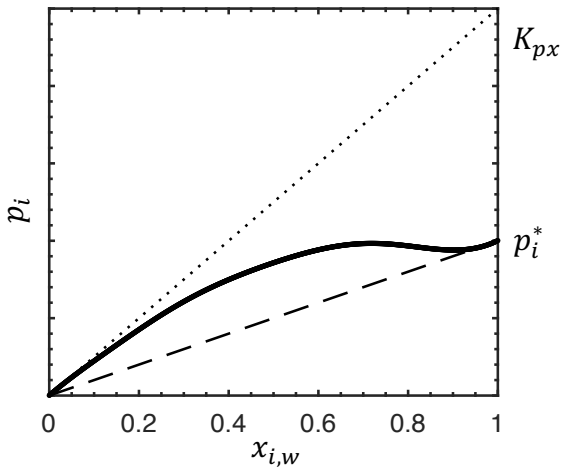

Figure 1.1. Partial pressures as a function of solute mole fraction in a binary solution

Figure 1.1 demonstrates that the choice of reference states depends on the region of interest. If operating in the ideal-dilute limit, then it is convenient to choose a reference state chemical potential defined as that obtained in the limit when $\lim_{x_{i,w} \to 1} p_i = K_{px}$. However, in the solute-rich region where solution ideality is expected, then one should choose $\lim_{x_{i,w} \to 1} p_i = p_i^*$.

[*] There is no uniformly agreed upon unit convention for the Henry's constant. Depending on the research field, the Henry's constant may have units of dimensionless concentration, dimensionless mole fraction, pressure, or inverse pressure (Smith and Harvey, 2007).

Solution mixtures are rarely ideal, meaning that they do not obey Raoult's law for all components over the entire range of compositions. Instead, Equation (1.6) is often used for modeling solute behavior in ideal-dilute solutions. By referencing its *infinitely dilute* chemical potential, $\mu_{i,w}^{\ominus}$, changes in the solute chemical potential with changes in mole fraction $x_{i,w}$ are captured solely by the effects of entropic mixing. That is,

$$\mu_i - \mu_{i,w}^{\ominus} = RTlnx_{i,w}. \tag{1.7}$$

In other words, the addition of solute in a dilute system results in negligible enthalpic contributions compared to those at infinite dilution. Here $\mu_{i,w}^{\ominus}$ captures the chemical potential of i in an infinite bath of solvent.

Having developed some physical intuition for the necessity of different reference states and how they are chosen, we can now develop a useful mathematical relationship between K_{px} and the chemical potential. Returning to the case of solute in a closed system, suppose pure liquid solute is allowed to equilibrate with surrounding air. By Equation (1.1)

$$\mu_{i,w}^{*} = \mu_{i,v}^{*}, \tag{1.8}$$

where $\mu_{i,w}^{*}$ and $\mu_{i,v}^{*}$ indicates the chemical potential of i in pure liquid solute and in saturated air, respectively. Thus,

$$\mu_{i,w}^{*} = \mu_{i,v}^{*} = \mu_{i,v}^{o} + RTln\frac{p_i^{*}}{p_i^{o}}. \tag{1.9}$$

As will be shown, it turns out the above equilibrated, saturated mixture makes for a convenient reference system. Next, consider component i in a gas mixture in equilibrium with a liquid solution, with a chemical potential $\mu_{i,w}$. Then,

$$\mu_{i,w} = \mu_{i,v} = \mu_{i,v}^{o} + RTln\frac{p_i}{p_i^{o}}. \tag{1.10}$$

Here, p_i again represents the partial pressure of solute in vapor above the liquid mixture. In Equation (1.10), the asterisk has been dropped since the liquid is no longer pure. Note that the chemical potential standard state used in Equations (1.9) and (1.10) was deliberately chosen to be the same, as they are defined with respect to the same p_i^o. Thus, Equation (1.10) becomes

$$\mu_{i,w} = \mu_{i,v} = \left\{\mu_{i,v}^* - RTln\frac{p_i^*}{p_i^o}\right\} + RTln\frac{p_i}{p_i^o}, \tag{1.11}$$

which simplifies to

$$\mu_{i,w} = \mu_{i,v} = \mu_{i,v}^* + RTln\frac{p_i}{p_i^*} = \mu_{i,w}^* + RTln\frac{p_i}{p_i^*}, \tag{1.12}$$

since $\mu_{i,v}^* = \mu_{i,w}^*$.

If the solution may be treated as ideal-dilute, Equation (1.7) is a valid form for $\mu_{i,w}$. Equating Equations (1.7) and (1.12) yields

$$\mu_{i,w}^* + RTln\frac{p_i}{p_i^*} = \mu_{i,w}^{\ominus} + RTlnx_{i,w}. \tag{1.13}$$

Noting that $p_i = K_{px}x_{i,w}$ at the Henry's limit and substituting this relation into the above equation yields

$$\mu_{i,w}^* + RTln\frac{K_{px}x_{i,w}}{p_i^*} = \mu_{i,w}^{\ominus} + RTlnx_{i,w}. \tag{1.14}$$

Solving for K_{px} gives finally

$$K_{px} = p_i^* \exp\left(\frac{\mu_{i,w}^{\ominus} - \mu_{i,w}^*}{RT}\right). \tag{1.15}$$

Measurements of K_{px} are discussed in Chapter 2. Equation (1.15) then allows for determination of the chemical potential difference $\Delta\mu^{ref} = \mu_{i,w}^{\ominus} - \mu_{i,w}^*$, which represents the chemical potential change for i in moving from pure solute to infinite dilution in the solvent. This difference $\Delta\mu^{ref}$ is also referred to as the molar Gibbs energy of dissolution.

1.2.2 Micelles and the Pseudo-phase Model

The pseudo-phase model is often used for modeling solute partitioning in micellar solutions since it provides useful simplifications for analysis. Here, the aggregate structures are treated as a collective; a single partition coefficient is used to describe partitioning of solute between micelles and the surrounding aqueous continuum. In addition, the micelle collective is treated as a "pseudo-phase". In doing so, micelle structure, micelle-micelle interactions, and micelle entropy of mixing are not explicitly accounted for in the analysis. Instead, the surfactants in micelles are treated as distinct phase, much like a bath of surfactant.

Following this, the chemical potential of solute in liquid $(\mu_{i,w})$ or within micelles $(\mu_{i,m})$ takes on the form given by Equation (1.7). That is,

$$\mu_{i,w} = \mu_{i,w}^{\ominus} + RTln\varphi_{i,w}x_{i,w} \quad ; \quad \mu_{i,m} = \mu_{i,m}^{\ominus} + RTln\varphi_{i,m}x_{i,m}. \tag{1.16}$$

In the above, $\mu_{i,m}^{\ominus}$ represents the ideal-dilute reference potential of solute in an infinitely large bath of pure surfactant. $\varphi_{i,w}$ and $\varphi_{i,m}$ are activity coefficients of solute in liquid and within micelles, respectively. These coefficients account for non-ideality of mixing, which may occur at non-dilute amounts of solute within each domain. Lastly, $x_{i,m} = \frac{n_{i,m}}{n_{i,m}+n_{s,m}}$ represents the mole fraction of solute within micelles, with $n_{i,m}$ and $n_{s,m}$ the moles of solute i and surfactant, respectively. Thus, for $\mu_{i,w} = \mu_{i,m}$, we have

$$\mu_{i,w}^{\ominus} + RTln\varphi_{i,w}x_{i,w} = \mu_{i,m}^{\ominus} + RTln\varphi_{i,m}x_{i,m}. \tag{1.17}$$

Equation (1.17) may also be rearranged to yield

$$\widehat{K}_{mw} = \frac{x_{i,m}}{x_{i,w}} = \frac{\varphi_{i,w}}{\varphi_{i,m}} \exp\left(\frac{\mu_{i,w}^{\ominus} - \mu_{i,m}^{\ominus}}{RT}\right), \tag{1.18}$$

where $\widehat{K}_{mw}$ represents a dimensionless distribution coefficient that characterizes the mole fraction of solute within micelles relative to that in the liquid.

Equation (1.18) provides useful insight for understanding micellar partitioning. It shows that even if the solute is ideal-dilute in each phase, such that $\varphi_{i,w}$ and $\varphi_{i,m}$ are unity, one should still expect a distribution of solute between micelles and liquid, so as long as $\mu_{i,w}^{\ominus} - \mu_{i,m}^{\ominus}$ is finite. In this case, the distribution would be independent of solute concentration. More generally, concentration effects in micelles are also captured by Equation (1.18). While hydrophobic solutes cannot appreciably dissolve in aqueous solvent (and are thus highly dilute, with $\varphi_{i,w} \approx 1$), substantial quantities of solute relative to surfactant in micelles are feasible. As progressively more solute is solubilized, solute-solute interactions within micelles may become more substantial so that $\varphi_{i,m} = f(x_{i,m})$. In Chapter 3, we examine this possibility further in systems containing short-chain phospholipids and limonene.

1.2.3 Other Theories for Thermodynamics of Micellar Solubilization

The thermodynamics of micellar solubilization behavior has been treated in depth by Nagarajan and Ruckenstein (1991) and by Puvvada and Blankschtein (1992). Contributions to the free energy of micellization, both with and without solute, were carefully examined by both groups. Both groups modeled solubilization by first examining a solute-free micellar solution and subsequently extended their theories to accommodate solutes. In a system containing only surfactant and water, in dynamic equilibrium above the cmc, the chemical potential of a singly dissolved surfactant monomer in water $(\mu_{s,w})$ is set equal to the chemical potential of a surfactant monomer in a micelle composed of g surfactant monomers (μ_g). That is, $\mu_{s,w} = \mu_g/g$. Thus, through Equation (1.7), one obtains (Tanford, 1973)

$$\mu_{s,w}^{\ominus} + kTlnx_{s,w} = \frac{1}{g}\left(\mu_g^{\ominus} + kTlnx_g\right), \tag{1.19}$$

where $\mu_{s,w}^{\ominus}$ and $\mu_g^{\ominus}$ are the infinitely dilute chemical potentials of a dissolved surfactant monomer free in water and the collective of monomers in a micelle of size g at infinite dilution, respectively. $x_{s,w}$ and x_g represent the mole fractions of dissolved free monomer in water and of micelles of size g, respectively. Rearrangement of Equation (1.19) yields

$$x_g = x_{s,w}^g \exp\left(-\frac{\mu_g^{\ominus} - g\mu_{s,w}^{\ominus}}{kT}\right) = x_{s,w}^g \exp\left(-\frac{g\Delta\mu_g}{kT}\right), \tag{1.20}$$

where $\Delta\mu_g = \mu_g^{\ominus}/g - \mu_{s,w}^{\ominus}$ is the chemical potential change between a free surfactant monomer and one aggregated within a micelle of size g, in an infinite bath of solvent.

A similar expression is developed when accounting for the possibility of dissolved solute. In this case, dynamic equilibrium between dissolved monomer, molecularly dissolved solute, and solute-containing micelles requires that $\mu_{gj} = g\mu_s + j\mu_i$, where μ_s and μ_i are the chemical potentials of surfactant and solute molecules, respectively, and μ_{gj} is the chemical potential of a micelle containing g surfactants and j solutes. The extension of Equation (1.19) is therefore

$$g(\mu_{s,w}^{\ominus} + kTlnx_{s,w}) + j(\mu_{i,w}^{\ominus} + kTlnx_{i,w}) = \mu_{gj}^{\ominus} + kTlnx_{gj}, \tag{1.21}$$

yielding the distribution

$$x_{gj} = x_{s,w}^g x_{i,w}^j \exp\left(-\frac{\mu_{gj}^{\ominus} - g\mu_{s,w}^{\ominus} - j\mu_{i,w}^{\ominus}}{kT}\right). \tag{1.22}$$

Here, x_{gj} is the mole fraction of micelles containing g surfactants and j solubilizates, $x_{i,w}$ is the mole fraction of free solute in liquid, $\mu_{gj}^{\ominus}$ is the infinitely dilute chemical potential of a gj micelle, and $\mu_{i,w}^{\ominus}$ is the infinitely dilute chemical potential of a free solute. From Equation (1.22) and knowledge of the total amount of solute in the micelle solution, the distribution of solute within micelles of various compositions and free solute in dissolved form can potentially be determined.

Nagarajan and Ruckenstein (1991) and Puvvada and Blankschtein (1992) expressed $\Delta\mu_{gj}$ as the sum of various thermodynamic contributions including the transfer free energy of surfactant tails, surfactant tail deformation, aggregate core-liquid interfacial free energy, steric and electrostatic headgroup interactions, and surfactant-tail solubilizate mixing free energy. Subsequent papers from both groups developed theories and computational approaches to predict these contributions for any solute added to a surfactant solution of interest (Iyer et al., 2013; Nagarajan, 2017; Nagarajan and Ruckenstein, 2000; Stephenson et al., 2007).While these methods provide a useful technical framework for understanding the associated complexities of solubilization phenomena, they are difficult to implement due to the large requirement of physical data for solute and surfactant as input parameters. Further work is needed to quantitatively predict $\Delta\mu_{gj} = \mu_{gj}^{\ominus} - g\mu_{s,w}^{\ominus} - j\mu_{i,w}^{\ominus}$ and thereby the distribution of solute inside and outside the micelles *a priori*. The HS-SPME measurements described in this dissertation may prove helpful in this effort, by providing experimental results for solute partitioning and solute chemical potentials within various surfactant solutions.

1.3 Experimental Methods for Measuring Micelle-Liquid Partitioning Equilibria

A major focus of this dissertation involves the experimental acquisition of micelle-liquid partition coefficients using solid-phase microextraction techniques. In this section we review a variety of other experimental methods used to evaluate partitioning behavior of hydrophobic solutes in micellar solutions. These approaches often make use of the pseudo-phase model previously described in §1.2.2. A summary of additional methods not discussed in this dissertation is available in the *Handbook of Surface and Colloid Chemistry* (Høiland and Blokhus, 2009).

1.3.1 Total Solubility

A classic approach used for obtaining micelle-liquid partition coefficients involves measuring the total solubility of a compound in an aqueous solution for a given amount of surfactant (Abe et al., 1992; Saito et al., 1993; Tokuoka et al., 1995, 1992). Here, successive increments of solute are added to a surfactant solution until the solubility limit is reached. Upon each increment of solute, the solution is sealed and allowed to equilibrate for a period ranging from several hours to a few days. The solubility concentration is most commonly detected via spectrophotometric light transmittance measurements (Abe et al., 1992; Tokuoka et al., 1994) or by visual inspection (Saito et al., 1993), but use of other devices, such as a total organic content analyzer, have also been reported (Tokuoka et al., 1992).

Acquiring partitioning data via solubility measurements can be done easily and for various types of solutes (Høiland et al., 1984; Jabbari and Teymoori, 2018). Given that there are few consumable expenditures, these measurements are relatively low cost. Thus, this method appears suitable for gaining a preliminary understanding of the micellar system. Indeed, many studies which utilize solubility measurements are paired with results using other experimental devices so as to develop a more complete understanding of solubilization behavior. Drawbacks of the solubility measurement include low accuracy and the inability to measure potential concentration effects associated with micellar partitioning. Many older studies cite data from solubility approaches, but modern literature typically relies on more sophisticated methods.

1.3.2 Chromatographic Methods

High-performance liquid chromatographic separations can provide another pathway for studying solute partitioning (Armstrong and Nome, 1981; Arunyanart and Cline Love, 1984). Here, a micellar solution is used as the mobile phase, which is passed through the column at a fixed flowrate. Once steady flow is established, a small quantity of solute is introduced to the column's entrance. As the solute is transported through the column, the solute is assumed to rapidly partition between the

micelles within the solution, the surrounding solvent, and the column's stationary phase. Armstrong and Nome (1981) modeled these partitioning equilibria using three partition coefficients, as illustrated in Figure 1.2 below. Their analysis established a linear dependence between surfactant concentration in the mobile phase and the inverse retention factor. The latter term is a quantity that is related to the amount of time solute travels through the column relative to that for the mobile phase. If these parameters are plotted together, the resulting slope could be used to determine a micelle-liquid partition coefficient.

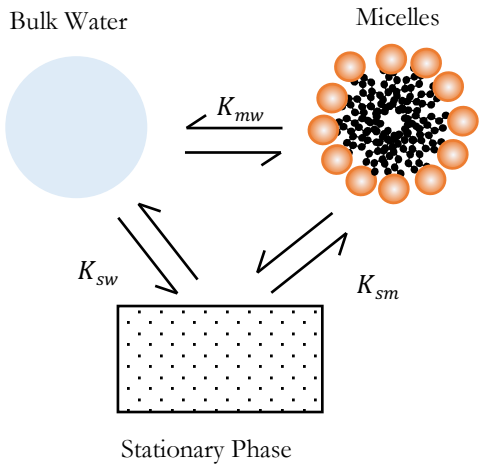

Figure 1.2. The three-phase model used for micellar chromatography. K_{mw} is the partition coefficient between micelles and water, K_{sm} is the partition coefficient between stationary phase and micelles, and K_{sw} is the partition coefficient between stationary phase and water

Liquid chromatography is well-suited for obtaining micelle-liquid partition coefficients obtained for non-volatile compounds. It is often utilized because it can quickly and quantitatively evaluate partition coefficients for a wide variety of solutes. Common challenges include long elution times and broad asymmetrical peak shape from the detector (Peris-García et al., 2018). These issues have been partially addressed by modifying the water continuum to include small quantities of organic solvent (Peris-García et al., 2018) or use of mixed micellar solutions (Duan et al., 2020); both of these modifications fundamentally change the nature of the sample matrix. Peris-García et al. (2018)

observed larger uncertainties for micelle-water partition coefficients obtained from particularly hydrophobic solutes. Strong multicomponent effects for solute transport in micellar solutions have been reported on elsewhere (Alexander et al., 2021, 2019), which would need to be accounted for in analyzing the chromatographic data. If paired with a UV-vis detector, the absorption spectra of surfactant should not overlap with the solute. Finally, generally large quantities of micellar solution must also be utilized, which results in higher costs.

1.3.3 Vapor Pressure

Vapor pressure techniques are useful for measuring partitioning of volatile compounds. A noteworthy advantage of this approach is that any solute concentration dependencies of K_{mw} are readily identified. This is due to the simple fact that measurements can be accurately made below the solubility limit and thus a range of concentration behaviors may be evaluated. The samples can be measured without disturbing chemical equilibrium. As will be discussed below, a few variations of this technique exist within the literature, but in all cases the premise relies on measuring solute vapor concentration against total added solute in a closed system. Doing so yields a solubilization isotherm.

Tucker et al. (1982) used a customized vapor pressure apparatus to automatically dispense precise amounts of solute into a vessel of known vapor volume, liquid volume, and surfactant concentration, and containing only solute, water, and surfactant. Additions of small amounts of solute were quantified using an attached manometer that provided readouts of resulting changes in vapor pressure, which would stabilize once final equilibration was achieved. Afterwards, the measurements could be compared with the vapor pressure of a reference standard. The reference was, in turn, typically prepared in one of two ways: (1) by constructing an entire reference solubilization isotherm from samples without surfactant, but otherwise identically prepared, with measurements above the solute solubility limit or (2) measurements on a sample containing pure solute only. The relative merits for these choices of reference state are described by Tucker et al. (1985,1982).

Other experimental approaches using solute vapor pressure to measure partitioning into micelles involve physically sampling small quantities of solute from the headspace that is in equilibrium with the sample. For instance, static headspace sampling uses a gas-tight syringe to remove volatile compounds in the vapor phase above a micellar solution (Vane and Giroux, 2000). The extracted sample is typically quantified using gas chromatography methods. A second approach exposes a single microdroplet to the headspace (Yao et al., 2010). In this case, the microdroplet contains surfactant which acts as an 'extracting solvent', whereby the gaseous solute above a micellar solution will partition into the microdroplet. The droplet is subsequently deposited into a secondary extracting solvent, and the droplet composition is then quantified by liquid chromatography.

The approach taken in this dissertation research is to use a SPME fiber to sample the headspace above a surfactant-containing solution. The fiber acts as an extraction phase which consists of a polymeric organic, viscoelastic material that is cross-linked and permanently attached to a thin rod as shown in Figure 1.3. The rod is typically an optical fiber of fused silica that has a diameter of 100–200 micrometers and is chemically inert (Pawliszyn et al., 1997). The polymeric film has thickness of 10–100 microns. Two common polymers are poly(dimethylsiloxane) (PDMS) and polyacrylate (PA). PDMS, a liquid-like phase, results in a much more rapid extraction when compared with PA. SPME has been successfully used to study micellar partitioning and solubilization by direct immersion of the fiber into the sample (Pino et al., 2007, 2004) or by headspace sampling techniques (Baek et al., 2003; Lloyd et al., 2011b). By extracting from the headspace, we avoid potential complications associated with fiber swelling and/or rapid degradation of the fiber caused by contact with the liquid. However, our method is restricted to volatile solutes that should not degrade when injected to the hot GC inlet.

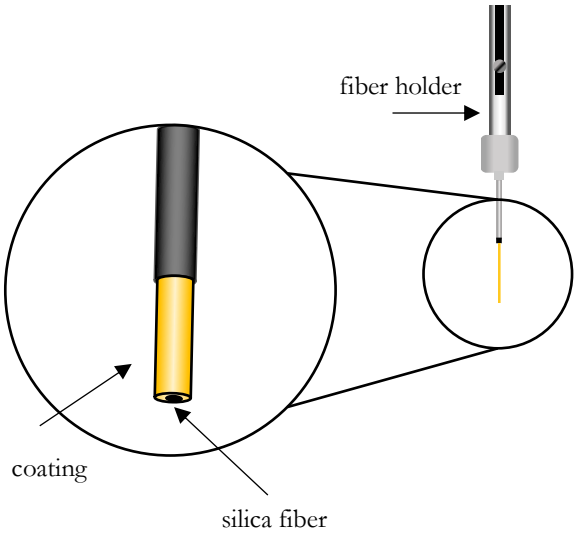

Figure 1.3. Illustration of a representative SPME fiber

1.4 Properties of Short-Chain Phospholipids

Phosphatidylcholines (PC) are a class of phospholipid comprising a zwitterionic "head" group and two acyl chain "tails". They are composed of a *sn-glycerol-3-phosphate* backbone, in which the C_1 and C_2 positions have been esterified by fatty acids and the phosphoryl group is attached to a choline residue. This molecular structure classifies these molecules as surfactants, capable of self-assembling as aggregates of varying sizes and structures. In animal cells, PC molecules normally contain tail lengths of 14–24 carbons and can be either saturated or unsaturated (Alberts et al., 2002). They are also found in plant-based oils, such as those derived from sunflower seeds, soybeans, and rapeseed (Brady, 2013). With long chain lengths, PC obtained from these natural sources will tend to pack together as a bilayer, minimizing the structured water formation around the tails that occurs when placed into an aqueous environment. Due to their amphiphilic nature, PCs are widely used in the food industry as emulsifiers, such as in the preparation of mayonnaise and baked products containing eggs (Brady, 2013).

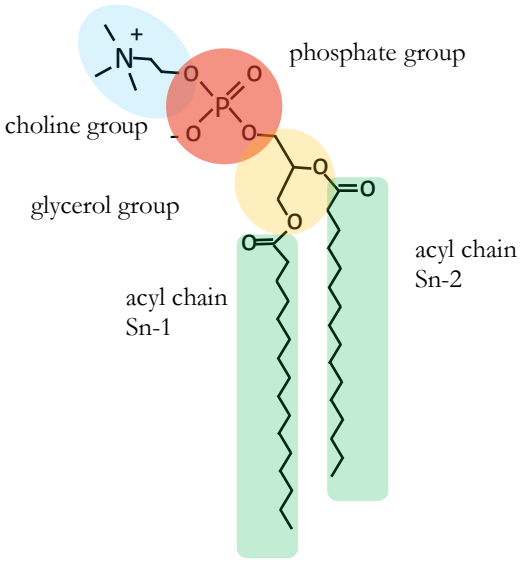

Figure 1.4. Molecular structure of phospholipid

Commercially available lecithin† obtained from natural sources are limited in their variety of fatty acid tails and, as such, there is interest in the development of new methods to create changes in phospholipid chemical composition for increased dietary and nutritional value purposes (Chojnacka et al., 2012, 2009; Zhao et al., 2014). In egg yolk PCs, composition can be tailored through isolation and subsequent chemical or enzymatic modifications. The former of these two has been used for synthesizing "short-chain" lecithin PCs with saturated tail lengths between 5–9 carbons in length (De Haas et al., 1971; Tausk and Overbeek, 1974). For example, Tausk and Overbeek (1974) synthesized short chain lecthin by first purifying egg yolk lecithin, and subsequently hydrolyzed these natural long-chain lecithin via tetrabutylammonium hydroxide. The *sn-glycerol-3-phosphate* backbone was then esterified with the appropriate acid anhydride of desired chain length.

When dissolved in water, these short chain PCs form micelles rather than bilayers. Determination of the critical micelle concentration of these short-chain lecithin in aqueous solution has been carried out using light scattering, ultrafiltration, calorimetry, and small-angle neutron scattering techniques.

† The term lecithin is often used interchangeably with phosphatidylcholine for historical reasons.

Results from a review of cmc data from Hauser (2000) are shown in Table 1.1 below (Hauser, 2000). For short-chain PCs with two identical tail lengths, the naming convention follows diC_nPC, where n denotes the number of carbons in each acyl chain. The data provided in the table shows that the cmc decreases by approximately one order of magnitude as the tail length is increased by one methylene unit.

Changes in PC chain length are also of importance in governing micelle shape and size. Information on the micellar structure of diC_6PC and diC_7PC was obtained by neutron scattering methods by Eastoe et al. (1998) and Lin et al. (1990, 1986, 1987). These studies showed that diC_6PC likely forms prolate ellipsoids with an aspect ratio of ~2 and this shape is relatively insensitive to changes in total surfactant concentration. In contrast, diC_7PC forms at low concentrations rod-like micelles that grow axially with increased surfactant concentration or decreased temperature (Lin et al., 1990, 1987). Tausk and Overbeek (1974) findings from ultracentrifugation and light scattering methods were consistent with these interpretations for both phospholipids. They found that the weight-average micellar weight, $\langle M_W \rangle$, for diC_6PC was 14–15×10^3 g/mol, which only slightly decreased with micelle concentration. Conversely, $\langle M_W \rangle$ for diC_7PC micelles monotonically increased from ~80×10^3 g/mol as concentration was varied between 1 and 20 mg/mL. DiC_8PC mixtures phase-separate into surfactant-rich and surfactant-poor phases at PC concentrations just beyond the cmc, which is ~0.14 mg/mL at room temperature (Tausk and Overbeek, 1974). Micelles in the surfactant-rich phase have been characterized as "wormy", likely existing as either an interconnected network (Nostro et al., 2008; Tausk et al., 1974b) or as an entanglement of elongated micelles (Blankschtein et al., 1986).

Table 1.1. Critical micelle concentrations of short-chain PCs in H_2O (Hauser, 2000)

Critical micelle concentration (cmc)								Experimental Conditions	Source
$diC_6PC \cdot H_2O$		$diC_7PC \cdot H_2O$		$diC_8PC \cdot H_2O$		$diC_9PC \cdot H_2O$			
mg/mL	mM	mg/mL	mM	mg/mL	mM	mg/mL	μM		
6.9	14.6	0.71	1.42	0.14	0.27	0.016	28.8	10^{-2}M Phosphate Buffer, pH 6.9	(Tausk and Overbeek, 1974)
6.5	13.8	0.80	1.60	0.13	0.25	—	—	10^{-2}M Phosphate Buffer, pH 6.9	(Tausk and Overbeek, 1974)
6.5	13.8	0.90	1.8	0.10	0.19	—	—	0.5 mM Tris pH 6.5, 0.1M NaCl, 10mM $CaCl_2$	(De Haas et al., 1971)
7.54	16±2	—	—	—	—	—	—	H_2O, 25°C	(Johnson et al., 1981)
7.2	15.2	—	—	—	—	—	—	^2H_2O, pH≈6	(Hauser et al., 1980)
5.2	11.0	—	—	—	—	—	—	0.5 mM Tris pH 8, 0.01 M NaCl	(Roholt and Schlamowitz, 1961)
—	—	0.90	1.8	—	—	—	—	0.01 M, room temperature	(Bonsen et al., 1972)
7.2	15.2		—	—	—	—	—	H_2O	(T. L. Lin et al., 1986)

Studies of short-chain lecithin have previously garnered interest among biochemists as they were often utilized as analogues for modeling the fundamental biological processes seen with their longer chain counterparts. These include examinations of enzyme kinetics (De Haas et al., 1971; Gabriel and Roberts, 1987), lipid conformation and mobility (Burns et al., 1981), and solubilization of cholesterols and triglycerides (Burns et al., 1983; Ramon A Burns and Roberts, 1981a, 1981b). Of relevance to this work were the solubilization studies, in which short-chain lecithins were found to be effective detergents. In Burn and Roberts (1981a), aqueous solutions of diC_7PC were found to solubilize greater amounts of crystalline cholesterol, when compared with egg PC sonicated vesicles. In addition, the activity of cholesterol oxidase was 25-fold higher in micelles as compared to in vesicles. The relationship between the tail length and the extent of solubilization was also examined. Burns et al. (1981a,1983) determined triglycerides or cholesterol could be dissolved in a greater extent in micelles with longer short-chain lecithin tails. In Chapter 3, we compare their results on triglycerides with our own studies involving short-chain PCs and d-limonene. We find many of the trends reported in these works are consistent with our own investigations.

1.5 Summary of Objectives

The objective of this dissertation was largely centered on developing experimental SPME methods to probe equilibrium aroma distributions in vapor-liquid systems. First, we calculated vapor-liquid partition coefficients for limonene-water mixtures in contact with air for the temperature interval of 15–40°C. These values were assessed using an error analysis developed by Lloyd et al. (2011a) and the coefficients were then used to calculate limonene's enthalpy of volatilization. In addition, we also determined the aqueous solubility limit of decane, 1-octanol, and limonene. The outcome of these results is presented in Chapter 2.

A second goal of our work was the characterization of solubilization properties for a series of short-chain lecithin, in which limonene was used as the model aroma compound. Trends in micelle-water partition coefficients were established as a function of temperature, solute concentration, and phospholipid tail length. In all cases, the micelle-water partition coefficient increased with increasing solute concentration. It is likely that this shift is the result of increases in favorable solute-solute interactions. In addition, phase behavior of diC_8PC in the presence of limonene was explored. It was found that the upper consulate temperature was lowered as a direct result of added limonene. Details of these studies are provided in Chapter 3.

A third objective of this work was to connect our SPME measurements to chemical potentials for various solutes. Results were compared to predictions from thermodynamic for ideal-dilute mixtures. Micelle-water partition coefficients and the extent of solubilization were also measured for decane, limonene, and octanol in aqueous mixtures of decaethylene glycol monodecyl ether. These studies allowed us to compare partitioning behavior for different surfactant types and for hydrophobic solutes of various sizes and polarity. These results were evaluated in the context of theory given by Nagarajan and Ruckenstein (1991). Finally, a method for evaluating the Gibbs energy of dissolution was developed in the process. The findings of this objective are provided in Chapter 4.

1.6 Nomenclature

G ..... Gibbs free energy

T ..... temperature

$\mu_{i,\alpha}$ ..... chemical potential of i in phase α

s ..... molar entropy of a pure component

ϑ ..... molar volume of a pure component

p ..... pressure

p^o ..... generalized standard state pressure

$\mu_{i,v}^o$ ..... standard state chemical potential of component i in vapor

$\mu_{i,v}^*$ ..... chemical potential of solute i in vapor above pure liquid i

p_i ..... partial pressure of component i in vapor mixture

$\mu_{i,w}$ ..... chemical potential of i in solvent

$\mu_{i,w}^{\ominus}$ ..... chemical potential of i in solvent at infinite dilution

$x_{i,w}$ ..... mole fraction of solute i in solvent

p_i^* ..... partial pressure above pure liquid i

K_{px} ..... Henry's constant; hypothetical pressure extrapolated from infinite dilution

$\mu_{i,w}^*$ ..... chemical potential of pure i as a liquid

$\Delta\mu^{ref}$ ..... chemical potential change for i moving from pure solute to infinite dilution in solvent

$\varphi_{i,w}$ ..... activity coefficient of i in solvent

$\varphi_{i,m}$ ..... activity coefficient of i in micelles

$x_{i,m}$ ..... mole fraction of i in micelles

$n_{i,m}$ ..... moles of i in micelles

$n_{s,m}$ ..... moles of surfactant in micelles

$\widehat{K}_{mw}$ ..... dimensionless distribution coefficient; $x_{i,m}/x_{i,w}$

$\mu_{s,w}$ ..... chemical potential of singly dissolved surfactant monomer in water solvent

μ_g ..... chemical potential of a micelle composed of g surfactant monomers

$\mu_{s,g}^{\ominus}$ ..... infinitely dilute chemical potential of dissolved surfactant monomer

$\mu_g^{\ominus}$ ..... infinitely dilute chemical potential of dissolved micelle of size g

$\Delta\mu_g$ ..... chemical potential change from free surfactant monomer to one in a micelle of size g

x_{gj} ..... mole fraction of micelles in solvent composed of g surfactant and j solute molecules

k ..... Boltzmann constant

$\mu_{i,w}^{\ominus}$ ..... infinitely dilute chemical potential of solute in solvent

$\Delta\mu_{gj}$ ..... $\mu_{gj}^{\ominus} - g\mu_{s,w}^{\ominus} - j\mu_{i,w}^{\ominus}$

$\langle M_w \rangle$ ..... average micellar weight

PC ..... phosphatidylcholine

K_{mw} ..... partition coefficient of solute between micelles and water

K_{sm} ..... partition coefficient between stationary phase and micelles

K_{sw} ..... partition coefficient between stationary phase and water

$PDMS$ ..... polydimethyl siloxane

PA ..... polyacrylate

diC_nPC ..... diacyl phosphatidylcholine with saturated tails of n carbons in length

SPME ..... solid phase micro-extraction

Chapter 2

Measuring Vapor-Water Partition Coefficients and Aqueous Solubility of Aroma Compounds by Headspace Solid-Phase Microextraction‡

2.1 Introduction

Equilibrium partitioning of sparingly soluble organic compounds is of general importance to numerous industries, including food processing, petrochemical separation, pollution control, and toxicology. For processes found within these industries, temperature frequently plays a significant role. In such cases, knowledge of their partitioning behavior, and their temperature dependencies, can help to shed fundamental insight needed for analysis of more complicated phenomena. However, equilibrium data for many insoluble compounds remains scarce. It is therefore of interest to continue to probe experimental methods that can be used to accurately obtain this information.

Headspace solid-phase microextraction (HS-SPME) is a promising tool that can be utilized for obtaining vapor-liquid partitioning for various hydrophobic compounds. HS-SPME is a solvent-free, low volume extraction technique that integrates separation and sampling into a single step through sorption of solutes onto polymer-coated fused silica fiber. In this technique, the extracting phase is exposed to a sample matrix for a set amount of time whereby solutes partition to the fiber coating.

‡ Adapted with permission from Andrew P. Karman, Susan E. Ebeler, Nitin Nitin, Stephanie R. Dungan. Partitioning, solubility and solubilization of limonene into water or short-chain phosphatidylcholine solutions. *J Am Oil Chem Society* **2021**; 98: 979–992. DOI: 10.1002/aocs.12535. Copyright © 2021 American Oil Chemists' Society.

HS-SPME offers several advantages over traditional headspace sampling via gas-tight microsyringes. A primary advantage is that since only a small amount of analyte is removed from a given sample matrix, it can be used to uncover partitioning equilibria without significant perturbation of the system. Furthermore, the extraction phase can be optimized in accordance with the desired method. For instance, polydimethyl siloxane coatings are popular choices amongst researchers since they exhibit wide linear dynamic ranges associated with linear absorption isotherms (Pawliszyn, 2012). Other popular choices include polyacrylate (PA) fibers and carbowax (polyethylene glycol), which exhibit modified selectivity towards polar and semi-volatile compounds. A third advantage is that no solute is lost during extraction since solutes directly sorb to the polymer coating (see Figure 2.1).

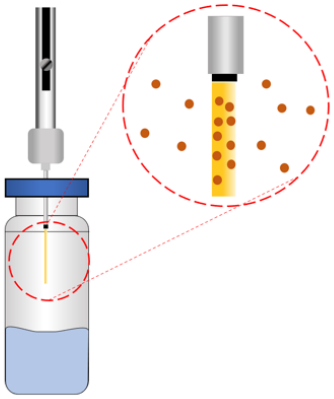

Figure 2.1. Headspace extraction of solute from a SPME sampling vial

Using methods devised by Lloyd et al. (2011a), a previous graduate student of this research group, it was determined that SPME could accurately quantify vapor-liquid partition coefficients for various hydrophobic compounds. In their studies, particular emphasis was given to error analysis and experimental limitations of the approach. For compounds which heavily favored partitioning into either the liquid or vapor phases, it was determined that even small sources of experimental uncertainty could become significantly magnified in the calculation of the vapor-liquid partition coefficient. For compounds that partition nearly equally between vapor and liquid, however, the accuracy of the

approach was significantly improved. Thus, it was thought that HS-SPME might be a suitable candidate for probing vapor-water partition coefficients over narrow temperature intervals, in which changes in this coefficient could remain near the same order of magnitude. This chapter presents complementary studies that show how HS-SPME can be successfully used to capture partition coefficients over a narrow temperature interval for limonene. Through establishing these partition coefficients, we can further validate the accuracy of these approaches.

A second key aim of this chapter involves the solubility measurements of poorly water-soluble organic compounds. Typically, solubilities are measured by adding an excess of solute to water, followed by extraction and analysis of the aqueous phase for solute quantities (Fichan et al., 1999; Schmid et al., 1992). This approach can be affected by incomplete separation or losses during the process, especially for volatile solutes. Advantages of assessing solubility using HS–SPME are that headspace measurements are determined by the concentration of vapor in equilibrium with actual dissolved solute, rather than measuring solute added or extracted. The method also allows us to sample solute distributions with a short extraction time and in situ—without the need of an additional separation step.

2.2 Materials and Methods

2.2.1 Materials

R-(+)-limonene (99%), n-decane (≥99%), and 1-octanol (99%) were purchased from Sigma-Aldrich (St. Louis, MO). Dimethyl sulfoxide was purchased from Thermo Fisher Scientific (Rockford, IL). Deionized water was obtained from a MilliQ™ water purification system installed in the laboratory (Millipore, Bedford, MA). Polyacrylate fibers (85μm) were purchased from Restek (Bellefonte, PA), and conditioned upon first use in accordance with instructions given by the manufacturer. Prior to

the start of the day's first experimental run, fibers were also pre-conditioned in the GC inlet (240˚C) for 15 minutes.

2.2.2 SPME-GC/MS

Partition coefficients or solubility concentrations were determined using headspace solid-phase microextraction (HS–SPME). These experiments were performed on an Agilent 6890GC/5975MS that was equipped with a Gerstel MPS 2 autosampler (Mülheim an der Ruhr, Germany), an attached agitator, and a water-cooled sampling tray (Gerstel). A diagram of the experimental setup is shown below.

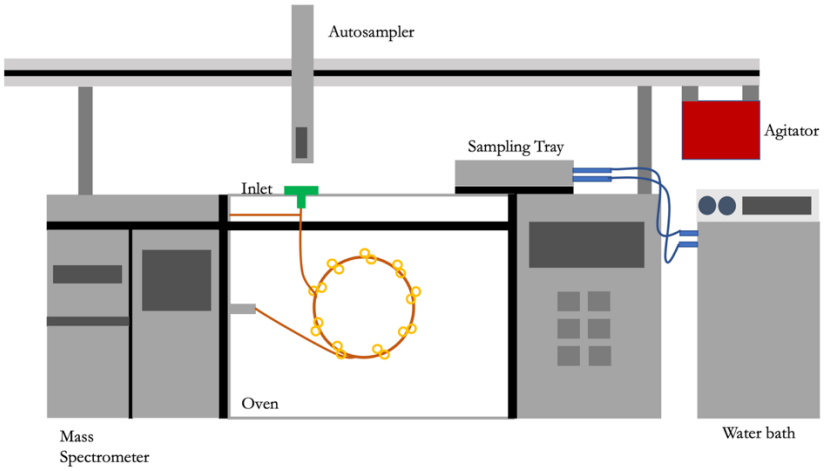

Figure 2.2. GC/MSD setup used to collect HS-SPME measurements

The GC contains a DB-Wax-ETR column of dimension 30m×0.25mm i.d.×0.25μm thickness (J&W Scientific, Folsom, CA). GC parameters used in this study are shown in Table 2.1, which is organized into several categories, depending on type of experiment and solute studied. In programming the GC, all measurements followed the same general procedure. Briefly, the oven is set to an initial temperature and is slowly heated (5˚C/min) to an intermediate temperature (Temperature 1), where it is held constant for 5 minutes. Afterwards, the column is heated more quickly (40˚C/min)

to the final temperature, which serves to prepare the column for the next measurement. In addition, the mass spectrometer detector (MSD) was programmed to run in selected-ion-monitoring (SIM) mode, using the most abundant ion fragment as determined from each solute's respective mass spectrum. Helium (99.999%) was used as the carrier gas. Sample extraction/desorption was acquired using the autosampler. During desorption step, the SPME fiber was held in the hot GC inlet (240°C) for 10 minutes to precondition the fiber for the next measurement. For extraction of solute from the headspace of prepared samples vials, a 1-minute extraction time was used. Peak area integration was performed using ChemStation (Agilent) software.

2.2.3 Experimental Procedures

To measure vapor-water partitioning behavior of limonene, samples were prepared in 21.7(±0.2) mL SPME vials (Agilent) at concentrations well below limonene's solubility limit at all temperatures studied. A stock solution of limonene was prepared by dissolving in dimethyl sulfoxide (DMSO) at concentrations of 5.3–19.2×10^{-3} M. Small amounts of stock solution were then aliquoted into SPME vials containing measured amounts of water via micro-syringe. Possible loss of solute by evaporation was prevented by placing the syringe's tip beneath the water's surface during the dilution step. The DMSO carrier solvent would initially sink to the bottom, carrying the limonene analyte along with it. Through this dilution, the final concentration of DMSO was always less than 0.2% (v/v). Limonene's water-air partitioning behavior is not expected to be affected at such low quantities of DMSO (Lloyd et al., 2011a). To measure solubilities of 1-octanol, n-decane, and limonene, samples were prepared in 21.7(±0.2) mL or 11.7(±0.2) mL SPME sample vials at concentrations 2–3 orders of magnitude larger than those used to measure partitioning. Due to the large difference of concentrations, as compared with the partitioning experiments, the use of DMSO was deemed unnecessary and consequently omitted.

Table 2.1. GC/MS parameters for analysis of solutes extracted by HS–SPME

	Partitioning Experiments	Solubility Experiments		
GC/MS Parameter	limonene	limonene	1-octanol	n-decane
Inlet Mode Split ratio	splitless	50:1	100:1	100:1
Initial Temperature (°C)	40	40	40	40
Rate 1 (°C/min)	5	5	5	5
Temperature 1 (°C)	100	75	95	75
Rate 2 (°C/min)	40	40	40	40
Final Temperature	250	240	240	240
SIM ion (m/z)[a]	68	68	56	57
GC/MS Interface Temperature (°C)	240	260	260	260
Column Flow Rate (mL/min)	0.9	1	1	1

[a]Most abundant ion fragment

Capping of the SPME vials followed a procedure given in Lloyd et al. (2011a). The capping system uses a PTFE gasket (19.1mm O.D.×14mm I.D. ×0.13 mm, Metro Gasket, Kansas City, MO), an aluminum disk (19.1 mm O.D., Reynolds, Richmond, VA), and a PTFE septum of 3 mm thickness. These were all inserted into a bi-metal (Sn/Al) crimp cap and manually capped with a crimper tool. The PTFE gasket/septum combination ensured an air-tight seal, while the aluminum disk prevented possible loss of solute by absorption into the septum. With this setup, it was determined that vials could be sealed for several hours (10+) without significant loss. Thus, the samples could be prepared all at once and allowed to equilibrate together. Mixing and equilibration was performed through programming of the autosampler, in which samples were transferred to the attached agitator (in sets of 6) for mixing, before being returned to the cooling tray for temperature equilibration. Mixing time was set to 30 minutes at 300 RPM. In addition, the agitator was programmed to switch rotation

directions at 10 second intervals to facilitate mixing. The samples were allowed to equilibrate on the tray for a period of at least 2 hours before sampling. It was determined that this time was sufficient in allowing the sample vials to reach the target temperature via thermocouple ($\pm 0.5^{\circ}$C).

From the GC method parameters provided in Table 2.1, the time to measure any given sample ranged between 16–20 minutes. This would mean that the last vial sampled would sit on the tray for several hours longer than first. To eliminate the possibility of time-dependent factors influencing the results (ex. systematic temperature changes in the lab), samples were frequently randomized during testing. As an additional control, duplicate measurements were typically included in many of the experimental "sets", where a "set" is defined as the series of measurements sampled on any given day. There did not appear to be any significant statistical differences in testing order when comparing results across multiple sets.

2.2.4 Statistics

Linear least squares regression analysis was used with a zero-intercept to determine slopes s_1 and s_2 and standard errors of the slopes were found using standard ANOVA procedures available in Microsoft Excel (Redmond, WA). Using their slope ratio $\mathcal{R}$, the vapor liquid partition coefficients and errors could be determined using error propagation as outlined by Lloyd et al. (2011a). The weight average of a result for given replicate was determined using the following equation:

$$\langle x \rangle = \frac{\sum_i w_i x_i}{\sum_i w_i}, \tag{2.1}$$

where $\langle x \rangle$ is the weighted average mean value, x_i is the value of interest as obtained from a replicate set, and w_i is the weight constant associated with x_i, defined as $w_i = 1/\sigma_i^2$, with σ_i taken as the error in x_i. The weight average error $\langle \sigma_i \rangle$ was computed as:

$$\langle \sigma_i \rangle^2 = \frac{1}{\sum_i w_i}. \tag{2.2}$$

2.3 Results and Discussion

2.3.1 Vapor-Liquid Partitioning

The following section briefly outlines the general procedure used for determining the vapor-water partition coefficient, K_{vw} for hydrophobic compounds. This procedure falls within a broader class of analytical approaches sometimes referred to by the name of "equilibrium partitioning in closed systems" (EPICS) methods. In these approaches, at least two independent measurements are made, in either in the vapor or the liquid, and are subsequently analyzed relative to one another to determine K_{vw}. The relative differences in these measurements, which stem from differences in vapor concentration of solute, was shown to be quantitively captured by varying the experimental parameter of fill fraction (Lloyd et al., 2011a).

Consider a hydrophobic compound, i, that is placed into an air-tight chamber that contains both water and vapor at amounts below its water solubility limit. After sufficient time, the system equilibrates, and the compound distributes between the two phases. A total mole balance of solute on the system gives

$$n_{i,t} = n_{i,v} + n_{i,w}, \tag{2.3}$$

where $n_{i,t}$ is the total moles of solute, $n_{i,v}$ is the moles of solute in vapor, and $n_{i,w}$ is the moles of solute in water. One can choose to rewrite Equation (2.3) in terms of vapor and liquid concentrations. Doing so gives

$$n_{i,t} = c_{i,v}V_v + c_{i,w}V_w, \tag{2.4}$$

where $c_{i,v}$ is the concentration of solute in vapor, V_v is the volume of vapor, $c_{i,w}$ is the concentration of solute in water, and V_w is the volume of the water phase. Next, we introduce the vapor liquid

partition coefficient defined as $K_{vw} = c_{i,v}/c_{i,w}$. We can substitute this term into Equation (2.4) through elimination of $c_{i,w}$. Solving for $c_{i,v}$ gives

$$c_{i,v} = \frac{n_{i,t}K_{vw}}{K_{vw}V_v + V_w}. \tag{2.5}$$

Fill fraction, which represents the amount of volume occupied by the liquid, is defined as $f = V_w/V_t$, whereas the total volume can be described in the following way: $V_t = V_w + V_v$. Substituting f into Equation (2.5) gives

$$c_{i,v} = \frac{n_{i,t}K_{vw}}{V_t(K_{vw}(1-f)+f)}. \tag{2.6}$$

Now suppose that there is a second system, of different fill fraction, that contains the same compound. Its vapor concentration may also be described by Equation (2.6). The ratio of the two systems' concentrations is therefore

$$\frac{c_{i,v_1}}{c_{i,v_2}} = \frac{n_{i,t_1}}{n_{i,t_2}}\frac{V_{t_2}(K_{vw}(1-f_2)+f_2)}{V_{t_1}(K_{vw}(1-f_1)+f_1)}, \tag{2.7}$$

where subscripts 1 and 2 are used to distinguish between these systems. Introducing dimensionless terms $N = n_{i,t_1}/n_{i,t_2}$, $\upsilon = V_{t_1}/V_{t_2}$, and $\kappa = c_{i,v_1}/c_{i,v_2}$ and solving Equation (2.7) explicitly for K_{vw} gives

$$K_{vw} = \frac{\kappa f_1 N\upsilon - f_2}{(1-f_2) - \kappa N\upsilon(1-f_1)}. \tag{2.8}$$

In the special case where $n_{i,t_1} = n_{i,t_2}$ and $V_{t_1} = V_{t_2}$, Equation (2.8) simplifies to

$$K_{vw} = \frac{\kappa f_1 - f_2}{(1-f_2) - \kappa(1-f_1)}. \tag{2.9}$$

Equation (2.9) can be used to determine K_{vw} if all other parameters are known and held constant. In our experiment $c_{i,v} = kA$, where A is the integrated peak area taken from our HS-SPME measurement and k is the constant of proportionality between A and $c_{i,v}$. Thus, in principle, only two

measurements are needed for the determination of K_{vw}. Note that, if the compound is hydrophobic, it is to be expected that Henry's law applies and, thus, K_{vw} is constant regardless of fill fraction.

From an experimentalist perspective, there are notable advantages associated with relative, as opposed to absolute, measurements of vapor concentration. For example, one can consider experimental setups where measurements (A) are related to a vapor concentration by proportionality constant (k), such as the case of this work. From Equation (2.8), one can see that the proportionality constant does not need to be explicitly known, since it would cancel once κ is evaluated. In other words,

$$\kappa = \frac{c_{i,v_1}}{c_{i,v_2}} = \frac{kA_1}{kA_2} = \frac{A_1}{A_2}. \tag{2.10}$$

Thus, preparation of a calibration curve, which can be a time-consuming procedure, is not necessary. One also finds that since only relative measurements in $n_{i,t}$ are needed, error associated with sample preparation can be significantly reduced. Gravimetric approaches, through the use of a highly precise analytical balance, would be able to accurately identify differences associated with preparing samples containing slightly different amounts of total solute.

Rather than relying on only two measurements, one can obtain more a robust estimate of K_{vw} using statistical power that comes with multiple measurements. A well-cited approach (Gossett, 1987), is to take several measurements of fill fraction "pairs" (i.e., high and low fill fractions) and proceed to average every possible combination using Equation (2.8). A second approach, which has been aptly referred to as the "phase-ratio variation method", would involve taking the inverse of Equation (2.6) and constructing plots of fill fraction versus $c_{i,v}$ for samples containing fixed amounts of solute. The slope obtained from this procedure could then be utilized to find K_{vw} (Ettre et al., 1993). A third possibility, as discussed in Lloyd et al. (2011a), is to recognize that a plot of vapor concentration versus total moles of solute, for a set fill fraction, would result in a straight line of positive slope as described

by Equation (2.5). Thus, from Equation (2.6) if a series of measurements for $c_{i,v}$ is taken over a range of n unique values for the total moles $n_{i,t}$ for a given fill fraction (f_1), the resulting slope (s_1) would be equal to

$$s_1 = \frac{K_{vw}}{V_{t_1}(K_{vw}(1-f_1)+f_1)}. \tag{2.11}$$

Similarly, a second system containing fill fraction f_2 would give

$$s_2 = \frac{K_{vw}}{V_{t_2}(K_{vw}(1-f_2)+f_2)}. \tag{2.12}$$

Division of Equation (2.11) by Equation (2.12) leads to

$$\frac{s_1}{s_2} = \frac{V_{t_2}(K_{vw}(1-f_2)+f_2)}{V_{t_1}(K_{vw}(1-f_1)+f_1)}. \tag{2.13}$$

If $V_{t_2} = V_{t_1}$ and we define s_1/s_2 as $\mathcal{R}$, then Equation (2.13) simplifies to

$$K_{vw} = \frac{\mathcal{R}f_1 - f_2}{(1-f_2)-\mathcal{R}(1-f_1)}, \tag{2.14}$$

once it is solved explicitly for K_{vw}. If one compares Equation (2.14) with Equation (2.9) it can be seen that they are quite similar; the only difference between the two is that the concentration ratio (κ) in Equation (2.9) has been replaced with the slope ratio $(\mathcal{R})$. If $c_{i,v} = kA$, then a plot of A versus $n_{i,t}$ would yield slopes equal to $S_1 = s_1/k$ and $S_2 = s_2/k$, where s_1 and s_2 are defined by Equations (2.11) and (2.12), respectively. As was the case for Equation (2.9), Equation (2.14) may also be applied when vapor concentrations are proportional for reasons that are analogous to Equation (2.10). The advantage of using slopes to calculate K_{vw} is that it provides a "check" by ensuring that vapor phase peak area measurements are proportional to $n_{i,t}$ which is a necessary, albeit not sufficient, criterion for indicating that such measurements are proportional to the vapor concentration. The above approach, leading to Equation (2.14) was used in this work.

2.3.2 Vapor-Liquid Partitioning Results

Measurements were made of peak area versus total amount of limonene added (in nmol) into water- containing headspace vials, with results plotted in Figure 2.3 (a-e). Temperatures were controlled at 15.0(±0.5)˚C, 22.0(±0.5)˚C, 30.0(±0.5)˚C, and 40.0(±0.5)˚C. Additional measurements, taken at ambient conditions using no temperature control, are also included. In each figure, peak areas were measured for two separate liquid volumes. As expected, peak areas were proportional to added limonene. Each liquid volume data replicate 'set' was subsequently fit to a line with a zero-intercept, using least-squares linear regression. The figures show that as the temperature is increased, the ratio of the fitted slopes, $\mathcal{R}$, changes at each given temperature. More specifically, at the lowest studied temperature (15˚C), the slopes are practically identical. As temperature is increased, the differences in slope ratio are magnified, with the largest difference in slopes occurring at 40˚C. The slopes, their ratio $(\mathcal{R})$, and the weighted slope ratio average $\langle\mathcal{R}\rangle$ are given in Table 2.3. All measurements were performed in triplicate sets. The coefficient of determination for these slopes (R^2) ranged between 0.955 to 0.998 and values were generally larger than 0.97. The weights used in calculating $\langle\mathcal{R}\rangle$ were taken as $1/\sigma_{\mathcal{R}}^2$, with $\sigma_{\mathcal{R}}$ representing the propagated error of the slope ratio. From $\langle\mathcal{R}\rangle$, the vapor-liquid partition coefficient (K_{vw}) was calculated using Equation (2.14). These averaged K_{vw} values, together with their 95% confidence intervals and comparative literature values, are presented in Table 2.3. The 95% confidence intervals were calculated from a Student's t-distribution. From this table, it can be seen that an increase in temperature leads to a larger vapor-liquid partition coefficient, but the latter value remains within the same order of magnitude.

Inspection of Figure 2.3 (a-e) shows that the slopes that correspond to the higher fill fraction measurements lead to larger slopes for all temperatures studied. The apparent relationship between

K_{vw} and f can be understood by examination of Equation (2.6). From this equation we find that if $K_{vw} > 1$, then $c_{i,v}$ increases as the fill fraction increases. One way of visualizing this behavior, as discussed in Lloyd (2011a), is by considering several limiting cases. First, one can examine the case where $K_{vw} \to \infty$. In this hypothetical scenario, all of the solute resides in the vapor. Therefore, any addition of water would serve to only to compress the vapor volume, which would thereby increase the solute vapor concentration. In this sense, the water phase behaves like a piston. Next, consider the case where K_{vw} is equal to 1. Substitution of this value into Equation (2.6) leads to an expression in which the vapor concentration is independent of fill fraction. Intuitively, this makes sense, since, by definition, a K_{vw} value of 1 means that the solute exhibits no thermodynamic driving force for either the vapor or the water phase. Combining the outcomes of these two limiting cases suggests that if $1 < K_{vw} < \infty$, increasing fill fraction increases $c_{i,v}$. For the final limiting case, consider when $K_{vw} \to 0$. In this case, all of the solute would reside in the liquid, and the removal of water (or addition of vapor) would serve to only concentrate the solute in water. In this sense, the vapor acts like a piston. Combining the outcomes for when $K_{vw} \to 0$ and below $K_{vw} = 1$ would suggest that $c_{i,v}$ decreases as the fill fraction increases. These explanations can be verified mathematically by testing Equation (2.6) for different values of K_{vw}.

As a final remark, we briefly discuss the accessible range of fill fraction ratios. From a physical standpoint, $0 < K_{vw} < \infty$ as discussed above. From Equation (2.14) we can determine the domain of $\mathcal{R}$. To do so, one would first need to explicitly solve $\mathcal{R}$ and then, subsequently, evaluate $\mathcal{R}$ for the two cases of when $K_{vw} \to \infty$ and $K_{vw} \to 0$. Doing so, and one obtains for the two K_{vw} limits $\mathcal{R} = (1 - f_2)/(1 - f_1)$ and $\mathcal{R} = f_2/f_1$, respectively. The domain of $\mathcal{R}$ is defined between smallest, $\mathcal{R}_{min}$, and largest, $\mathcal{R}_{max}$, of these two values, giving a domain defined on the interval $(\mathcal{R}_{min}, \mathcal{R}_{max})$.

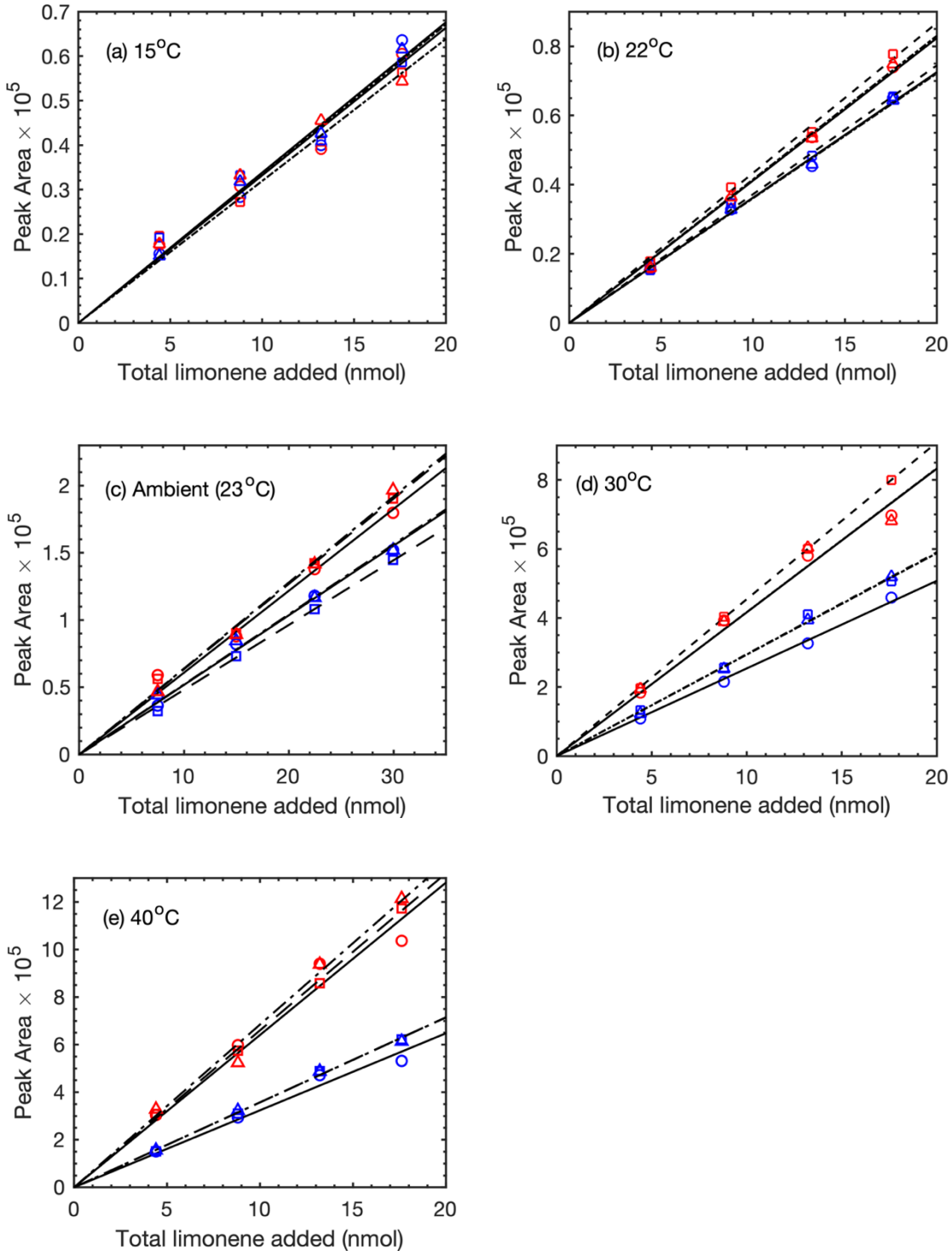

Figure 2.3. Replicate peak area measurements plotted as triplicate sets (○, □, Δ) to determine K_{vw} of limonene at (a) 15(±0.5) ˚C, (b) 22(±0.5) ˚C, (c) 23(±1) ˚C (ambient), (d) 30(±0.5) ˚C, and (e) 40(±0.5) ˚C. Symbols in blue (lower) and red (upper) correspond to fill fractions of f_1=0.0922 and f_2=0.908, respectively. Lines (—, – – ,– ·) correspond to best fit of replicate set as determined by linear regression. Total vial volumes were 21.7(±0.2) mL

Table 2.2. The vapor-liquid partition coefficient, K_{vw}, calculated from the experimental data collected in this work

	K_{vw} (± 95% C.I.)	Literature Values
15.0(±0.5)°C	0.97±0.12	—
22.0(±0.5)°C	1.231±0.062	—
23(±1)°C	1.36±0.18	—
25°C	—	1.7(±0.5) (Welke et al., 1998) 1.151(±0.002) (Copolovici and Niinemets, 2005) 1.314(±0.064), HS–SPME (Lloyd et al., 2011a) 1.34(±0.19), DI–SPME (Lloyd et al., 2011a)
30(±0.5)°C	1.94±0.14	1.57±0.092 (Helburn et al., 2008)
40(±0.5)°C	2.71±0.18	—

The data shown in Table 2.2 could be of practical use in beverage applications. Scientists interested in modeling physical changes in aroma flavors during human consumption, for example, must account for rapid temperature equilibration with the human body (Taylor, 1996). Provided the beverage matrix is like that of water, the changes in aroma concentration are captured by changes in K_{vw}.

2.3.3 Assessing Uncertainty of Vapor-Liquid Partitioning Values

From the $\mathcal{R}$ values presented in Table 2.3, we can calculate values of K_{vw} by simple application of Equation (2.14). However, more work must be done to properly evaluate the confidence associated with these values. To do so, one should recognize that the accuracy of the measured K_{vw} is a strong function of both the choice of method parameters and the "true" K_{vw} value.

To better explain what is meant by the above, we can start with in an example. Suppose that measurements in A are subject to random errors within the experimental procedure. To distinguish the effects of random error from real physical behavior, it would be advantageous if measured slopes were as different from another as the experimental procedure allows. As was already discussed in

§2.3.2, this can be accomplished by maximizing differences in fill fraction. In our experiments, the lower fill fraction limit was chosen such that DMSO, a non-volatile carrier solvent for limonene, never exceeded 0.2% v/v. This limitation was imposed to ensure that there were no significant changes to the bulk properties of water associated with its addition. The upper fill fraction was chosen to be approximately the largest amount of volume that could be added before fiber would contact the liquid.

Table 2.3. Data used to calculate K_{vw}. Each row represents experimental sets consisting of measurements acquired during the same experimental run of a given day. The slope ratio, $\mathcal{R}$, equals Slope 1 divided by Slope 2. The weighted slope ratio $\langle\mathcal{R}\rangle$ is weighted using the squared inverse of the error

Temperature (°C)	Slope $s_1 \times 10^3$ ($nmol^{-1}$)	R^2	Slope $s_2 \times 10^3$ ($nmol^{-1}$)	R^2	$\mathcal{R}$	$\langle\mathcal{R}\rangle$[a]
15.0 (±0.5)	33.2±1.5	0.966	33.8±1.5	0.964	0.982±0.022	0.977±0.034
	31.9±1.3	0.968	33.6±1.6	0.961	0.952±0.061	
	33.6±1.6	0.960	34.3±0.10	0.990	0.968±0.052	
22.0 (±0.5)	41.2±0.68	0.995	36.2±0.73	0.993	1.136±0.030	1.1520±0.015
	43.3±0.71	0.996	37.2±0.57	0.995	1.165±0.026	
	55.6±0.090	0.995	48.3±0.070	0.996	1.151±0.025	
23 (±1)	60.9±2.0	0.981	51.8±0.86	0.995	1.176±0.043	1.253±0.022
	63.4±1.4	0.991	48.2±0.60	0.998	1.317±0.033	
	63.9±1.2	0.994	52.1±1.3	0.989	1.227±0.039	
30 (±0.5)	416.2±12.8	0.983	253.8±4.2	0.995	1.640±0.057	1.5412±0.026
	454.2±1.2	0.999	295.1±6.1	0.992	1.539±0.032	
	423.2±7.3	0.965	293.8±2.8	0.998	1.418±0.066	
40 (± 0.5)	640.8±14.3	0.955	324.0±14.3	0.966	1.978±0.133	1.862±0.027
	660.3±6.1	0.998	357.6±4.7	0.997	1.847±0.030	
	684.6±6.1	0.982	356.2±5.7	0.995	1.912±0.069	

[a] $\langle\mathcal{R}\rangle$ is weighted average using the squared inverse of the propagated error as determined from individual replicate sets.

The existence of possible experimental errors and their effects on the calculated K_{vw} are next discussed. From Equation (2.9), we find that K_{vw} is a function of the fill fractions ($f_1$and f_2) the slope ratio $(\mathcal{R})$. Suppose that the measured value of $\mathcal{R}$ contains an associated standard error, which

we will denote as $\sigma_{\mathcal{R}}$. Since $\mathcal{R} = s_1/s_2$, one may be able to find $\sigma_{\mathcal{R}}$ using standard propagation of uncertainty via a first-order Taylor series expansion. That is, for some function $y(x_1, x_2 \ldots x_n)$ with standard deviations in the variables given by $\sigma_1, \sigma_2 \ldots \sigma_n$, then the standard deviation in y, is obtained as follows:

$$\sigma_y^2 = \sum_{i=1}^{n} \left(\frac{\partial f}{\partial x_i}\right)^2 \sigma_i^2, \tag{2.15}$$

where σ_y^2 is the variance of y. Note that the above analysis is valid only if errors in the measurements are uncorrelated. Application of Equation (2.15) to estimate errors in $\mathcal{R}$ yields

$$\sigma_{\mathcal{R}} = \pm\mathcal{R}\sqrt{\left(\frac{\sigma_{S_1}}{S_1}\right)^2 + \left(\frac{\sigma_{S_2}}{S_2}\right)^2} \tag{2.16}$$

σ_{S_1} and σ_{S_2} are the standard errors of the slopes, for fill fractions 1 and 2 respectively. These errors may be found using standard linear regression techniques. For relative error defined as $\epsilon = \pm\sigma_{\mathcal{R}}/\mathcal{R}$, the error in $\mathcal{R}$, $\mathcal{R}_{err}$, can be written as $\mathcal{R}_{err} = \mathcal{R}(1+\epsilon)$. Substitution of $\mathcal{R}_{err}$ into Equation (2.8) will give $K_{vw,err}$. That is,

$$K_{vw,err} = \frac{f_1\mathcal{R}(1+\epsilon) - f_2}{(1-f_2) + (1-f_1)R(1+\epsilon)}. \tag{2.17}$$

where the errors associated with fill fractions are negligibly small. The relative error in K_{vw}, which we call δ, may then be calculated as $\delta = (K_{vw,err} - K_{vw})/K_{vw}$. A plot of the magnitude of δ versus K_{vw} is given in Figure 2.4 for ϵ=±0.05, which has been essentially recreated from Lloyd et al. (2011a). It can be seen that δ becomes large as K_{vw} moves away from its minimum (~1). Thus, we can gather that at very large (10^2) or very small values (10^{-2}) values of K_{vw}, even small errors in the slope ratio become important. Our measured K_{vw} are all close to the value of one and their close agreement with values found within the literature are consistent with this analysis.

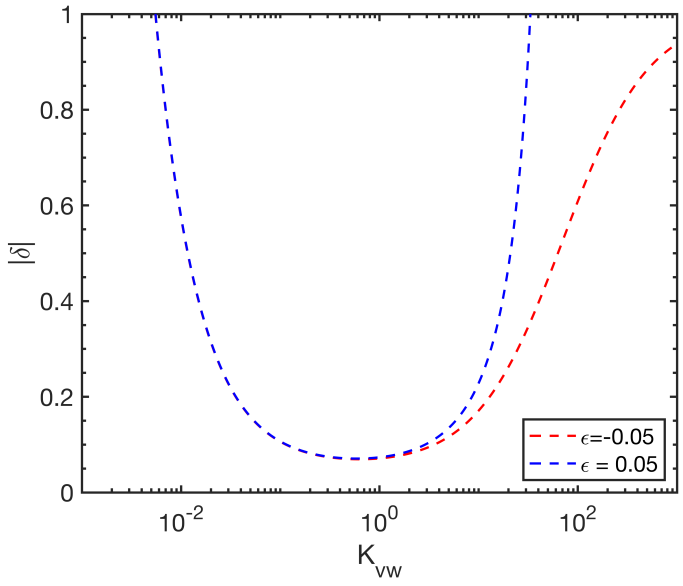

Figure 2.4. Magnitude of the relative error for a system with fill fraction as f_1=0.783 and f_2=0.092; fill fractions used in this study (Lloyd et al., 2011a).

2.3.4 Application of the van't Hoff Equation

Having found a temperature dependence associated with K_{vw} for limonene, it was determined that its corresponding enthalpy of volatilization could also be evaluated. A brief derivation is next provided. In Chapter 1, we showed that the Henry's constant, K_{px}, of a solute is related to the difference of its chemical potential within each phase. Since K_{vw} is effectively a Henry's constant, it can be related to K_{px} through the ideal gas law equation as

$$K_{vw} = \frac{\bar{v}_W}{RT}\frac{p_i}{x_{i,w}} = \frac{\bar{v}_W}{RT}K_{px} \tag{2.18}$$

for a dilute solution. Here $\bar{v}_W$ is the molar volume of water, p_i is the solute's partial pressure, and RT is the thermal energy. With this relationship and the expression for K_{px} given in Equation (1.15) K_{vw} can now be rewritten as

$$K_{vw} = \frac{p_i^* \bar{v}_W}{RT}\exp\left(\frac{{\mu_{i,w}}^{\ominus} - {\mu_{i,v}}^*}{RT}\right), \tag{2.19}$$

where $\mu_{i,w}^{\ominus}$ is the chemical potential of solute in water at infinite dilution, $\mu_{i,v}^{*}$ is the chemical potential of solute in vapor above pure solute, and p_{i}^{*} is the partial pressure of i above pure solute. At equilibrium $\mu_{i,v}{}^{*} = \mu_{i,w}{}^{*}$ for pure liquid i, and thus the above equation can be rewritten as

$$K_{vw} = \frac{p_{\mathrm{i}}^{*}\bar{v}_W}{RT}\exp\left(\frac{\mu_{i,w}{}^{\ominus} - \mu_{i,w}{}^{*}}{RT}\right) \tag{2.20}$$

One should now recognize that the term within the exponential of Equation (2.19) represents the dimensionless molar Gibbs energy of dissolution, $\Delta_d\bar{G}/RT$, which describes the energy to transfer one mole of solute from its pure state into an aqueous solution at infinite dilution. Following the definition of Gibbs free energy and taking the natural log on both sides, Equation (2.20) becomes:

$$\ln(RTK_{vw}) = \ln p_{\mathrm{i}}^{*} + \ln\bar{v}_W + \frac{\Delta_d\overline{H}}{RT} - \frac{\Delta_d\bar{S}}{R}, \tag{2.21}$$

where $\Delta_d\overline{H}$ and $\Delta_d\bar{S}$ are the enthalpy and entropy of dissolution, respectively. The Clausius-Clapyeron equation relates changes in vapor pressure with respect to temperature to the enthalpy of vaporization, $\Delta_{vap}\overline{H}$, as

$$\frac{d}{dT}(lnp_i^{*}) = \frac{\Delta_{vap}\overline{H}}{RT^2}. \tag{2.22}$$

Here $\Delta_{vap}\overline{H}$ represents the energy needed to transfer one mole of solute, from pure liquid solute to the vapor. Differentiating Equation (2.21) with respect to temperature gives

$$\frac{d}{dT}ln(RTK_{vw}) = \frac{\mathrm{d}}{\mathrm{dT}}lnp_{\mathrm{i}}^{*} + \frac{d}{dT}\ln\bar{v}_W + \frac{d}{dT}\left(\frac{\Delta_d\overline{H}}{RT} - \frac{\Delta_d\bar{S}}{R}\right). \tag{2.23}$$

Note that $\Delta_d\overline{H}$ is related to $\Delta_{vap}\overline{H}$ through $\Delta_{vol}\overline{H} = \Delta_{vap}\overline{H} - \Delta_d\overline{H}$, where $\Delta_{vol}\overline{H}$ is the enthalpy of volatilization, which represents the energy needed to transfer one mole from an infinitely dilute solution to the vapor. Assuming that $\Delta_d\overline{H}$ and $\Delta_d\bar{S}$ are temperature independent, then Equation (2.23) becomes

$$\frac{d}{dT} ln(RTK_{vw}) = \frac{d}{dT} \ln \bar{v}_W + \frac{\Delta_{vap}\overline{H} - \Delta_d \overline{H}}{RT^2}. \quad (2.24)$$

Expressing dT as $-T^2 d(1/T)$, Equation (2.24) yields the simplified result

$$\frac{d}{d(1/T)} \ln(RTK_{vw}) = \frac{d}{d(1/T)} \ln \bar{v}_W - \frac{\Delta_{vol}\overline{H}}{R}, \quad (2.25)$$

a type of van't Hoff equation. In addition, the first term in Equation (2.25) can be neglected if there is only a small change in molar volume with temperature. Thus, a plot of $\ln(RTK_{vw})$ versus $1/T$ yields a slope from which $\Delta_{vol}\overline{H}$ can be estimated. Figure 2.5 below was constructed from the data given in Table 2.2 and Equation (2.25) and $\Delta\overline{H}_{vol}$ is given in Table 2.4. Also included in Table 2.4 are literature values from Copolovici and Niinemets (2005) and Massaldi and King (1973).

Table 2.4. The experimental enthalpy of volatilization, $\Delta\overline{H}_{vol}$, together with published literature values

$\Delta\overline{H}_{vol}$ (kJ/mol)	Reference
34.5±2.7[a]	This work
37.8±0.9	Copolovici and Niinemets (2005)
35.1[b]	Massaldi and King (1973)

[a] 95% C.I.

[b] From $\Delta_{vol}\overline{H} = \Delta_{vap}\overline{H} - \Delta_d\overline{H}$ using $\Delta_{vap}\overline{H}$ as reported in (Copolovici & Niinemets, 2005) and $\Delta_d\overline{H}$ (Massaldi & King, 1973)

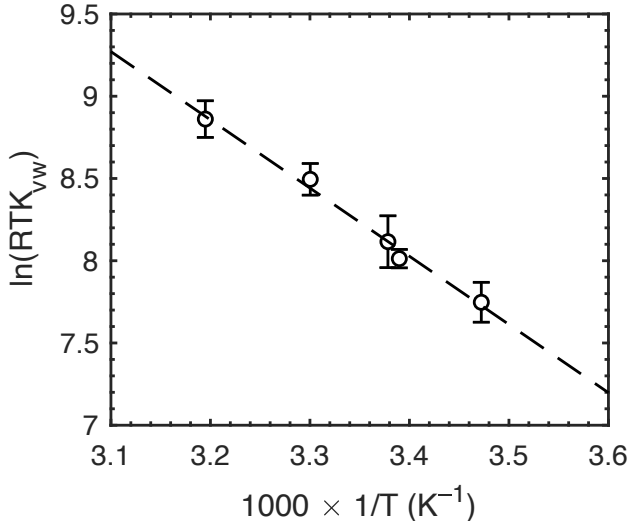

Figure 2.5. Natural log of RTK_{vw} versus $1/T$ from Table 2.3. Line represents the best fit from linear regression, with slope yielding the enthalpy of volatilization from Equation (2.25)

2.3.5 Solubility Measurements

Next, we determined the aqueous solubility concentrations at 25.0(±0.5)°C for the hydrophobic compounds d-limonene, 1-octanol, and n-decane. In addition, the aqueous solubility concentration of limonene at 40.0(±0.5)°C was determined. To do so, we first measured peak area versus total solute additions, in which the latter was added at amounts three orders greater in magnitude than those used in measurements described in §2.3.2. For these measurements, only a single fill fraction was used for each sample vial. The limonene solubility studies (25°C and 40°C) were conducted using 2 mL of water in 11.7 mL SPME vials (f=0.171). The decane and octanol solubilities were found using 5 mL of water in 21.7 mL vials (f=0.230). From the total mole balance given by Equation (2.3), one can solve for the aqueous concentration $c_{i,w}$ at saturation $(c_{i,w}^{sat})$ through the elimination of $c_{i,v}$ by substituting the definition for K_{vw}. Doing so gives

$$c_{i,w}^{sat} = \frac{n_{i,t}}{K_{vw}V_v + V_w}. \tag{2.26}$$

In all cases, peak area increased linearly with added solute, followed by a sharp break such that peak area is level at progressively higher solute additions. The break is indicative of the maximum amount of solute that can be dissolved before the water is saturated with solute. Above this limit, a newly formed solute rich phase arises, which is saturated with small amounts of dissolved water. An example solubilization isotherm for a water-decane solution is given in Figure 2.6 below. Here, the left axis shows raw GC/MS peak areas, and the right axis provides solute vapor concentrations normalized by the averaged set of saturated values ($c_{i,v}/c_{i,v}^{sat}$). Measurements in the saturated region were identified by visual inspection and their average value was used to create the top horizontal line. The remaining data points were fit to a second line using linear regression techniques. $n_{i,t}$ was estimated from the intersection between the line fitted to solute additions prior to and including the apparent break point and the horizontal line from the peak area after the apparent break point. The slopes, the coefficient of determination (R^2), and the estimated break point (in terms of total added solute) are given in Table 2.5.

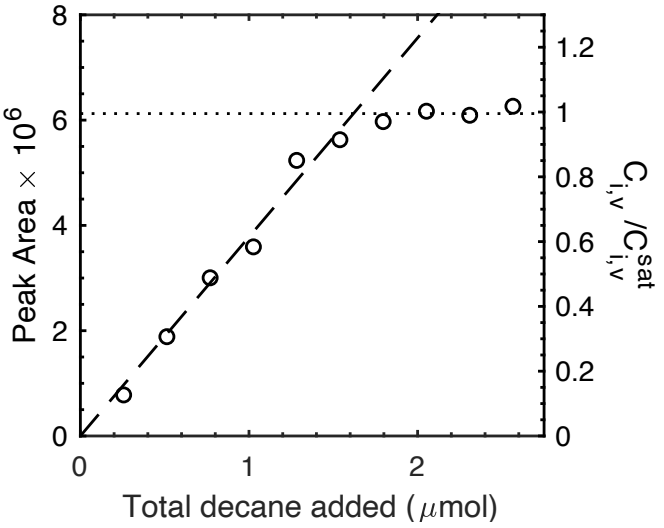

Figure 2.6. Raw GC/MS peak area data of aqueous decane solutions. Here f=0.230 and V_t=21.7(±0.2) mL

Measurements for all solutes are shown in Figure 2.7. Plotting normalized values provides a comparison between replicate sets. Doing so led to good reproducibility between normalized sets, as would be expected with similarity in breakpoint value. As an alternative to identifying the plateau region by inspection, a statistically more robust approach to determine the breakpoint has been previously developed (Muggeo, 2003). This method employs an algorithm that fits multiple line segments: one prior to and after a "guessed" break point. The slope of each segment is evaluated by a 'difference in slopes parameter' and iteratively checked against a mathematical identity. This method is especially useful for situations where there is ambiguity in breakpoint determination.

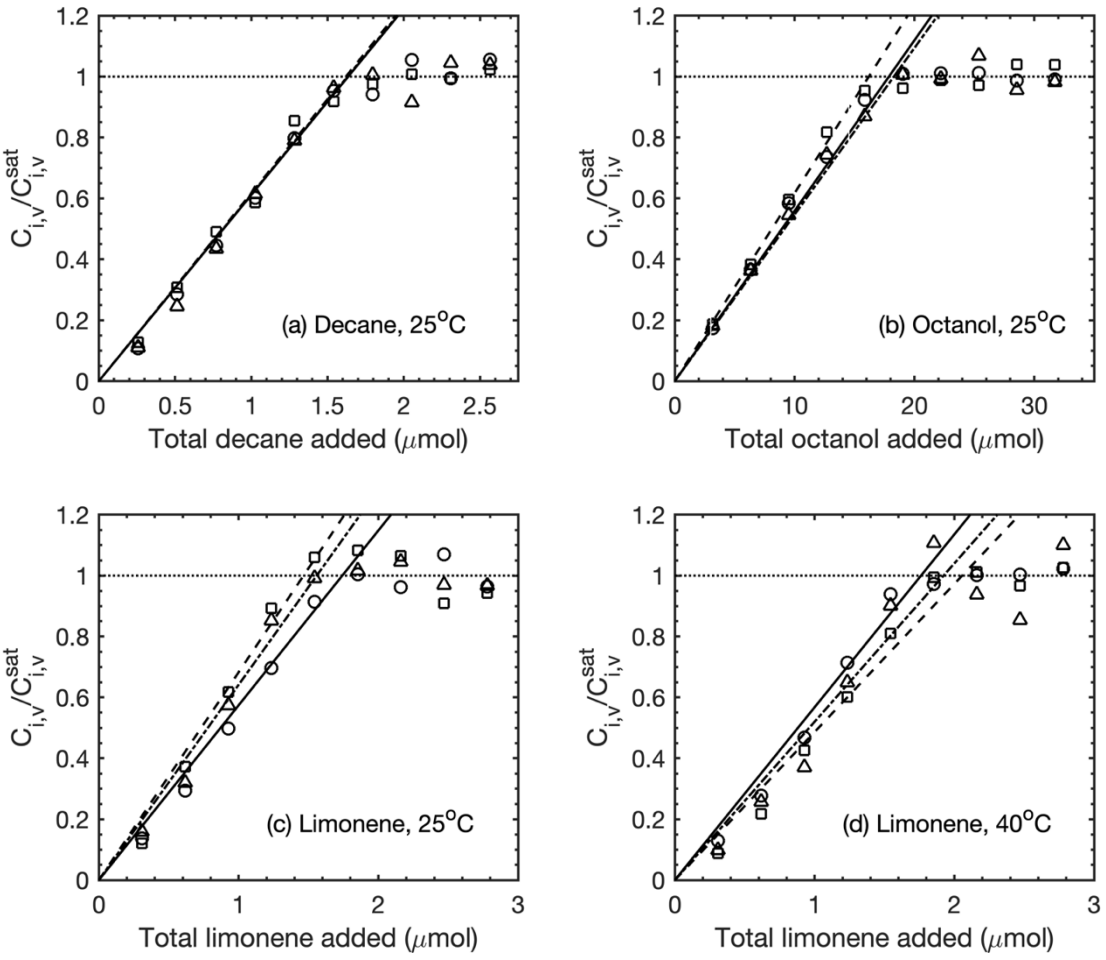

Figure 2.7. Normalized vapor concentrations ($c_{i,v}/c_{i,v}^{sat}$) versus total solute added, shown as triplicate sets (○, □, Δ). Lines (—,– –,– ·) correspond to best linear fits of replicate sets. For (a) and (b), f=0.230 and V_t=21.7(±0.2) mL; for (c) and (d), f=0.171 and V_t=11.7(±0.2) mL

Table 2.5. HS–SPME data used to calculate the solubility limit for three solutes in water; pure peak areas A^* are averages from three vials containing pure solute.

		Slope (μmol^{-1})[a]	R^2	$\langle A^{sat} \rangle$ (saturated)	A^* (pure)	$n_{i,t}^{sat}$ (μmol)	$\langle n_{i,t}^{sat} \rangle$[b] (μmol)
Decane	25(±0.5)°C	(39.6±0.5)×10^5	0.991	(64.8±1.6)×10^5	(73.7±1.4)×10^5	1.635±0.091	1.63 ±0.072
		(37.8±1.1)×10^5	0.968	(61.2±1.2)×10^5	(72.9±1.6)×10^5	1.62±0.053	
		(38.6±0.7)×10^5	0.984	(63.0±4.5)×10^5	(69.2±2.9)×10^5	1.63±0.12	
Octanol	25(±0.5)°C	(41.9±1.0)×10^3	0.976	(74.9±4.9)×10^4	(83.4±2.5)×10^4	17.87±0.47	17.44 ±0.35
		(46.2±1.0)×10^3	0.990	(74.8±0.3)×10^4	(84.4±2.7)×10^4	16.19±0.66	
		(42.8±0.7)×10^3	0.986	(74.2±3.4)×10^4	(83.4±1.5)×10^4	18.28.±0.94	
Limonene	25(±0.5)°C	(19.1±0.4)×10^5	0.977	(33.3±1.7)×10^5	(29.9±1.3)×10^5	1.742±0.097	1.608 ±0.057
		(25.5±0.9)×10^5	0.972	(37.3±3.2)×10^5	(36.8±1.4)×10^5	1.47±0.14	
		(24.8±0.9)×10^5	0.971	(38.4±1.8)×10^5	(39.1±5.8)×10^5	1.559±0.082	
	40(±0.5)°C	(19.3±0.9)×10^5	0.954	(33.9±0.7)×10^5	(45.9±1.7)×10^5	1.761±0.090	1.870 ±0.070
		(15.8±0.9)×10^5	0.939	(32.6±0.8)×10^5	(49.3±5.9)×10^5	2.05±0.12	
		(18.6±1.35)×10^5	0.898	(35.8±4.4)×10^5	(51.3±8.5)×10^5	1.93±0.28	

[a]Errors given as 1 standard error of the regression slope.
[b]Errors listed as standard error of the mean.

Table 2.5 contains data from peak area measurements of pure solute, which were taken in order to compare them to values from vapor above water mixtures in equilibrium with excess oil. Vapor-liquid partition coefficient and solubility concentrations, along with their respective reference literature sources, are also given in Table 2.6. The following is the order of increasing solubility observed at 25.0(±0.5)°C: decane, limonene, and 1-octanol. As one might expect, the more hydrophobic compounds yielded the lower aqueous solubilities. Limonene's solubility is approximately 200× higher than decane, and 35× lower than octanol, although all three solutes are quite close in molecular weight. With the exception of limonene at 25°C, pure solute measurements yielded larger peak areas than the data taken above saturated aqueous measurements. It likely that the latter saturated solution

peak areas were smaller due to the lowering of the solute chemical potential in excess bulk oil due to saturation by water.

The data is in good agreement in instances where literature values could be found. However, we were not able to find direct measurements of the limonene's aqueous solubility at 40°C, in which our saturation concentration was surprisingly slightly lower than that determined at room temperature. Such decreases have been observed for other aqueous hydrophobic systems, as has been reported elsewhere for similar temperature conditions.(Miller et al., 1998; Tsonopoulos, 1999) To further investigate these results, we estimate the solubility concentrations via Equation (2.27), given below, in which the solute partial pressure above the saturated solution was approximated from its pure component vapor pressure. That is,

$$c_{i,w}^{sat} V_w = n_{i,t} - \frac{p_i^* V_v}{RTK_{vw}}. \tag{2.27}$$

The basic premise of this calculation is that K_{vw} is valid at all concentrations up to the solute's solubility limit and that the chemical potential of solute in a saturated solution is essentially equal to its pure component form. p_i^* was measured by Massaldi and King (1973), giving values of 189 Pa at 25°C and 482 Pa at 40°C, respectively. The latter was calculated from the well-known Antoine equation from data taken up to 32°C. In using Equation (2.27), we have used our own K_{vw} values given in Table 2.3 and Table 2.6 for calculation of limonene solubilities. Using these vapor pressures yield solubilities that are nearly identical at the two temperatures (~4×10^{-4} M). Given temperature dependencies of solute partitioning and vapor pressure, combined with experimental uncertainties, the effect of limonene solubility between 25°C and 40°C may be too weak to ascertain. For octanol, using a pure vapor pressure at 25°C of 10.26 Pa (Kulikov et al., 2001), Equation (2.27) yields a solubility of 3.5×10^{-3} M. We note that the vapor procedure could not be applied to decane, because its strong partitioning into the vapor phase leads to a comparatively small number of moles that therefore cannot

be accurately determined from Equation (2.27). Overall, the use of our own and literature values for K_{vw} yield results for aqueous solubility of hydrophobic solutes that are more consistent with measurements by others, compared to when vapor pressure data is used in concert with Equation (2.27).

Table 2.6. Aqueous solubility measurements and literature values for limonene, decane and octanol[a]

		$c_{i,w}^{sat}$ (M), this work	K_{vw}	$c_{i,w}^{sat}$ (M), literature
Limonene	25(±0.5)°C	(1.04±0.07)×10^{-4}	1.36±0.18; This work	1.5×10^{-4} (Fichan et al., 1999) 0.45×10^{-4} (Schmid et al., 1992) 0.95×10^{-4} (Weidenhamer et al., 1993) 1.01×10^{-4} (Massaldi and King, 1973) 0.906×10^{-4} (Tamura and Li, 2005)
	40(±0.5)°C	(6.5±1.1)×10^{-5}	2.71±0.18; This work	—
Decane	25(±0.5)°C	(4.9±0.9)×10^{-7}	201; (Mackay and Shiu, 1981)	3.66×10^{-7} (McAuliffe, 1969) 3.23×10^{-7} (Tolls et al., 2002) 3.44×10^{-7} (Letinski et al., 2016) 1.39×10^{-7} (Franks, 1966)
Octanol	25(±0.5)°C	(3.5±0.3)×10^{-3}	(1.0±0.06)×10^{-3}; (Buttery et al., 1969)[b]	3.70×10^{-3} (Kinoshita et al., 1958) 3.86×10^{-3} (Shinoda et al., 1959) 4.11×10^{-3} (Janado and Yano, 1985)

[a]Errors listed as 95% C.I. unless otherwise noted
[b]Standard deviation

2.4 Conclusions

In summary, HS-SPME was shown to be an effective tool for probing local distributions of poorly water-soluble hydrophobic solutes. Vapor water partition coefficients for limonene were determined at different temperatures together with its associated enthalpy of volatilization. Our results indicate

that this method appears to be accurate for compounds with K_{vw} values near unity, as evidenced by comparison with published values in the literature. By extension, the experimental method can be further used to accurately estimate solubility concentrations, even at concentrations on the order of 10^{-7} M. Based on these findings, it appears that HS-SPME is especially advantageous for studying partitioning of volatile compounds, since it provides good throughput and high accuracy, while only requiring standard instrumentation found in many analytical chemistry laboratories.

2.5 Nomenclature

$n_{i,t}$ ..... total moles of solute i

$n_{i,v}$ ..... moles of solute i in vapor

$n_{i,w}$ ..... moles of solute i in water

V_v ..... volume of vapor

V_w ..... volume of water

V_t ..... total volume

$c_{i,v}$ ..... concentration of solute i in vapor

$c_{i,w}$ ..... concentration of solute i in water

$c_{i,w}^{sat}$ ..... concentration of solute i in saturated water

K_{vw} ..... vapor-water partition coefficient; $c_{i,v}/c_{i,w}$

f ..... fill fraction; V_w/V_t

N ..... dimensionless $n_{i,t}$; $n_{i,t_!}/n_{i,t_2}$

υ ..... dimensionless V_t; V_{t_1}/V_{t_2}

κ ..... vapor concentration ratio; $c_{i,v_1}/c_{i,v_2}$

A ..... peak area

k ..... constant of proportionality relating A to $c_{i,v}$

s ..... slope relating $n_{i,t}$ to $c_{i,v}$ for a series of measurements

S ..... slope relating $n_{i,t}$ to A for a series of measurements

$\mathcal{R}$ ..... slope ratio of s_1/s_2

$\bar{v}_W$ ..... molar volume of water

R ..... gas constant

T ..... temperature

p_i ..... partial pressure of component i above liquid mixture

p_i^* ..... partial pressure of i above pure liquid i

$\mu_{i,w}{}^{\ominus}$ ..... chemical potential of solute i at infinite dilution in water

$\mu_{i,w}{}^*$ ..... chemical potential of pure solute i as liquid

$x_{i,w}$ ..... mole fraction of component i in water

K_{px} ..... partition coefficient; $p_i/x_{i,w}$

$\Delta_d \overline{H}$ ..... molar enthalpy of dissolution

$\Delta_d \bar{S}$ ..... molar entropy of dissolution

$\Delta_{vol} \overline{H}$ ..... molar enthalpy of volatilization

Chapter 3

Limonene Partitioning between Water and Short-Chain Phospholipid Micelles: Effects of Temperature and Composition[§]

3.1 Introduction

The ability to measure and control how hydrophobic compounds distribute among different regions within multiphase mixtures has an important role in many applications. Such compounds, which include food aromas and flavors, bioactives, and many drugs, prefer thermodynamically not to mix with water, but instead to partition heavily into vapor or other nonpolar phases or regions. This is demonstrated in the micellar solubilization of sparingly soluble compounds. Here, clusters of self-assembled surfactant molecules "host" compounds within the aggregate. In doing so, sparingly soluble compounds can be further incorporated and transported within an aqueous environment.

Solubilization plays a central role in the use of adjuvants for delivery of drugs and agro-chemicals (Kim et al., 2010; Pennell et al., 2003), physiological transport of bioactive compounds, waste-water and soil remediation, and formulation of functional foods (Livney, 2015). In these applications, micellar solubilization not only makes it possible to incorporate much larger amounts of the active ingredient into a stable aqueous solution, it also crucially modifies rates and mechanisms for solute release, evaporation, or participation in chemical reactions. Thus, it is of value to understand solute–surfactant equilibrium associative interactions, and how the resulting partitioning behaviors depend

[§] Adapted with permission from Andrew P. Karman, Susan E. Ebeler, Nitin Nitin, Stephanie R. Dungan. Partitioning, solubility and solubilization of limonene into water or short-chain phosphatidylcholine solutions. *J Am Oil Chem Society* **2021**; 98: 979–992. DOI: 10.1002/aocs.12535. Copyright © 2021 American Oil Chemists' Society.

on surfactant structure, concentration, and system temperature. In the current work, headspace solid-phase microextraction is shown to be an accessible, convenient, and accurate approach for measuring such distributions.

To measure solute distributions in surfactant-containing ternary aqueous mixtures, we used polyacrylate-coated SPME fibers to extract solute from the headspace above an equilibrated aqueous solution, employing short extraction times, for quantification by gas chromatography and mass spectrometry (GC/MS). From the headspace concentration, water/micelle partition coefficients could then be determined, given known amounts of total solute and surfactant. We have shown in previous work that such methods are well-suited for quantifying solute distributions between vapor and water in the absence of surfactant (Lloyd et al., 2011a), and for measuring solute partitioning into micelles over a wide range of compositions (Lloyd et al., 2011b), without the need to significantly alter the overall system equilibria. In addition, earlier studies have demonstrated that vapor phase measurements of volatile hydrophobic compounds are effective at accurately and non-invasively assessing their concentration distribution within aqueous micellar solutions (Christian et al., 1981; Vane and Giroux, 2000).

Using vapor-water partitioning results from solute-water mixtures discussed in Chapter 2, HS–SPME approaches were applied to the quantification of solute partitioning between water and the interior of short-chain phospholipid micelles conducted at temperatures between 15–40°C. Unlike the water-insoluble, long-chain phospholipids typically found in nature, saturated phosphatidylcholines with acyl tails of 5–8 carbons are known to self-assemble in water above a critical micelle concentration (*cmc*) (Weschayanwiwat et al., 2005). Critical micelle concentration and aggregate size and shape have been measured for these phosphatidylcholine (PC) structures in binary mixtures by small-angle neutron scattering (T. Lin et al., 1986; Lin et al., 1987) tensiometry, and light scattering (Burns et al., 1983). However, surprisingly, their solubilization properties have received far less attention. Further

investigation of these short-chain phospholipids' ability to solubilize nonpolar compounds would help to advance their application as structured lipids for food, medical and other industries. Our results provide important new insights into the performance of phosphatidylcholine aggregates as flavor delivery hosts, which is of significant interest given the widespread use of phospholipids in food and pharmaceutical applications.

3.2 Materials and Methods

R-(+)-limonene (99%), dimethyl sulfoxide (99.9%), and deionized water were obtained from sources previously given in §2.2.1. 1,2 dihexanoyl-*sn*-glycero-3-phosphocholine (diC_6PC), 1,2 diheptanoyl-*sn*-glycero-3-phosphocholine (diC_7PC), and 1,2 dioctanoyl-*sn*-glycero-3-phosphocholine (diC_8PC) were purchased from Avanti Polar Lipids (Alabaster, AL) in powdered form. These phospholipids were manufactured with >99% purity and used without further purification.

3.2.1 Experimental Methods

Partitioning of limonene between phospholipid micelles and the surrounding aqueous continuum was probed using HS-SPME methods. Micelle-water partition coefficients obtained at limonene concentrations well below its aqueous solubility limit were determined by varying either diC_6PC or diC_7PC concentrations at constant liquid volume and total limonene additions. To do so, stock solutions of limonene dissolved into DMSO were first prepared at concentrations ranging from 5.3–46.5×10^{-3} M. The stock solution was then diluted into 11.7($\pm$0.2) mL SPME vials using aqueous surfactant solutions prepared between 0–5.2×10^{-3} M diC_7PC or 0-35.2×10^{-3} M diC_6PC. The highest concentration of these provided ranges are approximately two times the reported literature cmc for these phospholipids. These surfactant solutions always contained less than 0.05% (v/v) DMSO.

Additional studies were conducted in which concentrations of limonene were varied up to its water solubility limit in fixed concentrations of PC. Here, aqueous stock PC solutions well above their reported cmc's (Tausk and Overbeek, 1974) at the following concentrations: 35.2 mM (diC_6PC),

5.2mM (diC_7PC), and 4mM (diC_8PC). From these stock solutions, 1–2 mL of solution was aliquoted directly into 11.7(±0.2) mL or 21.7(±0.2) mL SPME vials via a glass pipette. Unlike air displacement pipettes, the glass pipettes ensured that no bubbles formed during transfer of surfactant solution to the SPME vials. Direct additions of limonene were added to these PC solutions via micro syringe without the use of DMSO. Attempts at further improving data quality were performed using an internal-fibre standardization approach with details given in Appendix A.

Experiments were performed on an Agilent 6890GC/5975MS previously described in Chapter 2. Figure 2.2 shows an illustration of the setup. The GC parameters are identical to those given in Table 2.1. These parameters have been divided into two parts: measurements made at low limonene concentrations (Type 1), or measurements made at high concentrations (Type 2).

Table 3.1. GC parameters used for acquiring micellar partitioning data.

GC/MS Parameter	Type 1	Type 2
Inlet Mode Split ratio	splitless	50:1
Inlet Temperature(°C)	240	260
Initial GC Oven Temperature (°C)	40	40
Rate 1 (°C/min)	5	5
Temperature 1 (°C)	100	75
Rate 2 (°C/min)	40	40
Final Temperature	250	240
SIM ion (m/z)[a]	68	68
GC/MS Interface Temperature (°C)	240	260
Column Flow Rate (mL/min)	0.9	1

[a]Most abundant ion fragment

Immediately following the dilution step, the SPME vials were capped using a quadruple barrier technique (Lloyd et al., 2011a, 2011b). Mixing was conducted using the agitator (sets of 6) at 300 RPM. Type 1 experiments were mixed for 1 hour followed by a minimum of 2 hours of temperature equilibration using the temperature-controlled tray. Type 2 experiments were mixed for either 2 hours (diC_6PC, diC_7PC) or 3 hours (diC_8PC) and followed by a minimum of 3 hours temperature equilibration. Samples measured on a given day, comprising an experimental data set, were checked for the possibility of time-dependence by measuring them out of sequence (randomized). As an additional control, duplicate standards were placed throughout the experiment. No statistically significant results were associated with mixing order, indicating the prepared samples were equilibrated. HS-SPME measurements were made using a 1-minute extraction. Following extraction, the SPME fiber was held in the GC inlet (240°C) for 10 minutes. Prior to the day's first experimental run, fibers were also preconditioned in the GC inlet (240°C) for 15 minutes. Helium (99.999%) was used as the carrier gas. Peak area integration was performed using ChemStation software (Agilent).

3.2.2 Statistics

Weight average values and their respective errors were calculated using Equations (2.1) and (2.2) given in Chapter 2. Non-linear least squares regression was performed via a Levenberg-Marquardt fitting algorithm using MATLAB (R2020).

3.3 Results and Discussion

3.3.1 Solubilization Isotherms with Varying Phospholipid and Low Limonene Content

Partitioning behavior of limonene in aqueous phospholipid solutions consisting of either diC_6PC or diC_7PC micelles is first discussed. In these results, concentrations of limonene are maintained well below its solubility limit in water alone. Experimental peak area measurements for varying amounts of added phospholipid were collected at temperatures in the range 15–40°C. Data in each replicate

set, where a set is defined as measurements for a single experimental run on a given day, were taken at the same temperature from 11.7 mL vials containing 46.5 nmol of total limonene. With 2 mL liquid and 9.7 mL vapor in the vial at our chosen experimental conditions, this limonene amount would correspond to a 3.2 μM aqueous concentration for a micelle-free system at room temperature— or about 3% of limonene's reported water solubility limit (Massaldi and King, 1973). One may also derive the maximum concentration that would pertain if all solute was to reside in the liquid. This amounts to a concentration of 23 μM which is still well below the aqueous solubility limit for limonene as reported in the literature (see Table 2.6).

As discussed in Chapter 1, the equilibrium distribution of limonene between the micelle collective "pseudo-phase" and the surrounding water can be described by an equilibrium constant, K_{mw}. As is the case with Henry's constant, K_{mw} is a thermodynamic quantity that should remain constant for a range of limonene concentrations, as long as conditions of an ideal-dilute solution, in both aqueous and micellar domains, is met. A brief description of the approach is given below. The mode of analysis closely follows the approach given in and Lloyd et al. (2011b).

Consider a chamber containing an analyte, water, vapor, and surfactant present at high enough concentrations such that micelles form. At equilibrium, the analyte (i) will distribute between the vapor, water, and the micelle "pseudo-phase". A total mole balance on the analyte can be written as a sum of the moles of analyte in each of these domains:

$$n_{i,t} = n_{i,v} + n_{i,w} + n_{i,m}, \tag{3.1}$$

where $n_{i,v}$, $n_{i,w}$, and $n_{i,m}$ represent the moles of analyte in vapor, dissolved in the aqueous continuum, and within micelles, respectively. $n_{i,t}$ is the total moles of analyte in the closed system. The above equation can be partially rewritten in terms of the concentration of analyte in the vapor,

$c_{i,v}$, and concentration of analyte in the water, $c_{i,w}$, by using the volume of the vapor and liquid phases, V_v and V_w, respectively. Thus, Equation (3.1) becomes

$$n_{i,t} = c_{i,v}V_v + c_{i,w}V_w + n_{i,m}. \tag{3.2}$$

To represent the last term in Equation (3.2), it is convenient to use mole fractions instead of concentrations. Since micelles are expected to consist entirely of surfactant and limonene molecules, the mole fraction of analyte in micelles, $x_{i,m}$, can be directly written as,

$$x_{i,m} = \frac{n_{i,m}}{n_{i,m} + n_{s,m}}, \tag{3.3}$$

where $n_{s,m}$ represents the number of moles of surfactant present in micelles. Explicitly solving for $n_{s,m}$ in Equation (3.3) and substituting into the mole balance in Equation (3.2) gives:

$$n_{i,t} = c_{i,v}V_v + c_{i,w}V_w + \frac{x_{i,m}}{1 - x_{i,m}} n_{s,m}, \tag{3.4}$$

where

$$n_{s,m} = \big(c_{s,t} - cmc\big)V_w, \tag{3.5}$$

and $c_{s,t}$ is the total concentration of surfactant in solution. Next, a pair of solute partition coefficients are introduced. The micelle-water partition coefficient is defined to represent the distribution between micelles and that dissolved in the aqueous continuum:

$$K_{mw} = x_{i,m}/c_{i,w} \approx \bar{v}_w \widehat{K}_{mw}. \tag{3.6}$$

where $x_{i,m}$ is approximated as $\bar{v}_w c_{i,w}$ and $\widehat{K}_{mw}$ represents a dimensionless partition coefficient as a ratio of mole fractions, $\widehat{K}_{mw} = x_{i,m}/x_{i,w}$. This definition has been used in several previous studies (Nagarajan, 1996; Saito et al., 1993). As introduced in Chapter 2, for distribution between the headspace and the aqueous continuum, the vapor-water partition coefficient is defined as

$$K_{vw} = c_{i,v}/c_{i,w}. \tag{3.7}$$

In Equations (3.6) and (3.7), $c_{i,v}$ and $c_{i,w}$ represent the molar concentrations in the vapor and dissolved in water in the liquid.

Substituting Equations (3.5)–(3.7) into the mole balance in Equation (3.1), allows us to rewrite Equation (3.1) as

$$n_{i,t} = c_{i,v}V_v + \frac{c_{i,v}V_w}{K_{Vw}} + \frac{\frac{K_{mw}}{K_{vw}}c_{i,v}V_v}{1 - \frac{K_{mw}}{K_{vw}}c_{i,v}V_v}\left(c_{s,t} - cmc\right). \tag{3.8}$$

Note that, if the concentration of analyte is sufficiently dilute, then $1 - x_{i,m} \equiv 1 - \frac{K_{mw}}{K_{vw}}c_{i,v}V_v \approx 1$ is a close approximation. Applying this approximation and solving explicitly for $c_{i,v}$ gives

$$c_{i,v} = \frac{n_{i,t}K_{vw}}{\left(K_{mw}\left(c_{s,t} - cmc\right) + 1\right)V_w + V_vK_{vw}}. \tag{3.9}$$

In our experiments, $c_{i,v}$ is related to the measured peak area (A) by a proportionality constant k $\left(c_{i,v} = kA\right)$. Thus, Equation (3.9) may be used directly if the experimental design parameters $n_{i,t}$, V_w and V_v are chosen and held constant and if $c_{s,t}$ is varied. K_{vw} and the cmc can be measured or found from the literature, and, in principle, k could be found by independent calibration of the SPME fiber. It is emphasized that the above equation is valid only above the cmc. However, in the absence of surfactant, Equation (3.9) can be reduced to

$$c_{i,v}^{o} = \frac{n_{i,t}K_{vw}}{V_w + V_vK_{vw}}, \tag{3.10}$$

which is essentially a restatement of Equation (2.26). If vapor-liquid partitioning measurements are not influenced by the presence of free surfactant monomer, Equation (3.10) also holds for concentrations of surfactant below the cmc. Division of Equation (3.9) by Equation (3.10) allows us to eliminate the experimental parameter, k. Finally, our working equation becomes

$$\frac{c_{i,v}}{c_{i,v}^{o}} = \frac{1 + K_{vw}V_v/V_w}{K_{mw}(c_{s,t} - cmc) + K_{vw}V_v/V_w + 1'} \tag{3.11}$$

where the left-hand side represents the vapor concentration when micelles are present relative to that when the micelles are absent. Equation (3.11) can alternatively expressed as

$$\frac{c_{i,v}}{c_{i,v}^{o}} = \frac{\hat{V}}{K_{mw}(c_{s,t} - cmc) + \hat{V}'} \tag{3.12}$$

where $\hat{V} = 1 + K_{vw}V_v/V_w$ is an effective dimensionless volume representing capacity for dissolved solute.

In principle, two measurements are then required to calculate K_{mw}: a peak area measurement without surfactant and another peak measurement at a higher surfactant concentration where micelles exist. All other independent variables including temperature, V_w, V_v, and $n_{i,t}$, are held constant. In practice, it is desirable to collect a range of measurements and 'fit' them together to generate more robust estimates for the partition coefficient K_{mw}. The most direct manner of experimentation is then to prepare a series of sample containers in the same way, only differing in the amount of surfactant concentration. A plot of $c_{i,v}/c_{i,v}^{o}$ versus $c_{s,t}$ then provides the solubilization isotherm. A straight-forward approach for fitting this isotherm is to use standard nonlinear-regression techniques via a Levenberg-Marquardt fitting algorithm. Alternatively, Equation (3.11) could be linearized by taking its inverse, but this approach was considered to be less accurate since it transforms the data, and its errors, in a nonlinear way (Lloyd et al., 2011b).

Figure 3.1 shows a representative solubilization isotherm in which limonene peak areas are plotted against diC$_7$PC concentration. Here, values on the right vertical axis represent this sample raw data (peak areas) obtained from the GC/MS.

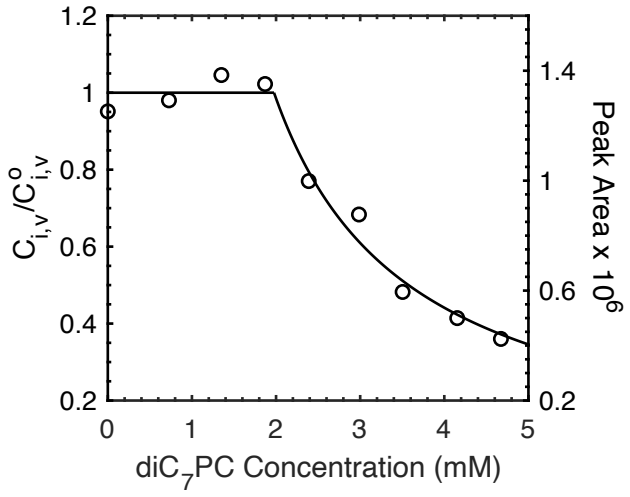

Figure 3.1. Normalized limonene vapor concentrations ($c_{i,v}/c^o_{i,v}$) and their respective peak areas at varying concentrations of diC$_7$PC

Values in Figure 3.1 are also plotted against a left axis to provide normalized peak area results of a single replicate set for each temperature. These normalized peak areas were obtained by averaging all peak areas at surfactant concentration below the apparent onset of micellization at an obvious break in the data. The surfactant concentration at the break point was subsequently compared with literature cmc values. The averaged peak areas should be proportional to the limonene concentration, denoted as $c^o_{i,v}$, for the vapor phase with no surfactant. We chose this procedure of normalization since the data below prior to the onset of micellization was found to be the same within experimental error, as that in the absence of surfactant (Lloyd et al., 2011b). The solid line indicates the best fit to Equation (3.11), above the putative cmc, when K_{mw} and the cmc were fit as adjustable parameters. The decision to leave the cmc as a fit parameter was made to improve the accuracy of the value of K_{mw} between experimental sets. Figure 3.2 contains triplicate data sets diC$_6$PC and diC$_7$PC solutions at all temperatures studied together with the curves with fitted cmc and K_{mw} values.

Table 3.2 and Table 3.3 contain fit results for K_{mw} and the cmc for limonene in diC$_6$PC and diC$_7$PC solutions at all temperatures studied. Also included is the coefficient of determination (R^2). These results indicate K_{mw} is on the order of 10^3 M^{-1} for both surfactants. We find that, in general, K_{mw} of diC$_7$PC is considerably larger than diC$_6$PC. At 15˚C, K_{mw} for diC$_7$PC is approximately 3.5× larger than that for diC$_6$PC. This difference between the two phospholipids is diminished as temperature is increased. Using dimensionless $\widehat{K}_{mw}$ (Equation (3.6)), we obtain large values of 6×10^4–8×10^4 for diC$_6$PCand 1.4×10^5–2.2×10^5 for diC$_7$PC, which are consistent with the hydrophobicity of limonene (Fieber et al., 2018). Figure 3.3 shows our results for K_{mw} for limonene partitioning into either diC$_6$PC or diC$_7$PC as a function of temperature.

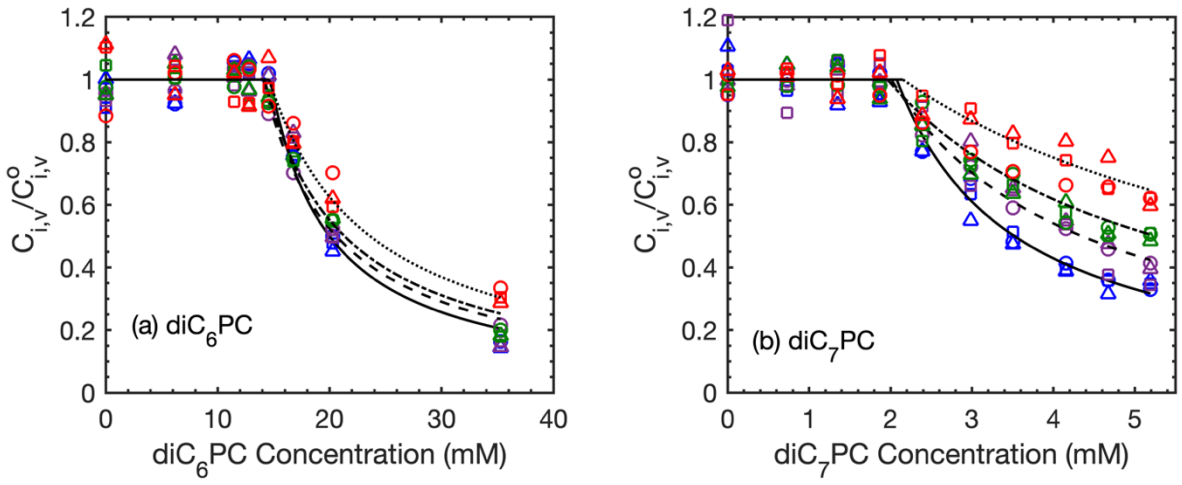

Figure 3.2. Limonene vapor phase concentration replicate sets (○, □, Δ) taken above (a) diC$_6$PC or (b) diC$_7$PC solutions, presented as a ratio of data taken in the presence ($c_{i,v}$) and the absence ($c^o_{i,v}$) of micelles, at 15˚C (blue, —); 23˚C (purple, – –); 30˚C (green, – ·); or 40˚C (red, ····). Curves are predictions from Equation (3.11), using values $\langle K_{mw}\rangle$ and $\langle cmc\rangle$ from Table 3.2 or Table 3.3

Table 3.2. Partition coefficient and cmc results from fits of Equation (3.11) to vapor phase data from diC_6PC solutions of varying concentration and a fixed low concentration of limonene

Temperature (˚C)	cmc (mM)	K_{mw} ($\times 10^3$ M^{-1})	R^2_{adj}	$\langle cmc \rangle$ (mM)[a]	$\langle K_{mw} \rangle$ ($\times 10^3$ M^{-1})[a]
(15.0±0.5)	14.72±0.18	1.05±0.12	0.989	14.70±0.13	1.089±0.098
	14.58±0.38	1.02±0.23	0.959		
	14.70±0.23	1.16±0.18	0.98		
(23±1)	13.78±0.19	1.14±0.08	0.995	14.08±0.16	1.158±0.075
	14.63±0.40	1.26±0.28	0.958		
	14.81±0.39	1.30±0.30	0.954		
(30±0.5)	14.12±0.32	1.50±0.20	0.983	14.20±0.22	1.46±0.14
	14.19±0.38	1.57±0.26	0.975		
	14.36±0.46	1.50±0.31	0.962		
(40±0.5)	13.89±0.75	1.08±0.21	0.957	14.587±0.086	1.567±0.054
	14.34±0.11	1.558±0.063	0.998		
	15.01±0.14	1.75±0.12	0.995		

[a] Errors represent standard error of the mean

Table 3.3. Partition coefficient and cmc results from fits of Equation (3.11) to vapor phase data from diC_7PC solutions of varying concentration and a fixed low concentration of limonene.

Temperature (˚C)	cmc (mM)	K_{mw} ($\times 10^3$ M^{-1})	R^2_{adj}	$\langle cmc \rangle$ (mM)[a]	$\langle K_{mw} \rangle$ ($\times 10^3$ M^{-1})[a]
(15.0±0.5)	1.92±0.052	3.42±0.25	0.978	2.078±0.031	3.93±0.20
	2.15±0.042	3.97±0.19	0.991		
	1.93±0.11	3.98±0.39	0.95		
(23±1)	1.921±0.076	3.16±0.18	0.986	2.011±0.060	3.23±0.16
	2.21±0.13	4.15±0.57	0.932		
	2.10±0.15	3.10±0.41	0.934		
(30±0.5)	2.13±0.10	3.69±0.32	0.967	1.962±0.069	3.16±0.16
	1.74±0.14	2.84±0.24	0.968		
	1.87±0.13	3.18±0.28	0.964		
(40±0.5)	1.65±0.14	2.53±0.20	0.968	2.152±0.090	2.54±0.15
	2.25±0.12	2.82±0.27	0.96		
	1.91±0.27	2.06±0.37	0.845		

[a] Errors represent standard error of the mean

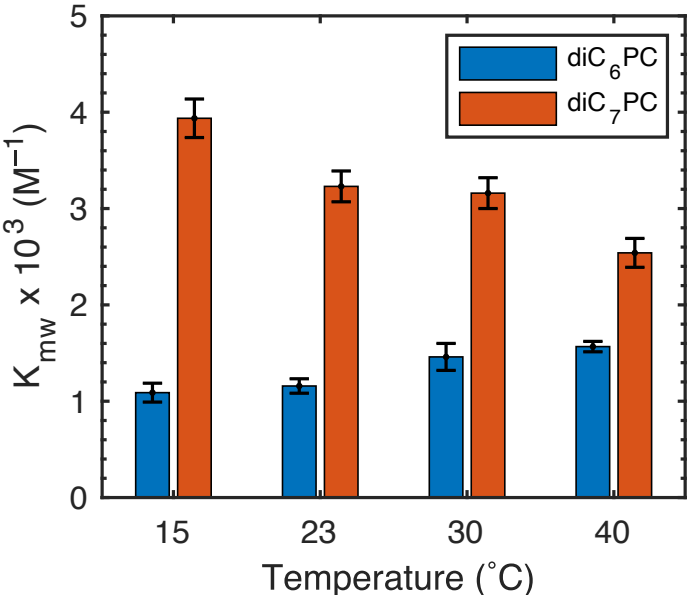

Figure 3.3. K_{mw} values for limonene in solutions of diC_6PC or diC_7PC at different temperatures. Error bars indicate the standard error of the mean

Our K_{mw} values for limonene in PC micelles can be compared to partitioning in other micellar solutions. Table 3.4 compares our results with polyethylene oxide surfactants ($C_{16}E_m$) (Tokuoka et al., 1994, 1992) and SDS (Abe et al., 1990; Lloyd et al., 2011b). Tokuoka et al. (1992,1994) measured maximum solubilization of limonene at various concentration. From their data, we were able to calculate the maximum mole fraction of limonene in micelles and divide it by our limonene solubility concentration to obtain an estimate of K_{mw}. In doing, so a direct comparison is made possible. Lloyd et al. (2011b), obtained K_{mw} using HS–SPME procedures described in this study. Despite obvious differences in these surfactants' properties (head group, single versus double tail), the obtained partition coefficients are remarkably similar, suggesting that K_{mw} is largely determined by the size and hydrophobicity of the limonene solute rather than the surfactant's structure alone.

Table 3.4. Values for K_{mw} for limonene solubilization in different surfactant solutions

	K_{mw} (M^{-1})		
Surfactant	23°C	30°C	Reference
diC_6PC	1.16×10^3	1.46×10^3	This work
diC_7PC	3.23×10^3	3.16×10^3	This work
$C_{16}E_{20}$	—	3.3×10^3	Tokuoka et al., 1994, 1992
$C_{16}E_{40}$	—	2.0×10^3	Tokuoka et al., 1994, 1992
SDS	—	1.2×10^3	Abe et al., 1990
SDS	1.7×10^3	—	Lloyd et al., 2011b

In Table 3.5, our experimental cmc values measured at room temperature for phospholipid in water are presented alongside published literature values for similar mixtures in buffer or water. For both phospholipids, there is close agreement between our values and those previously published at 25°C. Heerklotz et al. (2001) measured cmc using isothermal calorimetry techniques over a wider temperature interval. Consistent with findings of this work, their results showed a weak relationship between the critical micelle concentration and solution temperature. While effects of solubilized limonene on the cmc have been reported in aqueous nonionic micellar solutions (Tokuoka et al., 1994), these studies were conducted at solute concentrations at or near maximum solubility concentrations.

Table 3.5. The results of our cmc measurements for both diC_6PC and diC_7PC, presented alongside values from the literature at 25°C

	cmc (mM)	Literature cmc (mM)	Notes	Sources
diC_6PC	14.24 ±0.57	14.6	surface tension, 10^{-2}M PBS, 6.9pH	Tausk et al. (1974)
		13.8	light scattering, 10^{-2}M PBS, 6.9 pH	Tausk et al. (1974)
		15.2	small-angle neutron scattering	Lin et al. (1986)
		16±2	calorimetry	Jonson et al. (1981)
		15	calorimetry	Heerklotz et al. (2001)
diC_7PC	2.011 ±0.060	1.42	surface tension, 10^{-2}M PBS, 6.9pH	Tausk et al. (1974)
		1.60	light scattering, 10^{-2}M PBS, 6.9 pH	Tausk et al. (1974)
		1.8	absorbance in rhodamine 6G, 0.1M NaCl, pH 7.0	Bonsen et al (1972)
		1.9	calorimetry	Heerklotz et al. (2001)

3.3.1.1 Solute Concentration Effects at Low Limonene Concentration

Recall that in developing Equation (3.9), an important assumption was that $1 - x_{i,m} \approx 1$ or, alternatively, $x_{i,m} \ll 1$. Equation (3.11) tells us the vapor concentration prior to micellization, which we will denote as c_v^o. By the mole balance given in Equation (3.2) and the constant partitioning relationship given in Equation (3.7), the moles of limonene in micelles is calculated via $n_{i,m} = n_{i,t} - \left(\frac{c_{i,v}}{c_{i,v}^o}\right)\frac{c_v^o}{K_{vw}}V_w - \left(\frac{c_{i,v}}{c_{i,v}^o}\right)c_v^o V_v$. With this relationship, $x_{i,m}$ can be calculated via Equation (3.3). Table 3.6 below gives $x_{i,m}$ for diC_6PC at all four studied temperatures, which were calculated using average values of $\frac{c_v}{c_v^o}$. An analogous set of results, for diC_7PC is given in Table 3.7. For these calculations, we have estimated the cmc for diC_6PC and diC_7PC, at all temperatures, as 14.1mM and 1.9 mM, respectively. Note that these estimates make use of the assumption $x_{i,m} \ll 1$ in the determined K_{mw} values.

Table 3.6. Estimates of $x_{i,m}$ for limonene in aqueous diC$_6$PC solutions

	$x_{i,m} \times 10^{-3}$			
$(c_{s,t} - cmc)$ mM	15±0.5˚C	23±1˚C	30±0.5˚C	40±0.5˚C
0.45	0.51	0.98	3.80	0.51
2.66	2.12	1.61	2.22	1.78
6.18	2.06	1.89	1.69	1.43
21.18	0.94	0.92	0.88	0.78

Table 3.7. Estimates of $x_{i,m}$ for limonene in aqueous diC$_7$PC solutions

	$x_{i,m} \times 10^{-3}$			
$(c_{s,t} - cmc)$ mM	15±0.5˚C	23±1˚C	30±0.5˚C	40±0.5˚C
0.49	10.77	8.35	5.78	5.44
1.09	9.56	5.92	5.98	2.72
1.60	7.36	5.75	4.83	2.43
2.25	6.28	4.89	3.84	2.03
2.77	6.94	5.49	4.85	2.54
3.29	4.52	4.12	3.52	2.84

From the tables above we find that $x_{i,m}$ never exceeds 0.004 for diC$_6$PC or 0.011for diC$_7$PC based on our calculations. The lower the total limonene content at fixed PC concentration, the smaller the values of $x_{i,m}$, and the better we satisfy the constraint of $x_{i,m} \ll 1$. However, it should be noted that $n_{i,t}$ cannot be chosen to be arbitrarily small. An obvious limitation is that there must be enough solute present to generate a sufficient signal for quantitative analysis. One might also consider depletion effects, in which a substantial amount of solute is absorbed to the fiber, relative to the amount in the vapor. If depletion effects were present, the amount absorbed to the fiber may no longer be proportional to $c_{i,v}$ as the fiber would be "pulling" solute out from the liquid during the duration of the extraction step of the measurement. Lloyd et al. (2011a) theoretically examined the scenario in detail in which the limiting step for extraction was diffusion of solute out of the liquid. These authors calculated the theoretical amount of time for solute to diffuse out of the liquid such that it would be within 1% of the amount initially present in the vapor. It was determined that for

compounds in which K_{vw} was very small (i.e., less than 0.1) the necessary extraction times would be so small that they would be inaccessible in practice. However, by choosing 46.5 nmol, our range of solute concentrations in vapor are close to those given in Chapter 2, in which the derived K_{vw} values were in good agreement with the literature.

We decided that varying $n_{i,t}$ at concentrations further below the water solubility limit and comparing the obtained K_{mw} was a worthwhile endeavor. Figure 3.4 shows the solubilization isotherms, analogous to those given in Figure 3.2. Here, the solute concentrations were fixed at 4.65 nmol. This amount of solute is one order of magnitude smaller than was used previously. There was no significant statistical difference between K_{mw} and cmc acquired using 46.5 nmol and 4.65 nmol of limonene. This suggests the solutions were sufficiently dilute in limonene to satisfy the approximation of $x_{i,mic} \ll 1$, and that solute partitioning was not affected by $x_{i,m}$ at these dilute concentrations. We will investigate potential solute concentration effects in §3.32.

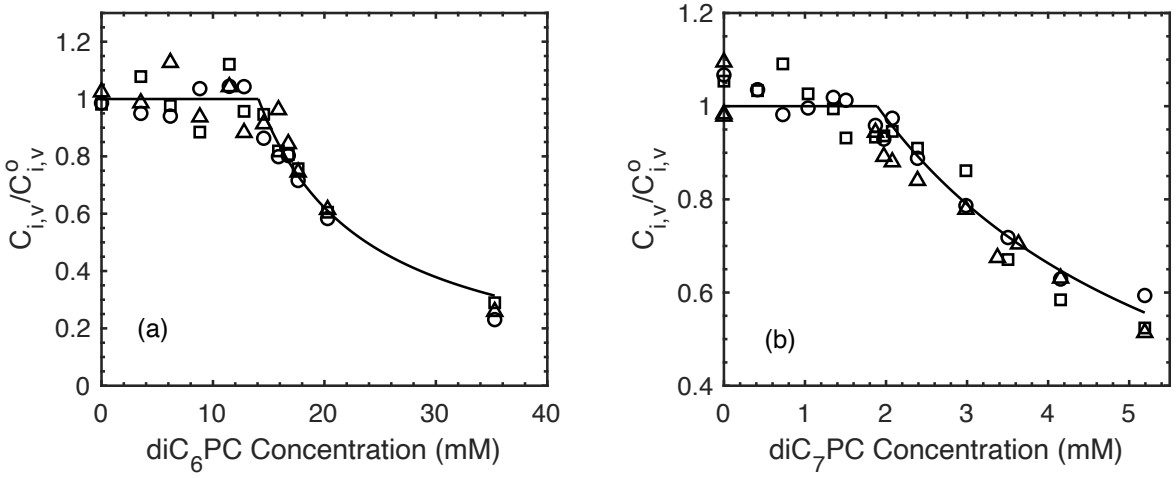

Figure 3.4. Solubilization isotherms for (a) diC$_6$PC and (b) diC$_7$PC at room temperature conditions

Table 3.8. cmc and K_{mw} values as obtained from data in Figure 3.4. Averages and goodness of fit metrics also given.

	cmc (mM)	K_{mw}(M^{-1})×10^3	R^2_{adj}	$\langle cmc \rangle$(mM)	$\langle K_{mw} \rangle$(M^{-1})×10^3
diC_6PC	13.65±0.55	1.51±0.25	0.953	14.07±0.37	1.42±0.18
	14.09±0.23	1.38±0.11	0.989		
	14.43±0.54	1.43±0.30	0.929		
diC_7PC	1.90±0.086	3.22±0.23	0.987	1.88±0.10	3.31±0.33
	1.87±0.14	3.63±0.52	0.921		

3.3.2 Solubilization Isotherms with Varying Limonene Content at Fixed [diC_6PC] or [diC_7PC]

In this section on solubilization, we again examine the vapor-liquid partitioning behavior of limonene in aqueous solutions consisting of either diC_6PC or diC_7PC micelles. In these sets of experiments, however, limonene is varied to probe higher concentrations up to its solubility limit, while surfactant concentration is fixed. By doing so, we can construct sets of solubilization isotherms at higher solute loadings and evaluate how micelle-water partitioning under these conditions compares to results obtained at low limonene concentrations.

Figure 3.5 presents a single replicate peak area measurement set plotted against the total amount of added limonene (in μmol) for solutions containing 5.2 mM of dissolved diC_7PC. It can be seen that addition of limonene up to 3.6 μmol led to larger peak areas from the headspace. Further addition of limonene beyond that point resulted in a break in this trend, with nearly constant peak areas at the highest amounts of limonene. As with the maximum solubility results (§2.3.5), a break in concentration, beyond which peak area measurements do not appreciably change with added limonene, indicates solution saturation and consequent formation of a separate bulk phase of limonene. A constant vapor pressure above these saturated solutions was therefore also established.

For experiments such as those presented in Figure 3.5, an additional measurement from vials containing water saturated with limonene was taken with each data set. These vials acted as a reference standard by which we could determine whether the solution's solubility limit had been reached. Agreement between the peak area measurements above phospholipid solutions that were saturated with limonene, and those acquired from saturated vials in the absence of phospholipid, was generally close, usually well within 5%.

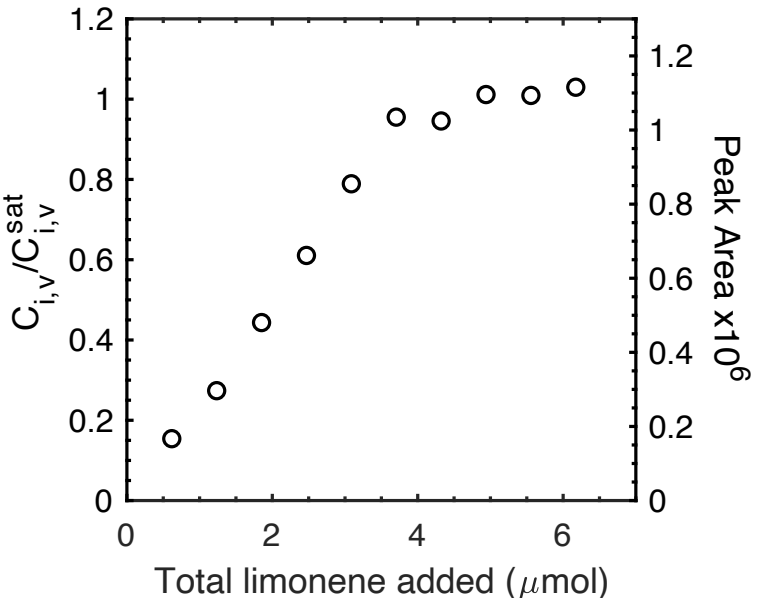

Figure 3.5. Peak areas and normalized vapor-phase concentrations for limonene above 5.2mM diC$_7$PC solutions, measured at 40˚C in a single day set of 11.70±0.20 mL vials. Liquid volume was 2 mL

To use this data to determine effects of composition on the limonene vapor concentration, peak area measurements were normalized with values corresponding to saturated limonene solutions, yielding the vapor concentration ratio $c_{i,v}/c_{i,v}^{sat}$. For diC$_6$PC and diC$_7$PC measurements taken at ambient conditions, each replicate set was normalized by a single saturated water solution reference standard measured on the same day. We observed satisfactory agreement between replicate sets using this procedure. For clarity, a replicate set represents a series of measurements which were taken on a

single day; different replicate set values are indicated by different symbols in Figure 3.6(○, □, Δ, ▷, ▽). For replicate peak area sets shown in Figure 3.6 (b,d) for 40˚C (○, □, Δ), the results for the reference standard were averaged together with measurements of phospholipid solutions saturated with limonene. Data from at least four phospholipid solutions beyond the break point—i.e., apparently saturated—were averaged with the reference standard at this higher temperature. This procedure was done to obtain a better estimate of the true saturated peak area, and it generally led to better agreement between normalized data set replicates. Comparisons between the averaged peak areas that include the saturated phospholipid solutions and those of the reference standard alone are shown in Table 3.9 below for each replicate set.

Table 3.9. Comparison of averaged peak areas versus reference measurements at 40˚C.

	Peak Area×10^6			
	diC_6PC		diC_7PC	
	Average of Saturated Solution with Phospholipid	Saturated Reference	Average of Saturated Solution with Phospholipid	Saturated Reference
Set 1	3.557±0.093 (n=4)	3.344	1.260±0.046 (n=5)	1.211
Set 2	3.389±0.17 (n=4)	3.647	2.470±0.066 (n=4)	2.550
Set 3	—	—	6.615±0.015 (n=4)	6.643

[a]All averages used four apparently saturated measurements except for diC_7PC set 1, which used five.

Figure 3.6 presents combined data sets for all system conditions analyzed using this approach. Solubilization isotherms were obtained at both room temperature and 40˚C. For each pair of isotherm results for a given phospholipid (i.e. room temperature and 40˚C), experiments were performed using identical phospholipid concentrations and fill fractions. These phospholipid concentrations were selected to be approximately 2.5 times their respective cmc values.

From the plots in Figure 3.6, we can make some general observations. First, we see that increasing the temperature generally leads to a decrease in apparent solubility. Second, the increase in peak area with increasing solute appears to be non-linear at room temperature, and more linear at 40˚C. Both trends will be evaluated more thoroughly in the upcoming paragraphs.

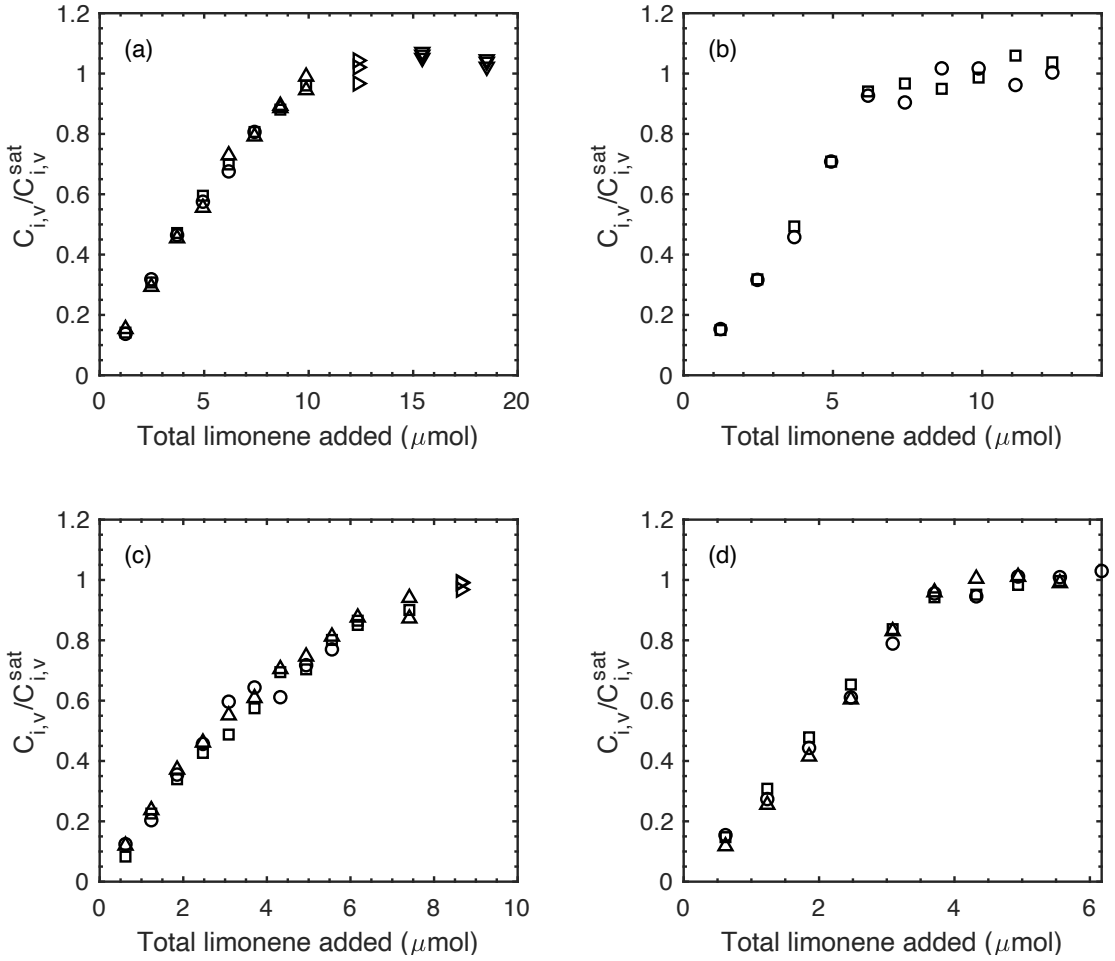

Figure 3.6. Replicate peak areas sets (○, □, Δ, ▷, ▽) normalized by saturated peak areas for limonene in vapor above solutions of 35.2 mM diC_6PC at (a) room temperature and (b) at 40±0.5˚C; and 5.2mM diC_7PC at (c) room temperature and (d) 40±0.5˚C. Measurements in (a) and (b) were made in 21.70±0.2 mL vials containing 1mL of aqueous diC_6PC. In (c) and (d), 11.70±0.2 mL vials were used containing 2 mL of aqueous diC_7PC

We first examine whether our previously determined K_{mw} values, obtained at low limonene concentrations and presented in §3.3.1 accurately predict the new measurements taken at higher limonene concentration. To make this comparison, we again utilize a mole balance to determine $c_{i,v}/c_{i,v}^{sat}$ as a function of solute concentration. At higher amounts of limonene in solution, we must consider the possibility that the corresponding mole fraction $x_{i,m}$ of limonene in micelles is no longer negligibly small. Substituting Equations (3.4)–(3.7) into the mole balance in Equation (3.2) without using the approximation $1 - x_{i,m} \approx 1$, and then solving for $c_{i,v}$, gives

$$c_{i,v} = \frac{n_{i,t}K_{vw}}{\frac{K_{mw}}{1 - K_{mw}c_{i,w}}n_{s,m} + V_v K_{vw} + V_w}. \tag{3.13}$$

Our vapor measurements are normalized by values $c_{i,v}^{sat}$ that were obtained above a saturated solution. The latter can be related to aqueous concentrations of limonene at the solubility limit using K_{vw}, assuming this coefficient is constant at all concentrations. With some rearrangement, we then obtain the following:

$$\frac{c_{i,v}}{c_{i,v}^{sat}} = \frac{n_{i,t}}{c_{i,w}^{sat}V_w\left(\frac{K_{mw}}{1 - K_{mw}c_{i,w}^{sat}c_{i,v}/c_{i,v}^{sat}}\left(c_{s,t} - cmc\right) + K_{vw}\frac{V_v}{V_w} + 1\right)} \tag{3.14}$$

or

$$\hat{c}_i = \frac{\hat{n}_{i,t}}{\left(\frac{K_{mw}c_{s,m}}{1 - x_{i,m}^{sat}\hat{c}_i} + \hat{V}\right)}, \tag{3.15}$$

with $\hat{c}_i = c_{i,v}/c_{i,v}^{sat}$. Here, $\hat{n}_{i,t} = n_{i,t}/(c_{i,\mathrm{w}}^{sat}V_w)$ is the ratio of total solute moles added, relative to the moles at saturation dissolved in the water continuum, and $\hat{V}$ follows the same definition given in §3.31. Here $c_{s,m} = c_{s,t} - cmc$ and $x_{i,m}^{sat} = K_{mw}c_{i,w}^{sat}$ represents the mole faction of solute within

micelles at the solubility limit. The latter quantity is also related to the so-called molar solubilization ratio (MSR) at saturation, where

$$MSR = \frac{n_{i,m}}{n_{s,m}} = \frac{x_{i,m}^{sat}}{1 - x_{i,m}^{sat}}. \tag{3.16}$$

Moving all of the terms in Equation (3.15) to the left-hand side of the equation gives

$$x_{i,m}^{sat}\hat{V}\hat{c}_i^2 - \hat{c}_i\left[K_{mw}c_{s,mic} + \hat{V} + \hat{n}_{i,t}x_{i,m}^{sat}\right] + \hat{n}_{i,t} = 0. \tag{3.17}$$

$\hat{c}_i$ can then be solved for explicitly by making use of the quadratic formula. That is,

$$\hat{c}_i = \frac{c_{i,v}}{c_{i,v}^{sat}} = \frac{\left(B - \sqrt{B^2 - 4AC}\right)}{2A}, \tag{3.18a}$$

where

$$A \equiv x_{i,m}^{sat}\hat{V}, \tag{3.18b}$$

$$B \equiv K_{mw}c_{s,m} + \hat{V} + \hat{n}_{i,t}x_{i,m}^{sat}, \tag{3.18c}$$

and

$$C \equiv \hat{n}_{i,t}. \tag{3.18d}$$

Equation 3.18 allows us to predict $c_{i,v}/c_{i,v}^{sat}$ using known values for K_{vw}, cmc, $c_{i,w}^{sat}$, and K_{mw}. We also note that, in the limiting case where there is no micellized surfactant, Equation (3.14) reduces to

$$\hat{c}_i = \frac{c_{i,v}}{c_{i,v}^{sat}} = \frac{n_{i,t}}{c_{i,w}^{sat}(K_{vw}V_v + V_w)} = \frac{\hat{n}_{i,t}}{\hat{V}}. \tag{3.19}$$

The analysis presented above allows us to define a set of three regimes within each solubilization isotherm:

- Regime I, where

$$n_{i,t} < c_{i,w}^{sat}(K_{vw}V_v + V_w),$$

and the added limonene would be soluble within pure water alone;

- Regime II, where

$$c_{i,w}^{sat}(K_{vw}V_v + V_w) < n_{i,t} < c_{i,w}^{sat}V_w\left(\frac{K_{mw}}{1-K_{mw}}\left(c_{s,t} - cmc\right) + K_{vw}\frac{V_v}{V_w} + 1\right),$$

and the added limonene is in excess of its solubility limit in water alone, but can still be solubilized by the phospholipid micelles;

- Regime III, where

$$n_{i,t} > c_{i,w}^{sat}V_w\left(\frac{K_{mw}}{1-K_{mw}}\left(c_{s,t} - cmc\right) + K_{vw}\frac{V_v}{V_w} + 1\right),$$

in which the amount of limonene exceeds the solubilization capacity of the phospholipid micelles and an excess bulk limonene phase forms.

These limits may also be given in dimensionless form:

- Regime I: $\hat{n}_{i,t} < \hat{V}$;
- Regime II: $\hat{V} < \hat{n}_{i,t} < \frac{K_{mw}c_{s,m}}{1-x_{i,m}^{sat}\hat{c}_i} + \hat{V}$;
- Regime III: $\hat{n}_{i,t} > \frac{K_{mw}c_{s,m}}{1-x_{i,m}^{sat}\hat{c}_i} + \hat{V}$.

Figure 3.7 presents the solubilization isotherms, with each of the three regimes labeled appropriately. Calculated values for $c_{i,v}/c_{i,v}^{sat}$, based on Equations (3.18) and (3.19), are represented as dashed lines. The blue line gives the predictions of $c_{i,v}/c_{i,v}^{sat}$ if micelles are not present (Equation (3.19)), while the red line predicts this ratio in the presence of micelles (Equation (3.18)) with K_{mw} assumed constant at the value K_{mw}^{I} obtained at very low limonene concentrations overall, for which $\hat{n}_{i,t}$ =0.23. The parameters K_{vw}, $c_{i,w}^{sat}$ and cmc, that were used in calculating the dashed line predictions, are presented in Table 2.2 and Table 2.6. K_{mw} values used in these predictions are given in Table 3.2 and Table 3.3. We have assumed that these two terms do not change with free monomer of surfactant outside of micelles.

In Figure 3.7 (a–d), the blue dashed lines predict solubilization behavior for limonene in the absence of surfactant (Regime I). As expected, we see that saturation occurs above a lower $n_{i,t}$ than that observed in measurements with solutions containing surfactant. Thus, the difference between measurements and the blue dashed lines directly shows the effect that micelles have on the apparent solubility of limonene. In the same figure, predictions shown as red dashed lines, which were made with Equation (3.18), show the expected solubilization isotherm if K_{mw} can be assumed constant at K_{mw}^{I} (Regime II). Recall these constant K_{mw} values were obtained at very low limonene concentrations ($n_{i,t} \ll 1$). For measurements taken at room temperature, Figure 3.7(a,c), it is seen that the vapor concentrations fall well below predictions from constant K_{mw}^{I} values (red dashed line), for both phospholipids studied. This indicates that limonene is taken up by micelles over a greater range than predicted by Regime II, extending well into the predicted saturated regime (Regime III). In fact, for both phospholipids at room temperature, the maximum amount of limonene which may be solubilized is nearly twice as large as that predicted from dilute partitioning values. In contrast, at 40°C the constant $K_{mw} = K_{mw}^{I}$ values determined at low limonene appear to better predict measured vapor concentration at higher solute concentrations Figure 3.7(b,d).

The room temperature results in Figure 3.7 indicate stronger partitioning of limonene from water into micelles than is predicted by the constant K_{mw}^{I} values from Table 3.2 or Table 3.3 alone. To assess the strength of this effect, we directly fit our data to Equation (3.18), to obtain a best fit in K_{mw} using non-linear least squares regression. The best fit values, indicated by the purple dashed line, are shown in Figure 3.8. These best fits results, denoted as K_{mw}^{II}, are provided in Table 3.10.

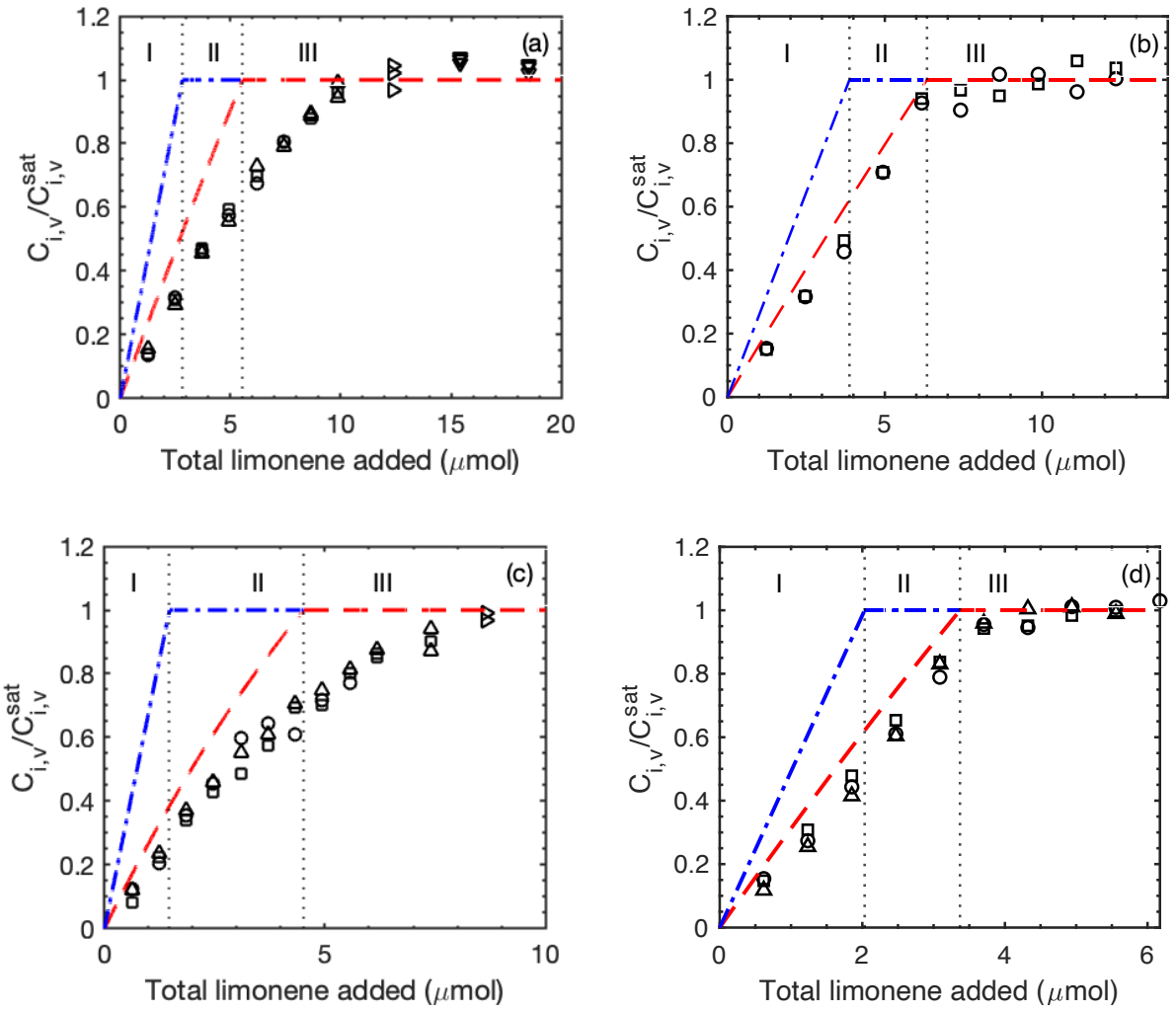

Figure 3.7. Solubilization isotherms as presented in Figure 3.6. Blue lines are predictions of Equation (3.19), while red lines are predictions of Equation (3.18) with K_{mw} equal to (a) 1200 M^{-1}, (b) 1500 M^{-1}, (c) 3200 M^{-1}, and (d) 2400 M^{-1}. Symbols (○, □, △, ▷, ▽) represent data from different replicate sets

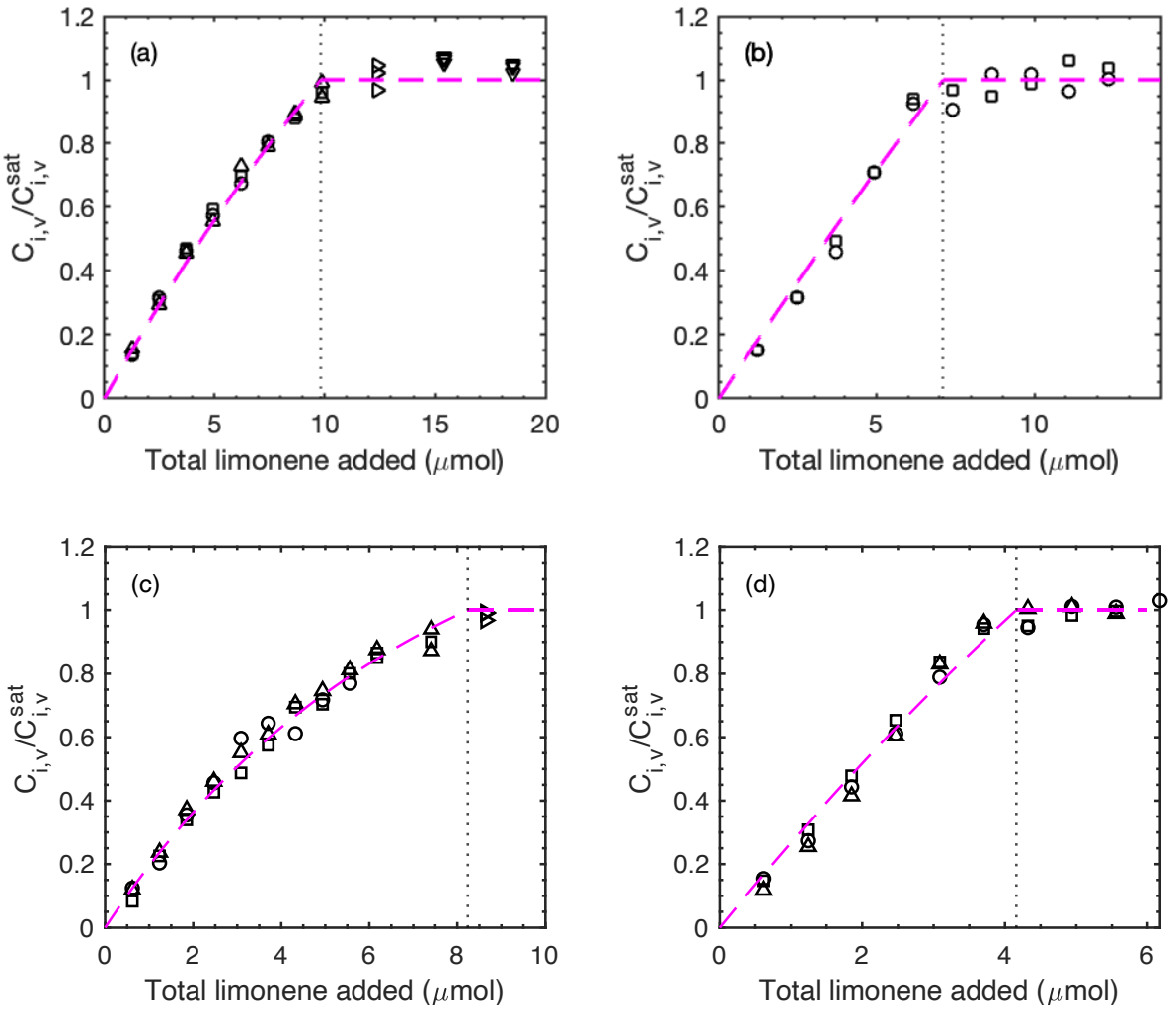

Figure 3.8. Solubilization isotherms as presented in Figure 3.6 and Figure 3.7, used to obtain new partition coefficient values (K^{II}_{mw}) for higher limonene concentration. The purple dashed line are the best fits to Equation (3.18). with K_{mw} as an adjustable parameter

Table 3.10. The best fit partition coefficient, K_{mw}^{II}, together with the maximum added amount of limonene, $\mathrm{n_{max}}$, below the onset of phase separation

	Temperature (°C)	K_{mw}^{II} (M^{-1}) $\times 10^3$	$\mathrm{n_{max}}$ (μmol)	$\mathrm{R_{adj}^2}$	$\langle K_{mw}^{II} \rangle^a$ (M^{-1}) $\times 10^3$	$\langle \mathrm{n_{max}} \rangle^a$ (μmol)
diC_6PC	23±1	2.406±0.047	9.49±0.17	0.994	2.360±0.027	9.75±0.10
		2.491±0.057	9.80±0.21	0.988		
		2.257±0.041	9.94±0.16	0.991		
	40±0.5	1.95±0.17	7.19±0.34	0.969	1.965±0.074	7.22±0.14
		2.008±0.096	7.31±0.19	0.989		
		1.87±0.15	7.05±0.28	0.977		
diC_7PC	23±1	5.08±0.16	8.19±0.45	0.966	5.108±0.048	8.26±0.13
		5.160±0.066	8.42±0.19	0.992		
		5.039±0.079	8.09±0.21	0.987		
	40±0.5	3.55±0.19	4.09±0.16	0.982	3.48±0.12	4.03±0.10
		3.38±0.16	3.96±0.12	0.988		
		3.79±0.38	4.29±0.32	0.949		

[a] Average of three replicate sets with error given as standard error of the mean.

The vertical dashed lines in Figure 3.8 mark the onset of the experimentally determined solubility limit, which was calculated by solving for $n_{i,t}$ in Equation (3.18), setting $c_{i,v}/c_{i,v}^{sat}$ equal to unity and K_{mw} to K_{mw}^{II}. From this procedure, we were able to obtain an estimate for the maximum amount of limonene n_{max} that could be added to the vial before phase separation occurred (Table 3.10). This information was then used to compute the maximum mole fraction $x_{i,m}^{sat}$ for limonene in micelles using the definition given in Equation (3.3). At the solubility limit, Equation (3.3) simply becomes

$$x_{i,m}^{sat} = \frac{n_{i,m}^{sat}}{n_{i,m}^{sat} + n_{s,m}} \tag{3.20}$$

where

$$n_{i,m}^{sat} = n_{max} - n_{i,w}^{sat} - n_{i,v}^{sat} \tag{3.21}$$

from a mole balance (Equation (3.4)). The moles of limonene needed to saturate the water, $n_{i,w}^{sat}$, was calculated using $c_{i,w}^{sat}V_w$, and the moles of limonene to saturate the vapor, $n_{i,v}^{sat}$, determined from $c_{i,w}^{sat}K_{vw}V_v$, using parameters in Table 2.2 and Table 2.6. Lastly, $n_{s,m}$ was calculated from Equation (3.5). Alternatively, one could calculate $x_{i,m}^{sat}$ by using $x_{i,m}^{sat} = K_{mw}^{II}c_{i,w}^{sat}$, from the definition given in Equation (3.6).

Table 3.11. Comparison of the maximum mole fraction, $x_{i,m}^{sat}$,for diC$_6$PC and diC$_7$PC

Solute	$x_{i,m}^{sat}$		
	Temperature (°C)	diC$_6$PC (mM)[b]	diC$_7$PC (mM)[b]
Limonene (This work)	23±1	0.25 (35.2mM)	0.51 (5.2 mM)
	30	0.17[a] (35.2mM)	0.32[a] (5.2mM)
	40±0.5	0.13 (35.2mM)	0.25 (5.2mM)
Tributyrin (Burns et al., 1983)	30	0.16 (80mM)	0.36±0.02 (80mM)
Trihexanoin (Burns et al., 1983)	30	—	0.20±0.03 (80mM)

[a] Values obtained by linear interpolation of values measured at 23°C and 40°C
[b] Values in parentheses correspond to the concentration of surfactant in the study

As can be seen from Table 3.11, $x_{i,m}^{sat}$ was larger for micelles diC$_7$PC than diC$_6$PC at both temperatures. In addition, $x_{i,m}^{sat}$ decreased by approximately 50% as temperature increased from ~23°C to 40°C, with both surfactants. While we were not able to find any data describing the partitioning behavior of limonene in short-chain phosphatidylcholine micelles, values for the

maximum mole fraction at 30°C of two short-chain triacylglycerols, tributyrin and trihexanoin, were reported by Burns et al. (1983), based on NMR spectroscopy measurements. The ratio of their maximum mole fraction values, for diC_7PC relative to diC_6PC, is similar to what was obtained for limonene in this study (Table 3.11). Linear interpolation of the data in Table 3.11 to estimate $x_{i,m}^{sat}$ for limonene at 30°C yields values very close to the maximum mole fraction results for tributyrin. The value for trihexanoin is significantly smaller.

Previous researchers (Chaiko et al., 1984; Nagarajan et al., 1986) have proposed that, for hydrophobic solutes, the extent of solubilization depends primarily on the solute's molecular size and water interactions as indicated through the solute-water interfacial tension. This dependence was observed experimentally for various hydrophobic compounds dissolved in anionic, cationic, and block copolymer aqueous solutions (Chaiko et al., 1984; Nagarajan et al., 1986). In Table 3.12, we compare these physical-chemical properties for limonene, tributyrin, and trihexanoin, as well as their octanol/water partition coefficient as a measure of hydrophobicity. The comparison shows tributyrin to have a significantly larger molecular weight and volume than limonene, but the triglyceride is also more polar and less hydrophobic, due to its carbonyl groups. It may be that these different properties for tributyrin compensate each other to yield solubilization properties in the phospholipid micelles that are quite similar to those of limonene. Trihexanoin, however, exhibits similar hydrophobicity as limonene, but its molecular size is largest among all three compounds. The large size difference between trihexanoin and limonene could partially account for the experimentally observed smaller maximum extent of solubilization in the case of trihexanoin.

In Chapter 4, we discuss a dimensionless volume polarity parameter first proposed by Ruckenstein et al. (1983) as a useful tool for predicting maximum solubilization for various hydrophobic solutes dissolved in aqueous systems. To our knowledge, this approach has never been

applied to zwitterionic micellar solutions, making the preliminary comparisons here of particular interest. The basis for this approach is rooted in molecular thermodynamics.

Table 3.12. Physicochemical properties of limonene and tributyrin including density (ρ), octanol-water partition coefficient (K_{ow}), molecular weight (MW), and molecular volume (ν_o), and the solute/water interfacial tension (σ_{ow})

.

	Limonene	Tributyrin	Trihexanoin	Sources
ρ (g/mL)	0.841	1.032	1.001	Lewis, 1997
$\log K_{ow}$	4.57	2.54	4.73	Li et al., 1998, Gualdesi et al., 2014
σ_{ow} (mN/m)	44±0.5	7[b]	18.6	Pérez-Mosqueda et al., 2013, Burns et al., 1983 Benerito et al., 1956
MW (g/mol)	136.24[c]	302.36[c]	386.5[c]	—
v_o (Å^3)	269[a]	487[a]	641[a]	—

[a] Calculated from density and molecular weight
[b] Estimates by Burns et al. (1983) using a procedure discussed in Donahue & Bartell (1954)
[c] Periodic table of elements

3.3.3 Quantifying Partitioning Enhancement with Increasing Solute

The results obtained from the best fits of K_{mw} to solubilization isotherms at low (K_{mw}^{I}) and high (K_{mw}^{II}) limonene concentrations indicate that K_{mw} is changing with the mole fraction of solubilized limonene within micelles, $x_{i,m}$. In all cases, $K_{mw}^{II} > K_{mw}^{I}$, suggesting that higher solute loadings within the micelle lead to enhanced partitioning. For example, one might imagine that the solubilization of limonene alters the micelle structure in such a way as to enhance its affinity and capacity for limonene.

From a thermodynamic perspective, a constant K_{mw} would be predicted if changes in chemical potential of solute with increased solute concentration are solely due to ideal-dilute mixing effects as shown in Chapter 1. However, change due to favorable (or unfavorable) enthalpic interactions between solubilized solute and its neighbors, as well as effects due to structural changes and interactions of the aggregate remains a possibility at higher solute content. Mathematically, this would amount to a changing solute activity coefficient as solute concentration is increased. As a simple

approach to capture this effect, suppose that K_{mw} increases linearly as more limonene is solubilized. In this case, K_{mw} would take on the form:

$$K_{mw} = K_{mw}^{I}\left(1 + a x_{i,m}\right). \tag{3.22}$$

K_{mw}^{I} represents the dilute partition coefficient measured at low limonene concentrations, as given in Table 3.2 and Table 3.3 and a is a dimensionless constant that quantifies the change in K_{mw} with mole fraction. Since by definition, $K_{mw} \equiv x_{i,m}/c_{i,w}$, we can solve for $x_{i,m}$ in terms of K_{mw}^{I} and $c_{i,w}$ and obtain

$$x_{i,m} = \frac{c_{i,w} K_{mw}^{I}}{1 - a c_{i,w} K_{mw}^{I}}. \tag{3.23}$$

Substitution of $x_{i,m}$ into a mole balance (Equation (3.4)) and solving for $\frac{c_{i,v}}{c_{i,v}^{sat}}$ yields

$$\frac{c_{i,v}}{c_{i,v}^{sat}} = \frac{n_{i,t}}{c_{i,w}^{sat} V_w \left(\frac{K_{mw}^{I}}{1 - K_{mw}^{I}(a+1) c_{i,w}^{sat} c_{i,v}/c_{i,v}^{sat}} \left(c_{s,t} - cmc\right) + K_{vw} \frac{V_v}{V_w} + 1 \right)}. \tag{3.24}$$

Equation (3.24) rearranges to yield a quadratic equation, with the solution

$$\frac{c_{i,v}}{c_{i,v}^{sat}} = \frac{\left(\breve{B} - \sqrt{\breve{B}^2 - 4\breve{A}\breve{C}}\right)}{2\breve{A}} \tag{3.25a}$$

These dimensionless constants $\breve{A}$, $\breve{B}$, and $\breve{C}$ are given by:

$$\breve{A} \equiv x_{i,m}^{sat,I}(a+1)\hat{V}; \tag{3.25b}$$

$$\breve{B} \equiv K_{mw}^{I} c_{s,m} + \hat{V} + \hat{n}_{i,t} x_{i,m}^{sat,I}(a+1); \tag{3.25c}$$

and

$$\breve{C} \equiv \hat{n}_{i,total}. \tag{3.25d}$$

Here, $x_{i,m}^{sat,l} = K_{mw}^{l} c_{i,w}^{sat}$, and the remaining variables are defined in § 3.3.2. Equation (3.25) was fit to the solubilization data in Figure 3.6, in order to generate best estimates for a. The resulting lines from Equation (3.25), along with the best fit values of a, are given in Figure 3.9 and Table 3.13.

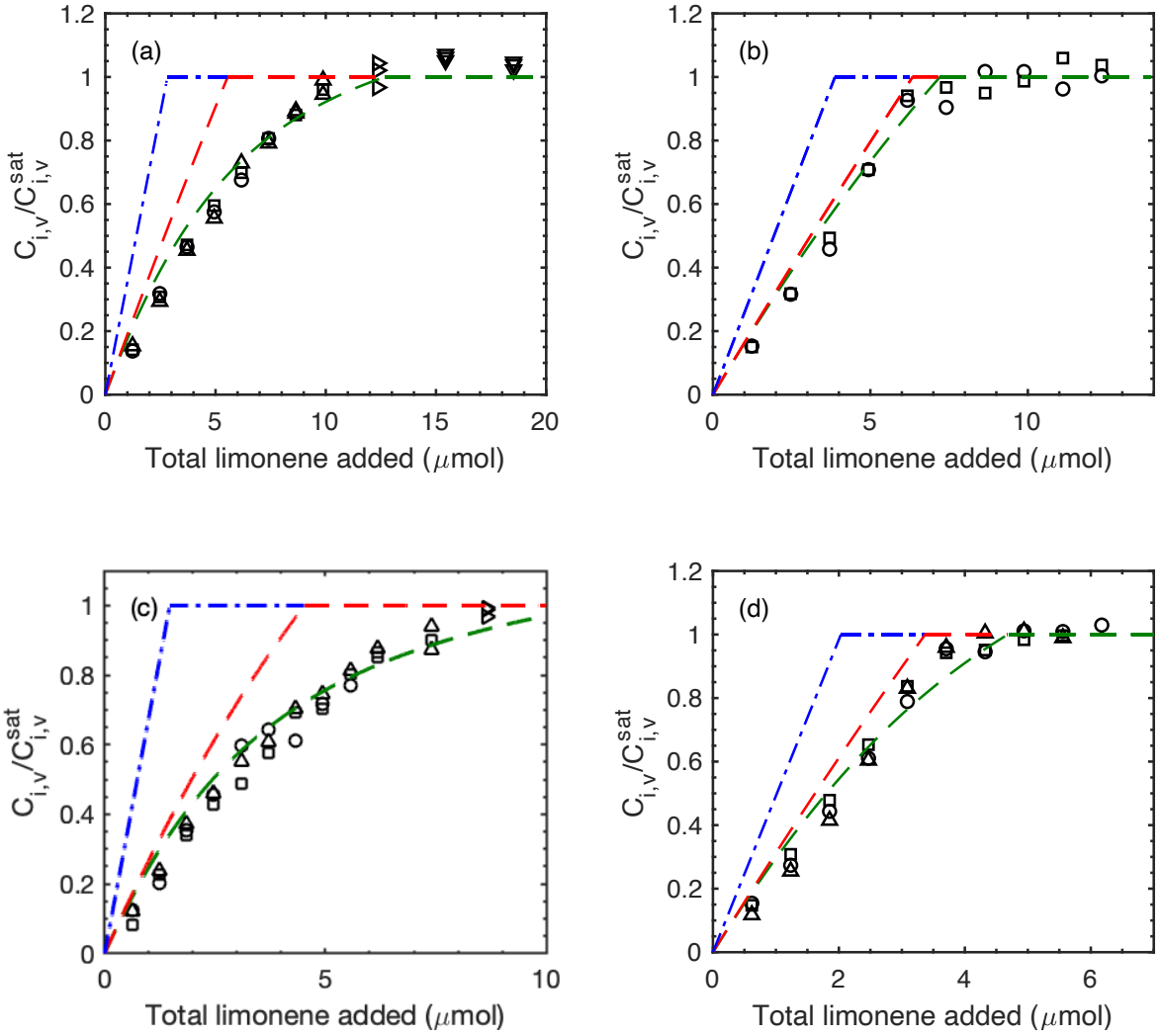

Figure 3.9. Solubilization isotherms as presented in Figure 3.6. The green dashed line are the best fits to Equation (3.25), adjusting only the parameter a. Red and blue dashed lines are the same as those given in Figure 3.7

Equation (3.25) with fit values for a describe the data in Figure 3.6 reasonably well., capturing the experimental results far better than constant K_{mw}^{I} alone. Values of a are all positive, consistent with an increase in K_{mw} as $x_{i,m}$ is increased. We also find that, in general, values of a are larger for diC$_6$PC than for diC$_7$PC micelles, suggesting that the effect of limonene in altering the micelle environment is more pronounced for the former lipid. Lastly, as temperature is increased, a decreases substantially for diC$_6$PC micelles, while a increased, albeit less appreciably, for diC$_7$PC. This may indicate that the diC$_6$PC micelles are more sensitive to changes with temperature at higher limonene concentrations.

Table 3.13. Best fit of the thermodynamic parameter a for data presented in Figure 3.9, obtained using non-linear least-squares regression analysis

	Temperature (°C)	a	R^2_{adj}	$\langle a \rangle^*$
diC$_6$PC	23±1	6.12±0.72	0.945	5.30±0.40
		5.21±0.35	0.964	
		5.03±0.30	0.956	
	40±0.5	2.4±1.3	0.947	2.5±1.1
		2.0±1.1	0.961	
		2.99±0.85	0.973	
diC$_7$PC	23±1	1.74±0.16	0.958	1.51±0.11
		1.52±0.12	0.951	
		1.412±0.074	0.979	
	40±0.5	1.72±0.49	0.959	1.86±0.48
		1.87±0.36	0.976	
		2.06±0.70	0.924	

*Weight average of replicates using $1/\sigma_a^2$ as weights, where σ_a is error in a.

Although representing K_{mw} with Equation (3.22) allows us to capture solubilization trends at both high and low limonene, the resulting predictions in Figure 3.9 for $c_{i,v}/c_{i,v}^{sat}$ do not fit the data quite as well as the constant $K_{mw} = K_{mw}^{II}$ predictions in Figure 3.8. The difference between the experimental and predicted values in Figure 3.9 seems to indicate that the actual dependence of K_{mw} on limonene at these high concentrations is weaker than prescribed in Equation (3.22). It may be that

K_{mw} is constant ($K_{mw} = K_{mw}^{I}$) when the number of solutes within the micelle is so low as to not perturb the excess free energy significantly, but then non-ideal effects increase in importance as solute numbers build up, and K_{mw} increases. Finally, at higher micellar mole fractions of limonene, further addition of solute no longer substantially modifies non-ideal interactions, and K_{mw} approaches the constant K_{mw}^{II}. This behavior would lead to a more sigmoidal dependence of K_{mw} on $x_{i,m}$.

A substantial increase in K_{mw} with added limonene was also observed by Lloyd et al. (2011b) for the same solute in aqueous SDS micellar solutions. In the latter system, $x_{i,m}^{sat}$ was found to be approximately 0.5, which is quite similar to our diC_7PC results. Vane and Giroux (2000) found consistent decreases in K_{mw} with increasing temperature for various solutes in SDS solutions, including the sparingly soluble compounds trichloroethylene (TCE), toluene, 1,1,1 trichloroethane (TCA), and tetrachloroethylene (PCE). These authors determined that K_{mw} decreased by as much as 50% for the PCE/SDS system when increasing temperature from 30˚C to 40˚C, a change similar in magnitude extent to that observed with diC_6PC. Scamehorn et al. (1989) also found the maximum extent of solubilization, $x_{i,m}^{sat}$, slightly decreased in SDS/cyclohexane mixtures when temperature was changed from 15˚C to 45˚C, although the extent of change was small. However, much greater decreases in $x_{i,m}^{sat}$ were observed with the nonionic surfactant tergitol, a nonylphenol ethoxylate, in solubilizing cyclohexane, upon increasing the temperature from 15˚C to 45˚C. Thus, the substantial decreases in both micellar partition coefficient and in extent of maximum solubilization, that we observed for zwitterionic micelles as temperature was increased, appears to be a phenomenon observed widely with surfactants and is not associated with any particular headgroup type.

While the above analysis is useful for quantifying the strength of enhanced partitioning at these higher $x_{i,m}$ amounts, it does not point to an exact cause. In addition to changes in micelle structure and solute-solute interactions within the micelle core, one may also consider a depression in the critical

micelle concentration (cmc). Theoretical models proposed by Nagarajan and Ruckenstein (1991) indicate that micellization of solute can lead to a depressed cmc. They determined for very hydrophobic solutes, which was quantified using a proposed volume-polarity parameter, the cmc can decrease by as much as 50% at the solute's solubility limit for aqueous solutions of sodium dodecyl sulfate micelles. A depressed cmc would lead to more micelles than accounted for by the mole balance and would thus result in an artificially large a term. Experimental studies detailing the dependence of cmc have been published for several alkane and alcohol solutes in solution containing sodium dodecyl sulfate micelles using a fluorescence probing technique (Malliaris, 1987). While they were able to detect a cmc depression associated with polar compounds, they were not able to find any changes in cmc associated with any of the alkane solutes studied. In our analysis, it is believed that limonene does not influence the cmc to any significant extent as observed in our low solute concentration effects given in §3.3.1.1

3.3.4 Limonene Partitioning into Aqueous diC$_8$PC Solutions

The phospholipid, 1-2-dioctanyl-sn-glycero-3-phosphocholine (diC$_8$PC), belongs to the same family of short-chain phospholipids as do diC$_6$PC and diC$_7$PC. The longer tail length makes diC$_8$PC more hydrophobic and, consequently, it forms micelles much more readily than its shorter-chain counterparts, with a critical micelle concentration reported as 0.27 mM at room temperature (Tausk et al., 1974), as compared to 14.6 mM and 1.9 mM for diC$_6$PC and diC$_7$PC, respectively. In addition, diC$_8$PC phase-separates into two visually clear, immiscible phases when mixed with water at sufficiently high concentrations and low enough temperatures. Although these phases are both transparent in appearance, they are vertically distinguishable due to their density difference, with the upper layer having the consistency of water while the bottom layer is considerably more viscous.

Nostro et al. (2008) have proposed that the viscous phase consists of an inter-connected network of cylindrical micelles, based on investigations by cryogenic-transmission electron microscopy (cryo-TEM), small-angle X-ray scattering, and nuclear magnetic resonance. Figure 3.10 presents a cryo-TEM image from Nostro et al. (2008), which indicates the existence of elongated micelles. As the authors have remarked, the low contrast in the image makes it impossible to definitively state whether there is an inter-connected network of micelles, or the aggregates are simply entangled from this image alone. An illustration of this the mixture is presented in Figure 3.11.

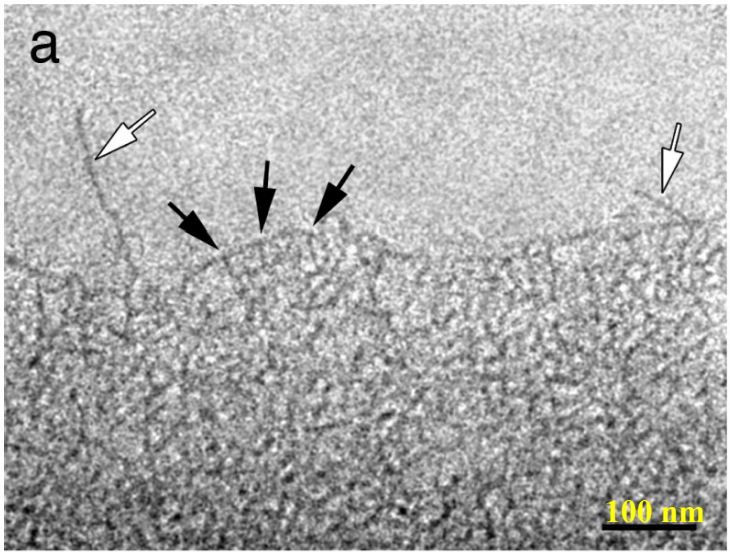

Figure 3.10. A thin sample film of diC_8PC dissolved in pure water (resistivity > 18 Ω) imaged using cryo-TEM as presented in Nostro et al. (2008). The open arrows indicate long micelles that are protruding from the network. The dark arrows indicate the presence of branch junctions [**]

Several researchers have experimentally studied the temperatures and concentrations over which the onset of micelle phase separation occurs (Carvalho et al., 1989, Tausk et al.,1974, Haung et al., 1990). The range of temperatures and concentrations that mark the phase behavior transition make

[**] Reprinted with permission from Pierandrea Lo Nostro, Sergio Murgia, Marco Lagi, Emiliano Fratini, Göran Karlsson, Mats Almgren, Maura Monduzzi, Barry W. Ninham, and Piero Baglioni. Interconnected Networks: Structural and Dynamic Characterization of Aqueous Dispersions of Dioctanoylphosphatidylcholine. *The Journal of Physical Chemistry B* **2008** *112* (40), 12625-12634. DOI: 10.1021/jp803983t. Copyright © 2008 American Chemical Society.

up what is called the "miscibility curve", which is presented in Figure 3.12. For solution compositions under the curve, the mixture will split into two phases with compositions denoted by the phase boundaries at the temperature of interest. Here, the right side of the curve represents mole fraction compositions of the lower, viscous phase.

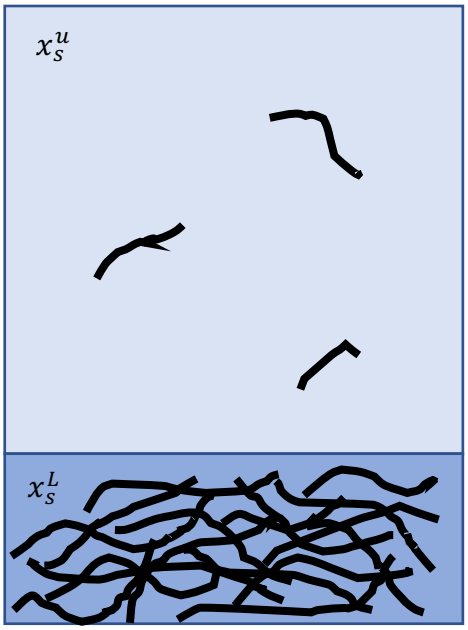

Figure 3.11. An illustration showing phase separation of diC$_8$PC. Symbols discussed in text

One defining feature of the miscibility curve is that it exhibits an upper consulate temperature, above which the viscous layer disappears. The miscibility data presented in Figure 3.12 was modeled using equations developed by Blankschtein et al. (1985) shown by curves in the figure. This group proposed a thermodynamic (mean-field type) theory that models the aggregate as long cylindrical micelles. Their model was fit to experimental data using two adjustable parameters (see Appendix B). The fit parameter, $\Delta\mu$, is related to both micelle growth and polydispersity. The second fit parameter, C, is an effective free energy of monomer-monomer interaction. The data presented in Figure 3.12

was obtained by three separate research groups, in which the miscibility curves were evaluated using Blankschtein's equation. The values of $\Delta\mu$ and C, associated with each of these data sets, is presented in Table B1 in the Appendix.

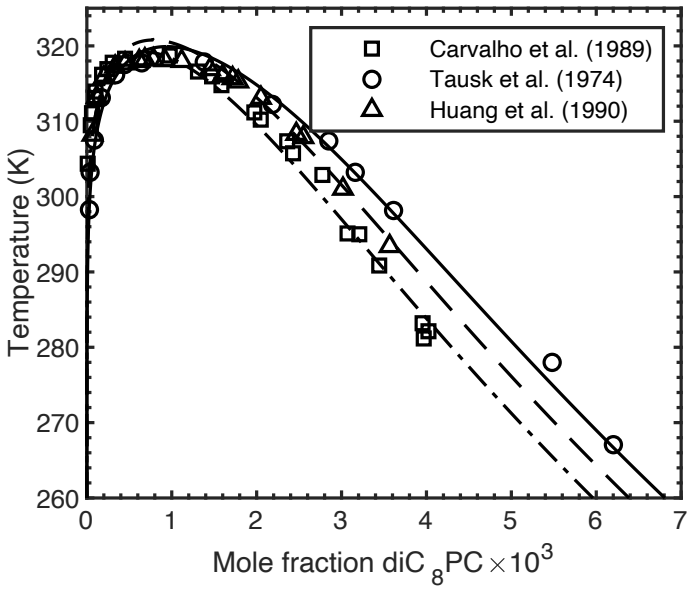

Figure 3.12. Miscibility curve for diC$_8$PC reproduced from literature sources in legend. Open symbols are experimental points. Curves are the best fit using theory developed by Blankschtein et al. (1985) (– –., –., –)

Through simple application of the lever rule, it is possible to determine the percentage of total surfactant that distributes between each of these phases for a given overall composition. Consider a mixture consisting of diC$_8$PC surfactant (s) dissolved in a bath of water (w) at conditions such that two phases form: an upper surfactant-poor phase (u) and a lower surfactant-rich phase (L). If n_{tot} is the moles of both components in the mixture, then the total moles of surfactant n_s can be written as

$$n_s = x_s n_{tot} = \ n_s^L + n_s^u = n^L x_s^L + n^u x_s^u = n^u(x_s^u - x_s^L) + n_t x_s^L. \tag{3.26}$$

Here we have used the known overall mole fraction x_s, as well as the surfactant mole fractions in each phase, denoted as x_s^u and x_s^L as appropriate. x_s^u and x_s^L are known at a given temperature from the

phase envelope in Figure 3.12. The total moles in phases u and L are expressed respectively as n^u and n^L. Solving equation (3.26) for n^u, we obtain

$$n^u = n_{tot}\frac{x_s^L - x_s}{x_s^L - x_s^u}. \tag{3.27}$$

Similarly,

$$n^L = n_{tot}\frac{x_s - x_s^u}{x_s^L - x_s^u}. \tag{3.28}$$

Finally, the moles of surfactant in each of the phases can obtained as

$$n_s^u = x_s^u n^u = x_s^u n_{tot}\frac{x_s^L - x_s}{x_s^L - x_s^u}; \tag{3.29}$$

and

$$n_s^L = x_s^u n^L = x_s^L n_{tot}\frac{x_s - x_s^u}{x_s^L - x_s^u}. \tag{3.30}$$

Then the fraction of total surfactant in the upper phase, designated as $f = n_s^u/n_s$, may be determined:

$$f = \frac{n_s^u}{x_s n_{tot}} = \frac{x_s^u}{x_s}\frac{x_s^L - x_s}{x_s^L - x_s^u}. \tag{3.31}$$

Likewise, the fraction of surfactant present in the lower phase is

$$1 - f = \frac{x_s^L}{x_s}\frac{x_s - x_s^u}{x_s^L - x_s^u}. \tag{3.32}$$

The existence of a second micellar phase within the aqueous solution could mean that at least two micelle-water partition coefficients would be needed to fully characterize limonene partitioning in the mixture. Attempts were made to measure partitioning of limonene into the single-phase solutions that form at diC_8PC concentrations below that required for the formation of a second, surfactant-rich phase. Unfortunately, in these preliminary measurements the effects of solubilization, at such low surfactant concentrations, could not be easily distinguished from the inherent scatter in

GC/MS peak area data. However, inspection of the phase diagram and Equation (3.32), shows us that increasing diC$_8$PC's concentration in water even slightly past the left phase boundary results in a vast increase in the fraction of surfactant found in the lower phase. Figure 3.13 shows the fraction of total surfactant in the lower phase $(1-f)$ as a function of the aqueous solution concentration at 25°C. These values were obtained by fitting phase boundary data phase from Huang et al. (1990) with equations (B.1–B.2) in Appendix B. The latter equations were obtained from the micellization theory of Blankschtein et al. (1985). The values of x_s^L and x_s^u as obtained from the best fit to the equations at 298K are given in Table 3.14. Values for the concentrations $c_s^L = n_S^L/V_\ell$ and $c_s^u = n_S^u/V_\ell$, where V_ℓ is the liquid phase volume are also given in the table. It is apparent that differences in the phase diagram results obtained by Carvalho et al. (1989) and Tausk et al. (1974) will yield somewhat different fit parameters and hence shifted predictions for $(1-f)$ versus aqueous diC$_8$PC mole fraction.

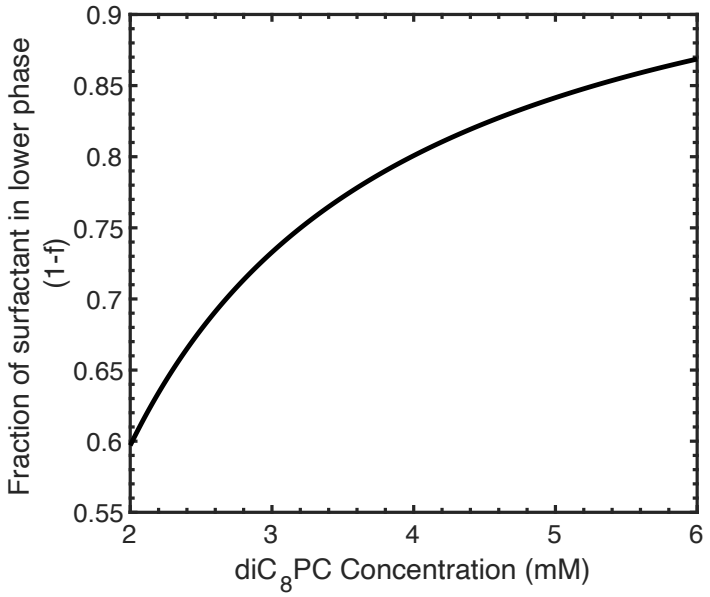

Figure 3.13. The percentage of total surfactant in the lower phase, 1-f, as a function of total concentration of prepared diC$_8$PC at 298K

Table 3.14. Surfactant mole fractions at 298K as found via Equations B.1–B.2, with data from Huang et al. (1990)

Mole fractions		Concentrations (mM)	
x_s^u	1.67×10^{-5}	c_s^u	0.93
x_s^L	3.14×10^{-3}	c_s^L	174

By choosing a concentration of diC_8PC in the two-phase region that is sufficiently beyond x_s^u, we can obtain useful information on limonene partitioning into diC_8PC micelles. At an overall concentration of c_s=4mM, the majority of the surfactant is found in the rich lower phase. Small-angle neutron scattering measurements conducted at 55°C (i.e., above the upper consulate temperature) were consistent with very long, thin cylindrical micelles (Eastoe et al., 1998). Furthermore, theoretical and experimental studies suggest that long flexible structures form at concentrations near the cmc and rapidly grow with an increase in concentration (Blankschtein et al., 1985; Tausk et al., 1974a), even for concentrations below c_s^u. Thus, the minority micelles found in the dilute upper phase are structurally very similar to those in the lower phase. We thus assume that the partitioning of solute into micelles found in either of the phases would be quantitatively similar, with any differences averaged to heavily favor the surfactant-rich phase at 4mM. This assumption would be better justified at even higher experimental values x_s, since the amount of total surfactant would further dominate the lower phase. However, practical considerations associated with material costs and time constraints meant we could not explore this limit further. We considered allowing the 4mM solution to phase separate, and subsequently extracting the viscous layer (via separatory funnel as an example) in order to conduct our partitioning studies. However, the amount of viscous layer that one can separate (per volume basis) was too small to be useful for these experiments. We also note we do not account for the possibility of changes in micellar distribution and phase behavior due to the addition of limonene.

We collected measurements at 25(±0.5)°C as described in §3.3.2, using 4 mM of diC$_8$PC mixtures, corresponding to an aqueous mole fraction of 7.2×10^{-5}. Preparation of these solutions resulted in a turbid, visually opaque solution upon mixing, which suggested that the solution was within the two-phase envelope as predicted by the phase diagram. Figure 3.14(a) presents measurements made at 25(±0.5)°C with varying amounts of total limonene added. Note that, although some variability in GC/MS peak area data was observed between sets in Figure 3.14(a), normalized data was highly reproducible. That is, normalizing the data by each replicate set's apparent saturated peak yield reproducible results for $c_{i,v}/c_{i,v}^{sat}$ shown in Figure 3.15(b). The standard deviations for these values were small (Table 3.15). Peak areas measured from prepared standards containing pure limonene alone or water saturated limonene at 40°C, on the other hand, were less reproducible, as indicated by the large variances in most sets (Table 3.16). While it is uncertain as to why these measurements were specifically affected, possible explanations include sample sensitivity to either light or temperature thus impacting partitioning into the headspace.

Table 3.15. Peak areas measured to determine the saturated vapor concentrations of limonene at 25(±0.5)°C

Set[a]	(Apparent Saturated Peak Area)×10^6	(Saturated Water Solution Peak Area)×10^6	(Pure Limonene Peak Area)×10^6
1	3.253±0.166	3.3050±0.0921	3.075±0.309
2	3.0742±0.0530	2.946±0.0391	2.835±0.195
3	2.8514±0.0881	2.887±0.0822	2.7635±0.0689

[a]For each replicate set, at least three measurements were made with error given as 1 S.D.

Table 3.16. Data measured to determine the saturated vapor concentrations of limonene at 40(±0.5)°C

Set[a]	(Apparent Saturated Peak Area)×10^6	(Saturated Water Solution Peak Area)×10^6	(Pure Limonene Peak Area)×10^6
1	5.113±0.185	7.69±2.97	8.71±3.61
2	3.559±0.200	7.92±5.39	5.18±1.94
3	2.5334±0.0369	2.887±0.0822	11.5±7.36

[a]For each replicate set, at least three measurements were made with error given as 1 S.D.

Figure 3.15 shows measurements made at 40(±0.5)°C above 4 mM mixtures. At this temperature, the diC_8PC looked visually clear, both prior to and after limonene was added, indicating the presence of a single phase. The observed single phase is consistent with the phase diagram given Figure 3.12. Figure 3.15(b) shows the data normalized by the average saturated peak area values. Table 3.16 contains the averaged pure and saturated results per replicate set and is analogous to Table 3.15.

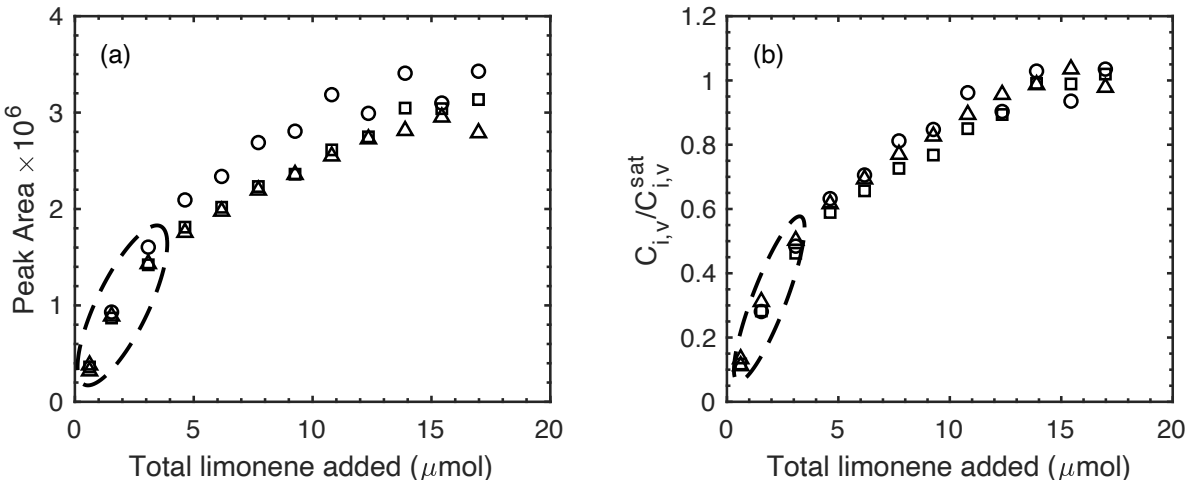

Figure 3.14. Replicate sets (○, □, Δ) of solubilization isotherms for limonene added to11.70±0.2mL with 4mM diC_8PC solution at 25±0.5°C. In (a), raw measurements of peak areas acquired by GC/MS are plotted as replicate sets. In (b), values on the left axis were normalized by the apparent saturated peak areas. Dashed ovals identify mixtures that were visibly turbid

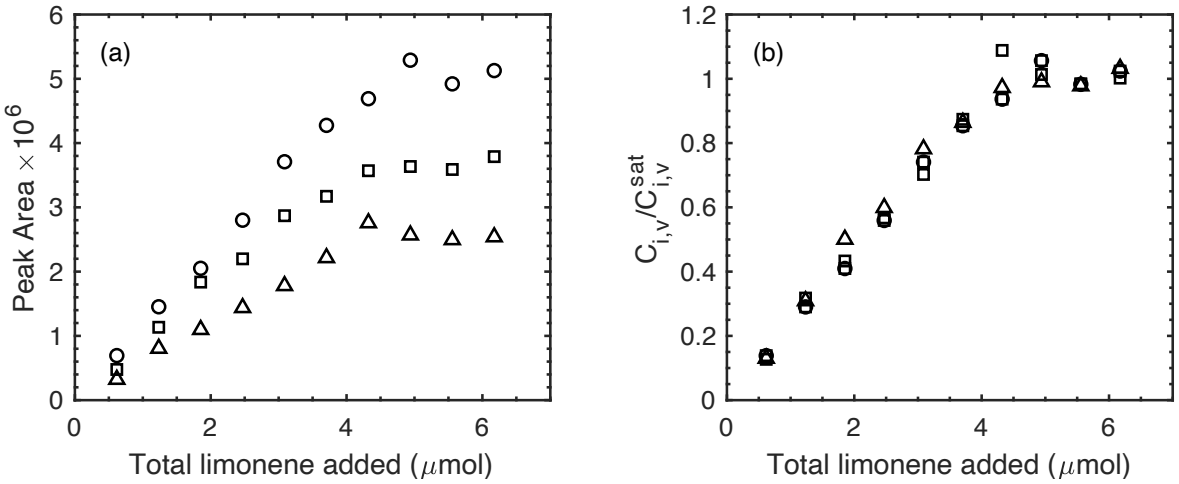

Figure 3.15. Replicate sets (○, □, Δ) of solubilization isotherms for limonene added to 11.70±0.2mL vials with 4mM diC$_8$PC solution at 40±0.5˚C, presented in parts (a) and (b) analogously to plots in Figure 3.14

The solubilization isotherms presented in Figure 3.14 and Figure 3.15 were used to find the best fit K_{mw} (K_{mw}^{II}) shown in Figure 3.16, similar to the procedure followed with diC$_6$PC and diC$_7$PC. This was done by fitting the data to Equation 3.18, where now $c_{s,m}$ represents the total moles of micellized diC$_8$PC divided by the total volume of liquid in the mixture. $c_{s,m}$ was obtained by subtracting the moles of micellized diC$_8$PC monomer, as determined from the published cmc of 0.27mM (Tausk and Overbeek, 1974). Under this approach, we have assumed that the molecular limonene dissolved in water forms an ideal-dilute solution.

Equation 3.18 fits the data well, showing trends which are qualitatively similar to diC$_6$PC and diC$_7$PC, as temperature is increased: the vapor concentration dependence on limonene is quadratic at ambient temperatures and linear at 40˚C. Table 3.17 summarizes our experimental results for K_{mw} and the maximum mole fractions $x_{i,m}^{sat}$ obtained from the solubilization isotherms at these higher limonene concentrations. At ambient temperatures, both $x_{i,m}^{sat}$ and K_{mw}^{II} appear to increase with surfactant chain length in the diC$_n$PC series, with the largest increase occurring between diC$_6$PC and diC$_7$PC. A similarly substantial effect of chain length was observed at 40˚C for diC$_6$PC and diC$_7$PC,

but no increase in $x_{i,m}^{sat}$ nor in K_{mw}^{II} (M^{-1}) was observed between diC_7PC and diC_6PC at 40˚C. At the higher temperatures these values were significantly reduced for all three phospholipids, compared to their values at room temperature.

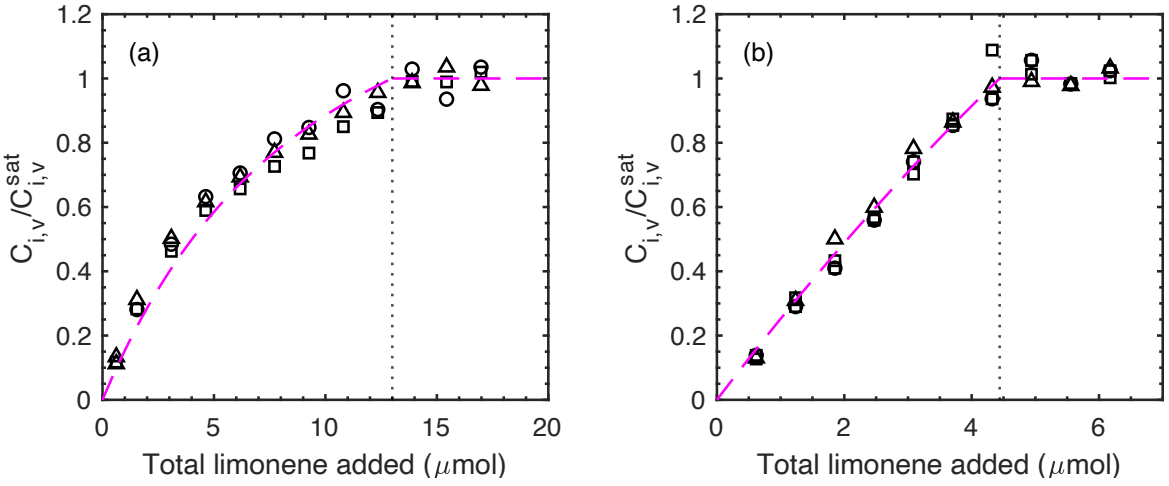

Figure 3.16. Normalized solubilization isotherms from data given in Figure 3.15. Purple line corresponds to Equation (3.18), with the best fit value for K_{mw}^{II}

Table 3.17. Maximum mole fraction of limonene in micelles, $x_{i,m}^{sat}$, and best fit K_{mw}^{II} for all phospholipids and temperatures studied

	diC_6PC		diC_7PC		diC_8PC	
	$x_{i,m}^{sat}$	$K_{mw}^{II}\times10^3$	$x_{i,m}^{sat}$	$K_{mw}^{II}\times10^3$	$x_{i,m}^{sat}$	$K_{mw}^{II}\times10^3$
(23±1)˚C	0.25	2.360±0.027	0.51	5.108±0.048	0.60	5.96±0.10[a]
(40±0.5)˚C	0.13	1.965±0.074	0.25	3.48±0.12	0.25	3.53±0.068

[a] Measured at 25(±0.5)˚C

It was observed that after mixing 4mM diC_8PC with water at room temperature, solutions containing amounts comparable to or greater than ~4.65 μmol looked clear. Mixing was performed at 350 RPM using an agitator attached to Gerstel MPS 2 autosampler for 3 hours, and samples were allowed to equilibrate for at least an additional 3 hours before samples were measured as described in the methods section of this chapter. Solutions at lower limonene concentration which remained turbid

are indicated by the data symbols inside of the dashed oval depicted in Figure 3.14; these mixtures were calculated to have total liquid concentrations of 1.9 mM or less. Thus, remarkably, these results indicate that the addition of limonene lowered the miscibility temperature (i.e. cloud point) below which phase separation occurs. General suppression of the upper consulate temperature in diC_8PC has been reported to occur by addition of other additives, such as salt (Huang et al., 1990) urea (Carvalho et al., 1989), and tributyrin (Ramon A Burns and Roberts, 1981b). In some cases, having enough additive could lower the upper consulate temperature to well below room temperature. For example, Carvalho et al. (1989) found that the upper consulate temperature could be lowered from ~47˚C to ~25˚C through addition of urea at a mole fraction of 0.0089 in solution. By approximating the density of solution as 1 g/mL, then this would equate to a liquid concentration of ~0.5M. These authors discounted partitioning of urea between micelles and water as the explanation for the observed lowering the phase boundary, as measurements showed that concentrations of urea in water did not change upon phase separation. Instead, they observed that as the upper consulate temperature decreased, and the dielectric constant increased linearly with an increase in aqueous mole fraction of urea. The ability of dissolved urea to weaken hydrophobic interactions between diC_8PC tails was also noted. This led the authors to propose that decrease in the phase boundary temperature was a result of weakening of the interaction potential between lipid molecules by increased dielectric screening between them, combined with reduced micelle growth due to weakened hydrophobic effects.

In contrast to urea, limonene does not appreciably dissolve in water. As can be shown by the mass balance, the amount of solute that is solubilized with micelles is similar in quantity to surfactant in micelles ($x_{i,m} > 0.3$). At these higher solute loadings, a significant change in micellar size distribution is likely, as was observed via DLS by Roberts et al. (1983) in aqueous tributyrin/diC_7PC solutions. In those studies, there appeared to be a substantial decrease in both hydrodynamic "size" and polydispersity of the micelles in moving from a solute-free (aqueous) diC_7PC solution to

tributyrin-saturated aqueous diC_7PC solution. Since both diC_7PC and diC_8PC form rod-like micelles and share the same head group, it is plausible that diC_8PC micelles would also change their shape to accommodate hydrophobic solute compounds. We thus postulate that our loaded micelles are probably smaller in size at these high limonene amounts, and this may enhance the miscibility at a given temperature.

Notably, cloud point depression through addition of limonene is not necessarily unique to our system. Similar findings have been observed in aqueous solutions of $C_{16}POE_{10}$ (Tokuoka et al., 1992). In addition, changes in aqueous nonionc solutions of $C_{12}E_6$ and n-dodecane have been studied using static and dynamic light scattering techniques (Einaga et al., 2004). These studies found that these rod-like micelles collapse into smaller spherical ones by incorporation of oil solute. It is possible that these short-chain phospholipids exhibit a similar mechanism with limonene. Further studies are needed to determine why we observe cloud point depression in our solute-containing system.

3.4 Summary

Micelle-water partition coefficients for limonene distributing within aqueous diC_nPC$|_{n=6,7,8}$ solutions at temperatures ranging between 15–40˚C were developed using headspace SPME. In doing so, we have shown SPME to be an effective and convenient tool for probing local aroma distributions. At low limonene concentrations, limonene was more readily solubilized into diC_7PC as compared with diC_6PC at all temperatures studied. However, the difference between the two PCs' solubilization potential diminished with increased temperature. At higher limonene concentrations of limonene, the larger mole fraction appeared to substantially influence the micelle energetics at ambient temperatures, but much less so at 40˚C. There also did not appear to be meaningful differences in micelle-water partition coefficients between diC_7PC and diC_8PC. Lastly, we find that limonene had comparable affinity for these PC micelles as more conventional surfactants. These observations are notable

considering their atypical two-tailed structure, especially in light of their relation to natural, long-chain phospholipids.

3.5 Nomenclature

diC$_6$PC 1,2 dihexanoyl-*sn*-glycero-3-phosphocholine

diC$_7$PC 1,2 diheptanoyl-*sn*-glycero-3-phosphocholine

diC$_8$PC 1,2 octannoyl-*sn*-glycero-3-phosphocholine

V_v ..... volume of vapor

V_w ..... volume of water

V_t ..... total volume

$c_{i,v}$ ..... concentration of solute in vapor

$c_{i,w}$ ..... concentration of solute in water

K_{vw} ..... vapor-water partition coefficient; $c_{i,v}/c_{i,w}$

$c_{s,m}$ ..... concentration of surfactant in micelles

cmc ..... critical micelle concentration

$\bar{v}_w$ ..... molar volume of water

$x_{i,m}$ ..... mole fraction of solute in micelles

K_{mw} ..... micelle-water partition coefficient; $x_{i,m}/c_{i,w}$

$n_{i,t}$ ..... total moles of solute

$n_{i,v}$ ..... moles of solute in vapor

$n_{i,w}$ ..... moles of solute in water

$x_{i,m}^{sat}$ ..... mole fraction of solute in micelles at saturation

$c_{i,v}^{sat}$ ..... concentration of solute in vapor at saturation

n_{max} ..... maximum moles of solute that can be dissolved in solution

$n_{i,m}^{sat}$ ..... moles of solute in micelles at saturation

$n_{i,v}^{sat}$ ..... moles of solute in vapor at saturation

K_{mw}^{I} ..... micelle-water partition coefficient obtained at low limonene concentrations

K_{mw}^{II} ..... micelle-water partition coefficient obtained over entire solubility limit of limonene

$\hat{c}_i$ ..... $c_{i,v}/c_{i,v}^{sat}$

$\hat{n}_{i,t}$ ..... $n_{i,t}/c_{i,w}V_w$

$\bar{v}_w$ ..... molar volume of water

$\hat{V}$ ..... dimensionless volume; $1 + K_{vw}V_v/V_w$

A ..... $x_{i,m}^{sat}\hat{V}$

B ..... $K_{mw}c_{s,m} + \hat{V} + \hat{n}_{i,t}x_{i,m}^{sat}$

C ..... $\hat{n}_{i,t}$

a ..... thermodynamic term capturing non-ideal changes in K_{mw}

$\breve{A}$ ..... $x_{i,m}^{sat,I}(a+1)\hat{V}$

$\breve{B}$ ..... $K_{mw}^{I}c_{s,m} + \hat{V} + \hat{n}_{i,t}x_{i,m}^{sat,I}(a+1)$

$\breve{C}$ ..... $\hat{n}_{i,total}$.

n_s ..... moles of surfactant in solution

x_s ..... mole fraction of surfactant in solution

n_{tot} ..... moles of surfactant and water in solution

n_s^L ..... moles of surfactant in lower micelle phase

n_s^U ..... moles of surfactant in upper micelle phase

x_s^u ..... mole fraction of surfactant in upper micelle phase

x_s^L ..... mole fraction of surfactant in lower

f ..... n_s^U/n_S

V_ℓ ..... liquid phase volume

c_s^u ..... concentration of surfactant in upper phase

c_s^L ..... concentration of surfactant in lower phase

$c_{i,v}^o$ ..... vapor concentration of solute i in the absence of surfactant

Chapter 4

Partitioning Behavior of Hydrophobic Compounds into Aqueous $C_{12}E_{10}$ Surfactant Solutions

4.1 Introduction

Nonionic surfactants are of importance to numerous processes such as in the manufacturing and formulation of detergents, cosmetics, pharmaceuticals, and pesticides. In the last case, surfactants not only enhance solubility and stability of pesticides in agricultural spray formulations, but may also improve wettability of spray droplets to the outer waxy-like surfaces of plant leaves (Song et al., 2019). This is particularly beneficial since the hydrophobicity of leaves contributes to spray droplets' poor adhesion to the plant's surface upon use, which contributes to pollution of soil, surface water, and ground water (Song et al., 2019). In pharmaceutical applications, nonionic surfactants aid in the bioavailability of drugs, whereby they can improve aspects of drug absorption. For example, polyethylene oxide surfactants have been used effectively as promising topical ocular drug delivery systems (Jiao, 2008). Membrane solubilization of ocular epithelial cells' phospholipid bilayer can contribute to increased permeability of drugs to the cell interior (Järvinen et al., 1995; Jiao, 2008).

Most studies that model solubilization in micellar solutions limit their analysis to some form of the pseudo-phase model as described above in Chapter 1. This is, in part, because only a few experimental methods allow the necessary measurements to be taken in situ—without need for physically separating dissolved components. However, connecting these studies to a classical thermodynamic framework would aid in providing a fundamental understanding to solubilization

mechanics. Such approaches provide ample amounts of data that can be applied to the development of an *a priori* predictive model.

This chapter examines solubilization research of several poorly water-soluble compounds in aqueous solutions of decaethylene glycol monododecyl ether ($C_{12}E_{10}$) using HS-SPME. In §4.3.1 and §4.3.2, micelle-water partition coefficients and extent of solubilization are first evaluated. In §4.3.4 and §4.3.5, relative vapor concentration measurements are converted into chemical potentials. A new thermodynamic treatment is developed, in which the chemical potential of solute is related to the overall molar solubilization ratio. In development of this new approach, we also find a complementary method for evaluating the enthalpy of dissolution that was discussed above in Chapter 2.

4.2 Materials and Methods

Decaethylene glycol monododecyl ether ($C_{12}E_{10}$), 1-octanol (99%), n-decane (99%), and d-limonene (97%) were purchased from Sigma-Aldrich (St. Louis, MO) and used without further purification. Deionized water (18 Ω) was obtained from water filtration system (MilliQ^{TM}) installed in the laboratory (Millipore, Bedford, MA).

4.2.1 SPME-GC/MS

Peak area measurements were acquired via headspace solid-phase microextraction (HS-SPME) techniques paired with gas-chromatography/mass-spectrometry (GC/MS). Details of the instrument are given in Chapter 3. An 85μm polyacrylate fiber (Resetek, PA) was used for all measurements. Upon purchase, the SPME fiber was pre-conditioned in the GC inlet at 280°C for 30 minutes. Extraction and desorption times were selected as 1 minute and 10 minutes, respectively. Prior to each day's first experimental run, the SPME fiber was conditioned in the GC inlet at 240°C for 15 minutes. Programming of the GC/MS followed methods identical to those given in Chapter 2. For clarity, these GC/MS parameters are presented in Table 4.1 below.

Table 4.1. GC/MS parameters for all studied solutes

	Solutes		
GC/MS Parameter	limonene	1-octanol	n-decane
Inlet Mode Split ratio	50:1	100:1	100:1
Initial Temperature (˚C)	40	40	40
Rate 1 (˚C/min)	5	5	5
Temperature 1 (˚C)	75	95	75
Rate 2 (˚C/min)	40	40	40
Final Temperature	240	240	240
SIM ion (m/z)[a]	68	56	57
GC/MS Interface Temperature (˚C)	260	260	260
Column Flow Rate (mL/min)	1	1	1

[a]Most abundant ion fragment

4.2.2 Sample Preparation

Stock solutions of $C_{12}E_{10}$ were prepared in DI water at either 10mM or 200mM final concentrations via a volumetric flask. From the stock, samples were diluted directly in either 11.7(±0.2) mL or 21.7(±0.2) mL SPME vials to their final surfactant concentration. Afterwards, aliquots of solute were added via micro-syringe before the vials were subsequently capped using a crimping tool and the quadruple barrier setup as discussed previously (Chapter 2).

For the experiments described in §4.3.1, solute was added to the HS-SPME vials containing $C_{12}E_{10}$ solution to create a series of solute concentrations up to and beyond that for which the system was saturated with solute. Volumetric ranges for the solutes added to 5 or 2 mL of water in this work are given in Table 4.2. Solubilization isotherms in §4.3.5 were made by varying $C_{12}E_{10}$ concentrations. These were prepared by dilution of a 300mM $C_{12}E_{10}$ stock solution. For selected sample sets measured

within a day, triplicate sample vials containing 2 mL (21.7mL vials) or 1 mL (11.7 mL vials) of pure solute were included in the set. All measurements were made on samples equilibrated at 25°C.

4.2.3 Statistics

Weight average values and their respective errors were calculated using Equations (2.1) and (2.2) given in Chapter 2. Non-linear least squares regression was performed using fitting methods as described in Chapter 3.

4.3 Results and Discussion

4.3.1 Partitioning of Hydrophobic Solutes in Aqueous $C_{12}E_{10}$ Solutions

GC-SPME headspace peak area measurements of various solutes were made above aqueous, solute-containing micellar solutions of $C_{12}E_{10}$. For each micellar system studied, the surfactant concentration was held fixed while the solute concentration was varied. In doing so, the entire set of headspace peak area measurements for each solute at a constant temperature 25°C make up the 'solubilization isotherm'. Figure 4.1(a–c) show raw headspace measurements for aqueous 200mM $C_{12}E_{10}$ solutions containing additions of limonene, octanol, and decane, respectively. In Figure 4.1(d) is presented the raw headspace measurements for a 10mM $C_{12}E_{10}$ solution containing additions of limonene. As with our phosphatidylcholine/limonene studies (§3.3.3), increasing solute generally led to higher peak area peak measurements until a threshold amount of solute was reached, beyond which the peak area values plateaued. Amounts of solute beyond this threshold limit likely saturate the micellar solution, so that an excess bulk solute phase would form. Correspondingly, there was a plateau of measured peak area with added solute above the threshold concentration. Figure 4.2(a–d) presents normalized data from Figure 4.1, where peak areas were normalized by the average values in the plateau region, within which the solution was apparently saturated $\left(c_{i,v}/c_{i,v}^{sat}\right)$. The data points in the plateau region were identified by visual inspection of the peak area data in Figure 4.1.

Table 4.2. Volume range of total solute added

V_w (mL)	V_t (mL)	$C_{12}E_{10}$ (mM)	Decane (μL)	Limonene (μL)	Octanol (μL)
5	21.7	200	2–120	2–70	2–240
2	11.7	10	—	0.25–3.5	—

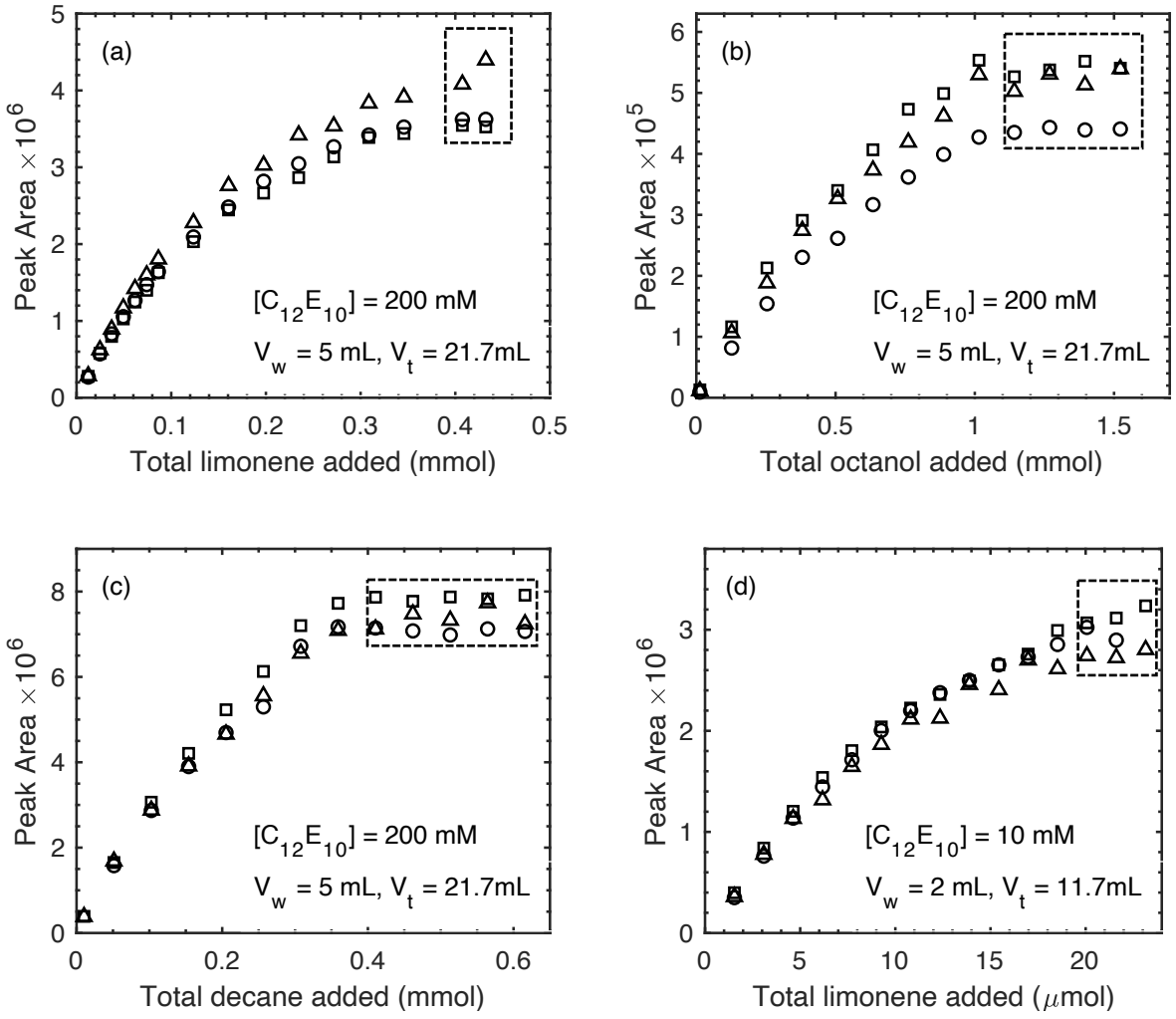

Figure 4.1. Triplicate raw headspace peak area measurements (○, □, Δ) of (a) limonene, (b) octanol, and (c) decane added into 200mM aqueous solutions of $C_{12}E_{10}$ at (25±0.5)°C. In (d) raw headspace measurements of limonene were made above a 10mM aqueous solution of $C_{12}E_{10}$ at (25±0.5)°C. V_w and V_t represent liquid volume and total vial volume, respectively. Data averaged to yield peak area results for the plateau region shown in dashed box.

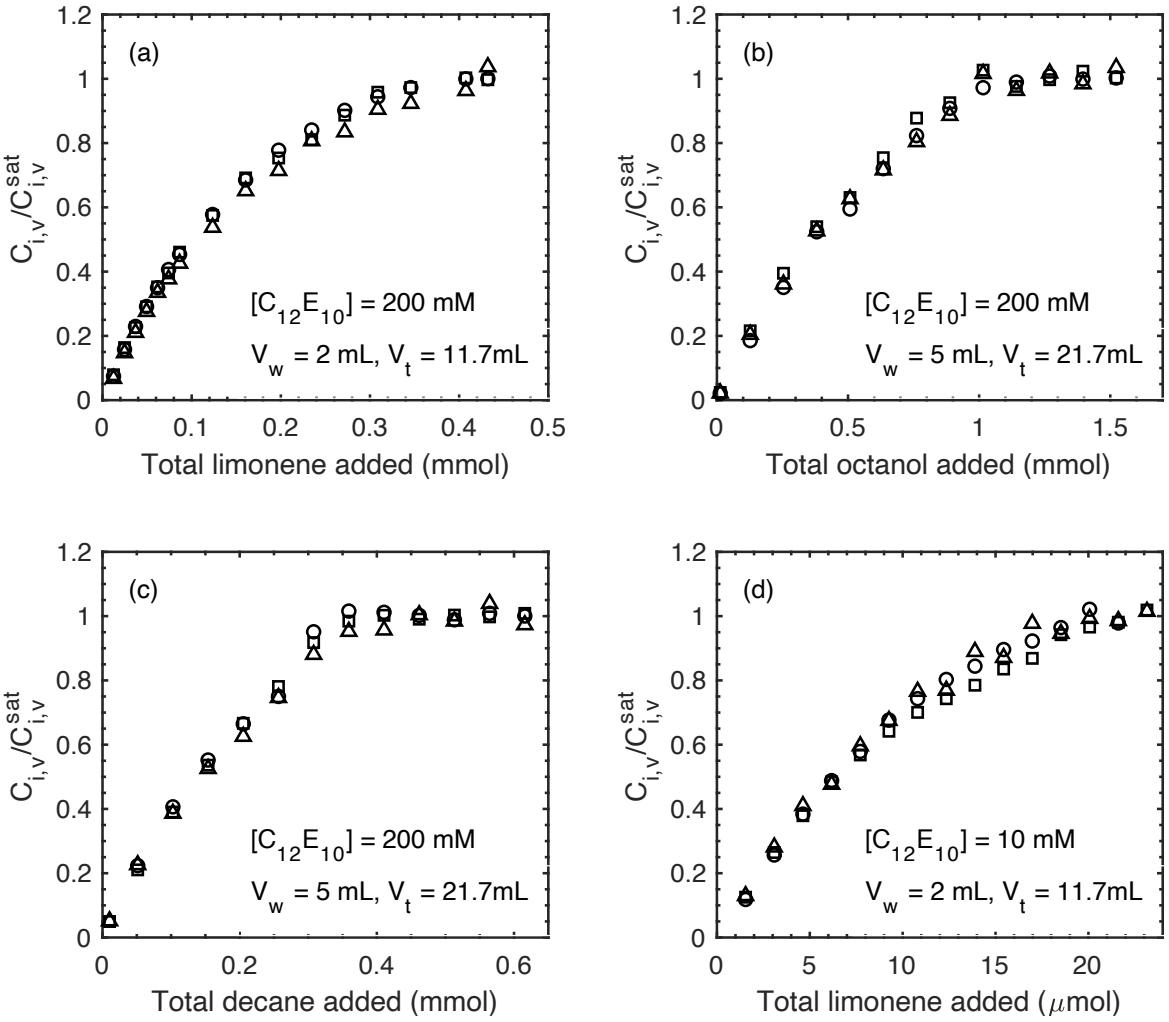

Figure 4.2. Triplicate measurements of solute (○, □, Δ) in aqueous solutions of $C_{12}E_{10}$ as given in Figure 4.1, normalized by the average of saturated peak areas of each replicate set. V_w and V_t represent liquid volume and total vial volume, respectively.

Table 4.3 serves to complement Figure 4.2, by providing a comparison between the averaged peak area values for pure solute liquid and comparable values for the $C_{12}E_{10}$ solute-containing mixtures in the plateau region (saturated solutions). The apparent saturated peak area was uniformly smaller than the pure peak area measurements, most likely due to the saturation of the bulk excess solute phase by water, which lowers the solute chemical potential. The difference between pure solute peak area and solute saturated peak area was largest (~27%) for the octanol/$C_{12}E_{10}$ system, among studied solutes. In addition, this difference was more substantial than that observed from independent measurements for saturated octanol in water alone, without surfactant (Table 2.5, §2.3.5). The latter values were about 11% smaller on average than those for pure octanol. We postulate that $C_{12}E_{10}$ in the surfactant containing mixtures may form reverse micelles in octanol, thereby solubilizing additional water content into the excess bulk octanol phase and lowering the octanol vapor pressure. For saturated limonene in either 10mM or 200mM $C_{12}E_{10}$, averaged peak areas were approximately 10% smaller than that above pure limonene. This difference is similar to that between saturated solutions of limonene and water (Table 2.5, §2.3.5). Lastly, the 200mM $C_{12}E_{10}$/decane solutions saturated peak areas were about 5% smaller than the pure decane. In Figure 4.2, the data is normalized by the averaged peak areas in the plateau region, defined as the region where measurements are approximately constant with added solute. This approach tended to yield lower error, as represented by the sample standard deviation, than measurements normalized by values obtained from pure solute. The resulting normalized values should represent solute vapor concentrations relative to those above saturated micellar solutions.

Figure 4.3 presents the solubilization isotherm data for $c_{i,v}/c_{i,v}^{sat}$ from Figure 4.2, together with fits of Equation (3.18a) to determine K_{mw}. Each best fit to the $c_{i,v}/c_{i,v}^{sat}$ data, represented as a purple dashed line, was obtained using the mole balance on solute (Equation (3.4)) and treating K_{mw} as a fitted constant.

Table 4.3. Comparison of headspace peak area measurements above pure octanol or octanol in 200mM $C_{12}E_{10}$ in the plateau region as presented in each data set as given in Figure 4.2.

			Peak Area($\times 10^6$) [a]	
[$C_{12}E_{10}$]	Solute	Set	Pure	Saturated
200mM	Octanol	1	0.617±0.018 (n=3)	0.4396±0.0034 (n=4)
		2	0.760±0.025 (n=3)	0.539±0.011 (n=4)
		3	0.6814±0.0022 (n=3)	0.521±0.017 (n=4)
	Limonene	1	3.996±0.086 (n=3)	3.6230±0.0019 (n=2)
		2	4.02±0.37 (n=3)	3.536±0.014 (n=2)
		3	4.76±0.28 (n=3)	4.24±0.22 (n=2)
	Decane	1	7.65±0.12 (n=3)	7.21±0.33 (n=5)
		2	8.15±0.13 (n=3)	7.845±0.061 (n=5)
		3	7.84±0.47 (n=3)	7.44±0.22 (n=5)
10mM	Limonene	1	3.365±0.054 (n=3)	2.960±0.089 (n=3)
		2	3.412±0.079 (n=3)	3.176±0.085 (n=3)
		3	3.06±0.31 (n=3)	2.762±0.057 (n=3)

[a]Error represents 1 standard deviation of the measurements.

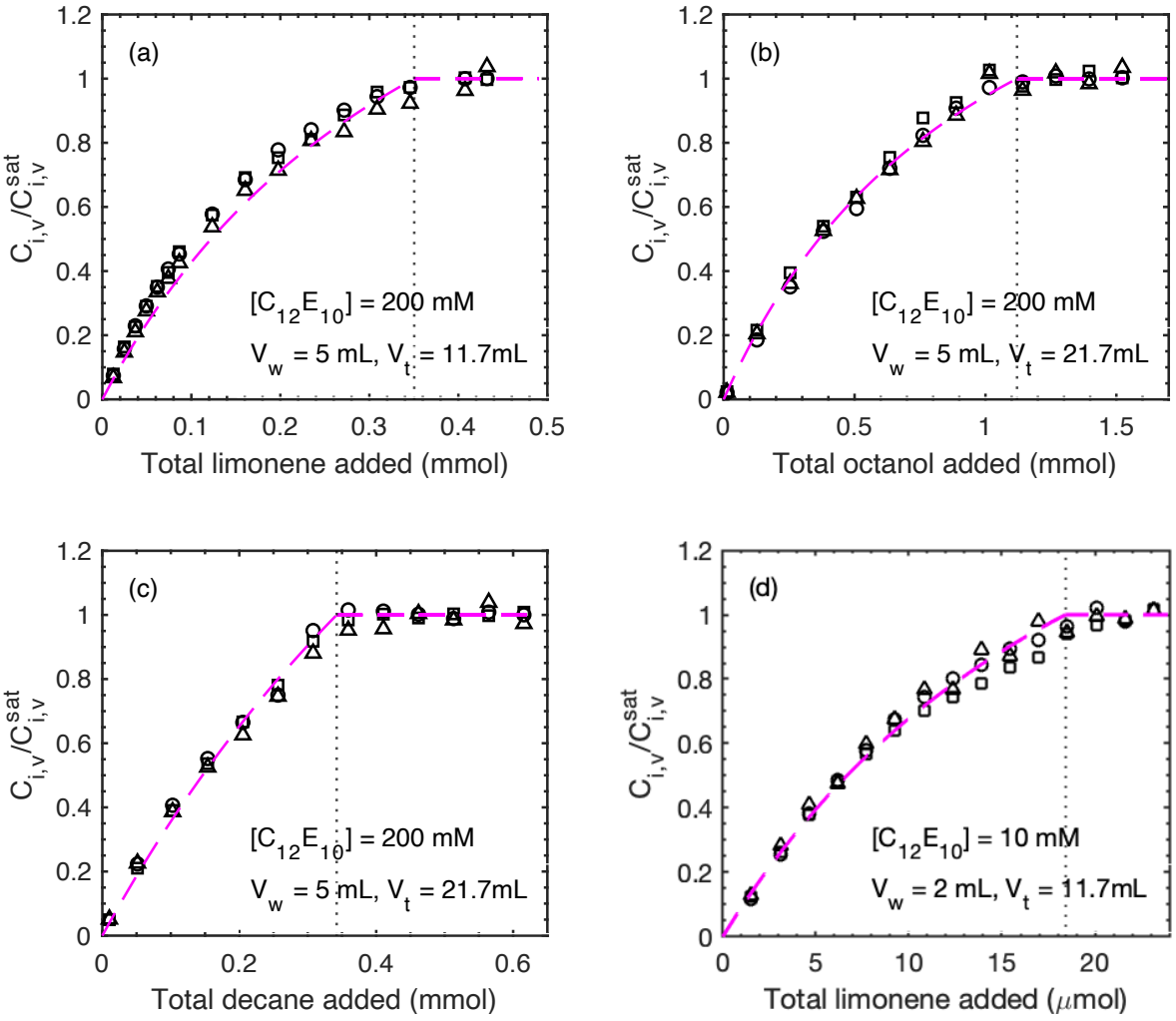

Figure 4.3. Triplicate measurements (○, □, Δ) of solute in aqueous solutions of $C_{12}E_{10}$ as given in Figure 4.2, together with solubilization isotherm fits (purple dashed line). Vertical dotted indicates breakpoint in which the solution becomes saturated with solute.

An important difference between these studies and those presented in Chapter 3 are the total quantities of surfactant concentrations studied. At 200mM $C_{12}E_{10}$, much larger amounts of solute can be solubilized in solution (see Table 4.2) than previously obtained with the diC_nPC systems with lower concentrations. In turn, the volume of vapor is expected to slightly decrease (~2%) with addition of solute. To check if this would substantially change our partition coefficient calculations, changes in vapor volume were recalculated by assuming solution volume additivity with solute. In all cases, changes in the partition fit partition coefficient were ≤ 5% and were deemed negligible. Table 4.4

gives the weighted averages of the fitted K_{mw} values for each of the three sets, denoted as K_{mw}^{II} as in Chapter 3. Values for K_{mw}^{II} were used to determine the calculated amount of solute n_{max} added at the solubility limit, where $c_{i,v} = c_{i,v}^{sat}$ (Equation 3.18). Solute phase separation will occur for amounts larger than n_{max}.

Table 4.4. Weight averaged partition coefficients and maximum amounts of solute before saturation for the studied 200mM $C_{12}E_{10}$ systems

$[C_{12}E_{10}]$ (mM)	Solute	$K_{mw}^{II} \times 10^3$ (M^{-1})	n_{max} (mmol)	R^2_{adj}	$\langle K_{mw}^{II} \rangle \times 10^3$ (M^{-1})	$\langle n_{max} \rangle$ (mmol)
200	Octanol	0.1499±0.0017	1.121± 0.026	0.996	0.1471±0.0016	1.077± 0.023
		0.1438±0.0013	1.030± 0.018	0.998		
		0.1486±0.0018	1.101± 0.028	0.995		
	Decane	(518.7±9.9)	0.3423± 0.0087	0.985	(547.5±9.9)	0.3580± 0.0089
		(543±11)	0.364± 0.010	0.985		
		(547.5±9.1)	0.3681± 0.0083	0.992		
	Limonene	(4.351±0.081)	0.315± 0.010	0.981	(4.454±0.081)	0.327± 0.011
		(4.383±0.082)	0.319± 0.011	0.980		
		(4.614±0.081)	0.350± 0.012	0.983		
10	Limonene	(4.565±0.048)	0.01842± 0.00033	0.993	(4.693±0.073)	0.01860 ± 0.00040
		(4.844±0.053)	0.02044± 0.00041	0.990		
		(4.566±0.070)	0.01841± 0.00048	0.982		

From these results, we find that K_{mw}^{II} is largest for the least soluble compound, decane, and is followed by limonene and octanol. The decane partition coefficient is more than 100× larger than

that for limonene, and 3700× larger than for octanol. There did not appear to be a statistical difference ($p > 0.05$) in K_{mw}^{II} for limonene between the 200mM $C_{12}E_{10}$ and the 10mM $C_{12}E_{10}$ system.

4.3.2 Literature K_{mw} Values for Aqueous Nonionic Surfactant Solutions Containing Solute

Table 4.5 provides micelle-water partition coefficients (K_{mw}) of our studied solutes as taken from various surfactants found within the literature. Also included are the partition coeffficients of short-chain phospholipids given in Chapter 3. The cited methods shown in this table indicate that turbity approaches, in which measurements are made at the saturation limit of solute within a micellar solution, are a common experimental technique for obtaining K_{mw}. K_{mw} was calculated directly from the data sets available from the given sources in order to make their findings directly comparable with our own. To do so, $x_{i,m}^{sat}$ was first obtained via Equation (3.3) using literature maximum concentrations of solute and surfactant given in Table 4.5. Next, K_{mw} was determined using $K_{mw} = x_{i,m}^{sat}/c_{i,w}^{sat}$, where values of $c_{i,w}^{sat}$ were supplied using our own solubility data (Chapter 2, Table 2.6). In preparing Table 4.5, we have reported our results using K_{mw}^{II}, which provides a better fit to measurements made near saturation and thus provides a more appropriate comparison with literature values.

Broadly, Table 4.5 shows our partition coefficients alongside those reported in other works. In regards to the solubilization of limonene, the $C_{12}E_{10}$ micelles exhibit a partition coefficient that is similar to diC_7PC, falling between values for diC_6PC and diC_8PC, and is larger than but similar in magnitude with those for $C_{16}E_{20}$ and $C_{16}E_{40}$ reported by Tokuoka et al. (1994). The decane K_{mw} value we measured in $C_{12}E_{10}$ solutions is also comparable to turbidity results from Binks et al. (1999) for $C_{12}E_n$ surfactants, as is octanol when compared to K_{mw} data in $C_{16}E_n$ micelles by Abe et al. (1992). Octanol partition coefficients determined by Saito et al. (1993) in $C_{12}E_9$ and $C_{12}E_{12}$ solutions, however, were almost two times higher. Turning to anionic surfactants, K_{mw} values we obtained by HS-SPME for limonene (Lloyd et al., 2011b) are significantly lower than those observed with nonionic or

zwitterionic micelles, in agreement with turbidity data by Abe et al. (1990). Partitioning results by Binks et al. (1990) for decane and by Abe et al. (1992) for octanol also indicate weaker partitioning into the charged surfactants. Note, the cmcs for most surfactants presented in Table 4.5 is provided in Appendix C.

Table 4.5. Partition coefficients at 25°C of solutes for various surfactants found within the literature

	K_{mw} (M^{-1})				
Surfactant	limonene	decane	1-octanol	Method	Reference
diC_6PC	2.37×10^3	—	—	HS–SPME	This work[b]
diC_7PC	5.10×10^3	—	—	HS–SPME	This work[b]
diC_8PC	5.96×10^3	—	—	HS–SPME	This work[b]
$C_{12}E_6$	—	7.93×10^5	—	Turbidity	Binks et al., 1999
$C_{12}E_8$	—	1.35×10^5	—	Turbidity	Binks et al., 1999
$C_{12}E_9$	—	—	278	Turbidity	Saito et al., 1993
$C_{12}E_{10}$	4.45×10^3	5.47×10^5	147	HS–SPME	This work[b]
$C_{12}E_{12}$	—	—	265	Turbidity	Saito et al., 1993
$C_{12}E_{19}$	—	—	257	Turbidity	Saito et al., 1993
$C_{16}E_{10}$	—	—	100[a]	Turbidity	Abe et al, 1992
$C_{16}E_{20}$	3.3×10^3 [a]	—	—	Turbidity	Tokuoka et al., 1992, 1994
$C_{16}E_{20}$	—	—	122[a]	Turbidity	Abe et al, 1992
$C_{16}E_{40}$	2.0×10^3 [a]	—	—	Turbidity	Tokuoka et al., 1992, 1994
SDS	1.2×10^3	—	—	Turbidity	Abe et al., 1990
SDS	1.7×10^3	—	—	HS–SPME	Lloyd et al., 2011b
SDS	—	—	91[a]	Turbidity	Abe et al, 1992
SDS	—	1.13×10^4	—	Turbidity	Binks et al., 1999
TTAB	—	6.58×10^4	—	Turbidity	Binks et al., 1999

[a] Measured at 30°C , [b] Measurements of this work reported using K_{mw}^{II}

From the n_{max} values given in Table 4.4, one can calculate $x_{i,m}^{sat}$ using Equation (3.3). These values are shown in Table 4.6. Decane, which has the lowest water solubility among these three solutes, exhibits the lowest $x_{i,m}^{sat}$, while the most water-soluble compound, 1-octanol, yields the highest $x_{i,m}^{sat}$. A comparison of $x_{i,m}^{sat}$ for limonene with the maximum mole fractions from our phospholipid results, given in Chapter 3, is also provided.

Table 4.6. Maximum mole fraction of solute $(x_{i,m}^{sat})$ within various micelles (this work).

	Decane	Limonene	Octanol
$C_{12}E_{10}$	0.26	0.45[a],0.46[b]	0.51
diC_6PC	—	0.25	—
diC_7PC	—	0.51	—

[a]$C_{12}E_{10}$=200mM, [b]$C_{12}E_{10}$=10mM

An interesting finding among these studies is that molar solubilization ratio (MSR, Equation (3.16)), at saturation, was observed to be independent of the total amount of surfactant of a given system at saturation, even at very large amounts of total surfactant (Binks et al., 1999, Tokuoka et al., 1994). That is, MSR only depended on the relative amount of surfactant and solute in the aggregate and not on their absolute amounts. Similar observations have been reported for other solute/surfactant systems using headspace techniques (Nagarajan and Ruckenstein, 1991). The MSR is the ratio of moles of solute to surfactant within the micelle and is related to the mole fraction $x_{i,m}$ for solute within micelles: $MSR = \frac{x_{i,m}}{1-x_{i,m}}$ .Given this, in Figure 4.4, we plot $c_{i,v}/c_{i,v}^{sat}$ versus $x_{i,m}$ for the entire solubilization isotherm of limonene in aqueous solutions of 10mM $C_{12}E_{10}$ and 200mM

$C_{12}E_{10}$. The overlap between the two is evident. Our results show this correspondence holds over the entire range of mole fractions, not just at saturation where the mole fraction is maximum.

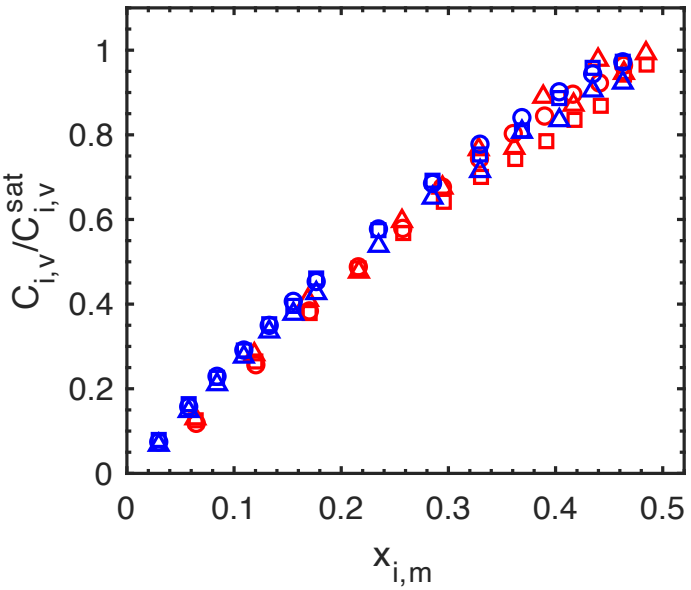

Figure 4.4. Solubilization isotherms for replicate samples (○, □, Δ) of limonene in 10mM (red) or 200mM $C_{12}E_{10}$ (blue) as function of solute mole fraction within micelles

Additionally, a couple of interesting trends are apparent from Table 4.5. First, we note for these systems are somewhat larger than those reported in solutions containing either $C_{12}E_{20}$ or $C_{12}E_{40}$ (Tokuoka et al., 1994). It would seem that relative size of the head group to tail length is of importance in governing solubilization thermodynamics. A larger headgroup would not only influence packing and structure but would result in a larger palisade layer. Diminished K_{mw} values with increasing polyethylene oxide head group size (relative to hydrocarbon tail length) have been observed in the literature for other C_nE_m surfactants using solutes 1-octanol and decane (Table 4.5).

4.3.3 Effects of Solute Properties on Solubilization

The differences in $x_{i,m}^{sat}$ amongst solutes suggests there is an underlying solute–surfactant relationship which governs the maximum amount of solute that can be solubilized within these micellar solutions.

For instance, previous research would indicate that the molecular volume of solute is of importance. Chaiko et al. (1984) experimentally measured the molar solubilization ratio at saturation (MSR^{sat}), which can be related to $x_{i,m}^{sat}$ through Equation (3.16), for various hydrocarbons. These solutes were dissolved in aqueous surfactant solutions composed of sodium dodecyl sulfate (SDS), cetyl pyridinium chloride (CPC), or dodecyl ammonium chloride (DAC). In all cases, they found that the molecular volume appeared inversely correlated with MSR^{sat}. Since SDS and DAC contain a twelve-carbon tail, the variation in MSR^{sat} values, for a given solute, was attributed to differences in the surfactants' polar head groups.

To better account for differences in polarity of solutes, Chaiko et al. (1984) proposed a dimensionless "volume-polarity" parameter, p_{vw}, defined as

$$p_{vw} = \sigma_{ow} v_o^{2/3} / kT. \tag{4.1}$$

Here, σ_{ow} is the solubilizate-water interfacial tension, v_o is molecular volume of the solute, and kT is the thermal energy. The importance of σ_{ow} is that it acts to quantitively capture the effect of solute polarity stemming from the aromatic character of hydrocarbon solutes. Based on their own experimental measurements, the Chaiko group was able to better distinguish aromatic from aliphatic hydrocarbon solutes, as compared to plots of MSR versus v_o alone. Experimental values of σ_{ow} for solutes in our studies, together with values of solute molecular volume (v_o), were used to calculate the volume-polarity parameter p_{vw}, given in Table 4.7 below. The molecular volume was determined from the density of pure solute at 20°C (Rumble, 2021).

Table 4.7. Properties of studied solutes at 20°C

	MW (g/mol)	ρ_i (g/mL)	v_o $(Å^3)$[a]	σ_{ow} (mN/m)	p_{vw}
Decane	142.29	0.73	323	52.33 (Zeppieri et al., 2001)	5.99
Limonene	136.24	0.841	269	44±0.5 (Pérez-Mosqueda et al., 2013)	4.45
1-Octanol	130.23	0.826	260	8.23[a] (Villers and Platten, 1988)	0.79
Tributyrin	302.36	1.032	487	7 (Burns et al., 1983)	1.05
Trihexanoin	386.5	1.001	641	18.6 (Benerito et al., 1956)	3.36

[a]Calculated using a second order polynomial fit at 20°C

Figure 4.5 presents measured MSR^{sat} values versus p_{vw} and v_o for solutes in aqueous solutions of surfactant as given by Chaiko et al. (1984), Roberts et al. (1983), and the current work. The surfactants used in each of these studies have similarly sized alkyl tails of 12–14 carbons, but varying headgroups. Plotting the MSR^{sat} of the solutes together in different surfactant micelles allows us to determine if there are any consistent trends in the MSR^{sat} which can be established with changes in either p_{vw} or v_o. Figure 4.5(a) shows an apparent inverse correlation between MSR^{sat} versus p_{vw} for the hydrocarbon solutes, despite the differences in surfactant types. However, more polar solutes, including triacylglycerol esters and octanol, fall outside of this general trend. Figure 4.5(b) presents MSR^{sat} data versus v_o of the solute. Here the data among all studied solutes shows a consistent, approximately exponential, decay of MSR^{sat} associated with increasing v_o. It appears that the collective micelles have less capacity for bulkier solutes than smaller ones, perhaps owing to lower packing efficiency due to steric limitations, and this trend holds even for more polar solutes such as octanol and tributyrin. In fact, the MSR^{sat} in Figure 4.5(b) falls close to a single correlation curve, despite being obtained in micelle solutions of several different surfactant types and measured by

various methods. Evidently, the MSR^{sat} in molecular size alone is a useful predictor for MSR relative for a range of solutes.

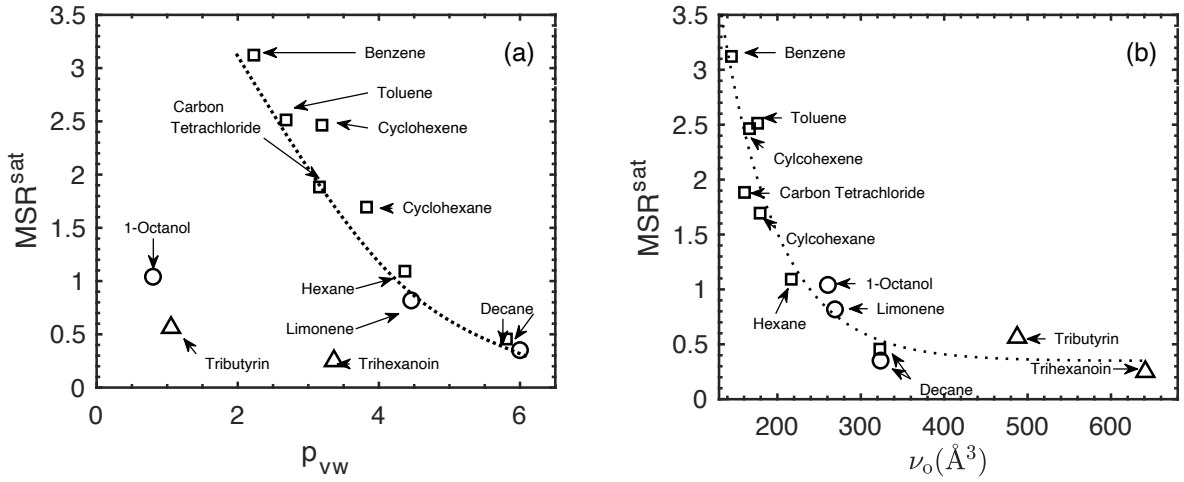

Figure 4.5. Molar solubilization ratios at saturation plotted against (a) the volume-polarity parameter p_{vw} or (b) the solute molecular volume for solutes in 200mM $C_{12}E_{10}$ (circles, this work), 100mM CPC (squares, Chaiko et al., 1984), 80mM diC_7PC (triangles, Roberts et al., 1983).

4.3.4 Measuring Changes in Solute Chemical Potential with Added Solute or Surfactant

Attention is next given to determination of solute chemical potentials. The chemical potential of solute was evaluated by use of normalized vapor concentrations provided by our SPME experiments. The chemical potential of solute in micelles can be equated at equilibrium to that of individual solute molecules dissolved in the water continuum. The latter can be treated as an ideal-dilute micellar solution, so that the chemical potential of solute in micelles can be written as

$$\mu_{i,m} = \mu_{i,w} = \mu_i = \mu_{i,w}^{\ominus} + kTlnx_{i,w}. \quad (4.2)$$

Here $\mu_{i,m}$ is the chemical potential of solute within micelles, $\mu_{i,w}$ is the chemical potential of solute dissolved within water, $\mu_{i,w}^{\ominus}$ is the solute's ideal-dilute reference chemical potential, and $x_{i,w}$ is the mole fraction of solute in water. Note that the chemical potential is equivalent between all phases and

hence μ_i, written without phase specificity, indicates the chemical potential of solute in the system. If the solution is saturated with solute, then Equation (4.2) becomes

$$\mu_i^{sat} = \mu_{i,w}^{\ominus} + kTlnx_{i,w}^{sat}. \tag{4.3}$$

Subtracting Equation (4.3) from Equation (4.2) gives

$$\mu_i - \mu_i^{sat} = kTln\left(\frac{x_{i,w}}{x_{i,w}^{sat}}\right). \tag{4.4}$$

Application of Henry's Law to Equation (4.4) gives

$$\mu_i - \mu_i^{sat} = kTln\left(\frac{p_i}{p_i^{sat}}\right), \tag{4.5}$$

where p_i is the solute vapor pressure and p_i^{sat} is the solute's vapor pressure above a saturated aqueous solution. Finally, use of the ideal gas law on Equation (4.5) changes pressures into vapor concentrations, $c_{i,v}$, which finally gives

$$\mu_i - \mu_i^{sat} = kTln\left(\frac{c_{i,v}}{c_{i,v}^{sat}}\right). \tag{4.6}$$

If the water and the pure solute are nearly immiscible, then Equation (4.6) can be approximated as

$$\mu_i - \mu_i^{sat} \approx kTln\left(\frac{c_{i,v}}{c_{i,v}^{*}}\right), \tag{4.7}$$

where $c_{i,v}^{*}$ is the solute vapor concentration above pure solute.

From the mole balance in Equation (3.1), we can define the total amount of solute in the liquid as $n_{i,\ell} = n_{i,w} + n_{i,m} = n_{i,t} - n_{i,v}$, and therefore

$$c_{i,\ell} = n_{i,\ell}/V_w = \frac{1}{V_w}(n_{i,t} - V_v c_{i,v}). \tag{4.8}$$

A plot of $\mu_i - \mu_i^{sat}$ versus $c_{i,\ell}$, obtained from Equations (4.6) and (4.8) and from the data in Figure 4.3, is shown in Figure 4.6 below. In this figure, the trends associated with each solute appear exponential. For the least soluble compound, decane, the chemical potential rises the most sharply for

an increase in $c_{i,\ell}$, followed by limonene and then octanol (the most water soluble). Furthermore, as the solute concentration approaches its saturation concentration, $\mu_i - \mu_i^{sat}$ approaches zero, as expected.

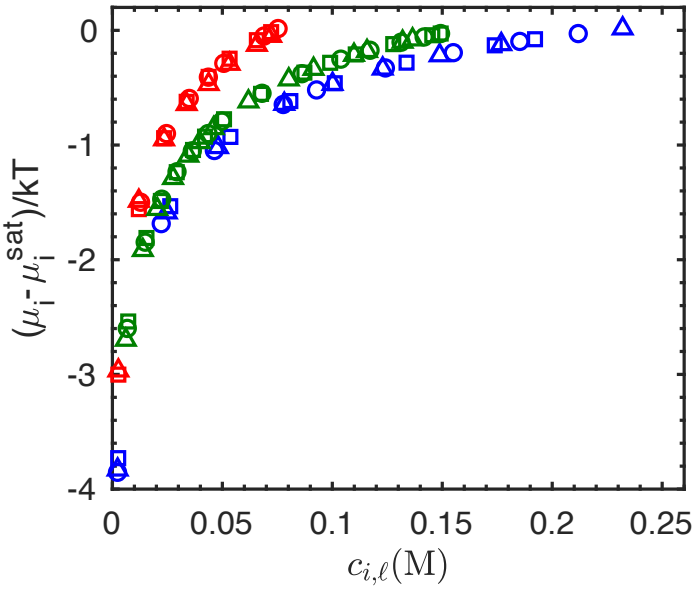

Figure 4.6. Chemical potentials of decane (red), octanol (blue), and limonene (green) calculated from replicate data sets (○, □, Δ) given from Figure 4.3

From the total mole balance, Equation (4.8) is

$$\frac{n_{i,\ell}}{V_w} = c_{i,w}\left(1 + \frac{K_{mw}c_{s,m}}{1 - K_{mw}c_{i,w}}\right), \tag{4.9}$$

which can be rewritten as

$$c_{i,\ell} = c_{i,w}\left(1 + \frac{K_{mw}c_{s,m}}{f(c_{i,w})}\right). \tag{4.10}$$

with $f(c_{i,w}) = 1 - K_{mw}c_{i,w}$. Rearrangement yields

$$0 = K_{mw}c_{i,\ell}c_{i,w} - c_{i,\ell} + c_{i,w} - K_{mw}c_{i,w}^2 + K_{mw}c_{s,m}c_{i,w}. \tag{4.11}$$

Solving for $c_{i,w}$ gives us

$$c_{i,w} = \frac{1}{2K_{mw}}\left[\beta - \left(\beta^2 - 4K_{mw}c_{i,\ell}\right)^{\frac{1}{2}}\right], \tag{4.12}$$

where $\beta = 1 + K_{mw}\left(c_{s,m} + c_{i,\ell}\right) = 1 + K_{mw}c_{s,m}(1+\rho)$ and $\rho = c_{i,\ell}/c_{s,m}$ is the ratio of solute to surfactant in the micellar solution. Equation (4.12) shows us that, with knowledge of K_{mw}, $c_{i,w}$ depends only on the known surfactant concentration $c_{s,m}$ and the total mole ratio ρ of solute to surfactant in the liquid solution. Next we can consider the case where $c_{i,w} \ll c_{i,\ell}$. Equation (4.10) becomes

$$c_{i,\ell} = \frac{K_{mw}c_{i,w}c_{s,m}}{1 - K_{mw}c_{i,w}} \tag{4.13}$$

or

$$c_{i,w} \approx \frac{c_{i,\ell}}{K_{mw}\left(c_{s,m} + c_{i,\ell}\right)} = \frac{1}{K_{mw}}\frac{\rho}{1+\rho}. \tag{4.14}$$

Now, recall Equation (4.2) expresses the chemical potential of solute in an aqueous micellar solution, based on that of the ideal-dilute solution of the molecularly dissolved solute. Then we can approximate Equation (4.2) as

$$\mu_i \approx \mu_i^{\ominus} + kTlnc_{i,w} + kTln\bar{v}_w, \tag{4.15}$$

where $\bar{v}_w$ is the volume of a water molecule, and the number of water molecules $n_w \gg n_{i,w}$.

Next, one can substitute $c_{i,w}$ from Equation (4.14) into Equation (4.15) to obtain

$$\mu_i \approx \mu_i^{\ominus} + kTln\bar{v}_w + kTln\frac{\rho}{1+\rho} - kTlnK_{mw}. \tag{4.16}$$

In Equation (4.16) K_{mw} is potentially a function of ρ. Equation (4.16) indicates that the solute chemical potential varies only with the solute-to-surfactant molar ratio in solution.

In Figure 4.7(a–c) we plot the expression

$$(\mu_i - \mu_i^{\ominus})/kT \equiv \mu_i^{th}/kT = ln\frac{\rho}{1+\rho} + ln\left(\frac{\bar{v}_w}{K_{mw}^{II}}\right) \tag{4.17}$$

for values $\rho = c_{i,\ell}/c_{s,m}$ corresponding to the range of values in Figure 4.6. In this theoretical prediction we used constant values K_{mw}^{II} for the micelle-water partition coefficient, as given in Table 4.4, and $\bar{v}_w$= 0.018 L/mol. The vertical shift between μ_i^{th}/kT and the experimental data, replotted versus $ln\frac{\rho}{1+\rho}$ in the figure, represents a difference, $\Delta\mu^{ref}/kT$, between experimental and theoretical reference potentials:

$$\frac{\Delta\mu^{ref}}{kT} = \frac{\left(\mu_i^{\ominus} - \mu_i^{sat}\right)}{kT}. \tag{4.18}$$

If we fit the experimental data at the smallest value $\rho = \rho_{min}$ to the expression $\frac{\mu_i^{th}}{kT} + b$, where the assumption that K_{mw} is most accurate, we obtain an estimate $b = \frac{\Delta\mu^{ref}}{kT}$ from the fit parameter b, as shown in Figure 4.7(d–f). One may also recognize that $\Delta\mu^{ref}$ in Equation (4.18) is equal to the chemical potential difference $(\mu_i^{\ominus} - \mu_i^{sat})$ inside the exponential in Equation (2.20). Equation (2.20) can thus be rearranged to use as an alternate way to estimate $\Delta\mu^{ref}$:

$$\frac{\Delta\mu^{ref}}{RT} = \ln\left(\frac{RTK_{vw}}{p_i^* \bar{v}_W}\right) = B. \tag{4.19}$$

Here p_i^* is the saturated vapor pressure of solute at temperature T, and K_{vw} is evaluated using results in Table 2.2, together with literature values of p_i^*. The resulting quantities B and b are given in Table 4.8 below, showing close agreement between the two ways to estimate $\Delta\mu^{ref}$.

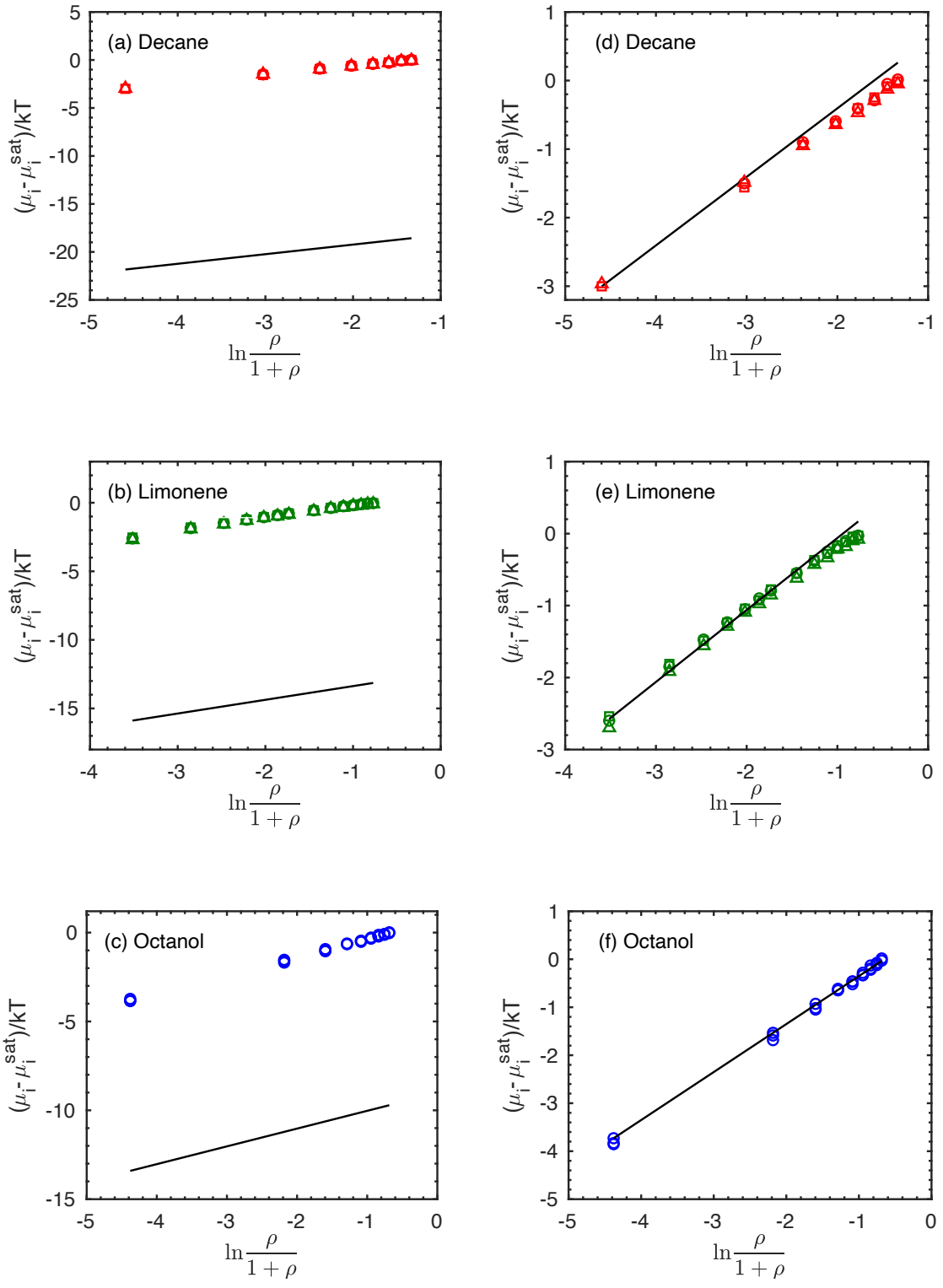

Figure 4.7. (a–c) Chemical potentials of decane (red), limonene (green), and octanol (blue), calculated from replicate data sets (○, □, Δ). Theoretical values (black) obtained from Equation (4.17). In (d–f) the theoretical values have been shifted vertically as described in the text

Table 4.8. Calculated values of B and b as obtained from experimental data at 298K

	B (no surfactant)	b $(C_{12}E_{10})$
[a]Decane	18.78	[d]18.83
[b]Limonene	13.76	[e]13.31
[c]1-Octanol	9.48	[e]9.67

[a]p_i^*=192 Pa at T=298K using data interpolated from Chirico et al. (1989)
[b]p_i^*=189 Pa at T=298K from Massaldi and King (1973)
[c]p_i^*=10.26 Pa at T=298K from Kulikov et al. (2001)
[d]ρ_{min}=0.0030
[e]ρ_{min}=0.0063

Quantities B and b physically represent the Gibbs energy to transfer one solute molecule from pure solute into water. For more polar compounds this transfer energy is approximated as coming from enthalpic contributions alone (i.e., the molar enthalpy of dissolution $(\Delta_d \overline{H})$ previously described in Chapter 2). However, for more hydrophobic compounds entropy changes during dissolution also contribute significantly. To assess the plausibility of these values, we compared our B results with calorimetric data reported by Baldwin (1986) for various hydrophobic solutes, which is given in Table 4.9 below. The data shows similarities between octanol and toluene, and limonene and hexane, reflecting effects of polarity, number of carbons, and cyclic/acyclic shape, on the transfer energy. A second trend observed is the apparent linear increase in $\Delta\mu^{ref}$ with aliphatic chain length for alkanes, which is shown in Figure 4.8.

Table 4.9. Values of the transfer Gibbs energy associated with moving one solute molecule from pure solute to water as given by Baldwin (1986) and this work

Compound	$\Delta\mu^{ref}$ (kJ/mol)	Source
Benzene	19.38	(Baldwin, 1986)
Toluene	22.80	(Baldwin, 1986)
Octanol	23.49	(This work)
Ethyl Benzene	26.19	(Baldwin, 1986)
Cyclohexane	28.12	(Baldwin, 1986)
Pentane	28.50	(Baldwin, 1986)
Hexane	32.53	(Baldwin, 1986)
Limonene	34.09	(This work)
Decane	46.54	(This work)

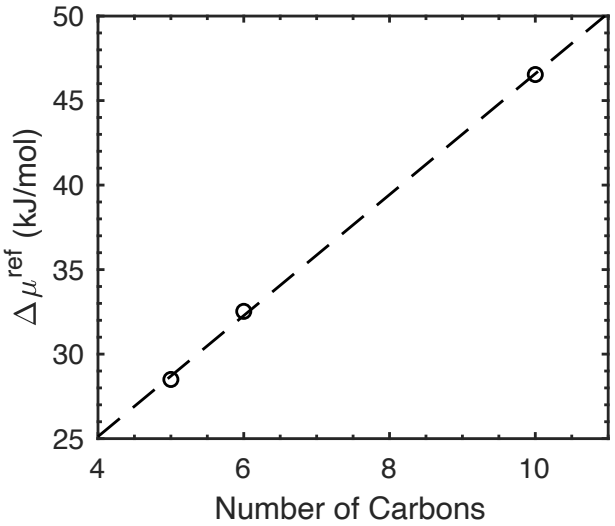

Figure 4.8. Gibbs transfer energies per molecule plotted against carbon number for alkanes within Table 4.9

4.3.5 Measuring Changes in Decane Chemical Potential with Added $C_{12}E_{10}$

Recall that an alternative way of constructing a solubilization isotherm is to vary surfactant for fixed amounts of solute (see §3.3.1). Raw peak area measurements for six solubilization isotherms made up of decane in varying concentrations of aqueous $C_{12}E_{10}$ solutions are given in Figure 4.9. As expected,

an increase in surfactant concentration led to a decrease in the decane vapor concentration. For each replicate set (○, □, Δ), three reference standards prepared of pure decane solute were also measured. The average and standard deviation of these measurements are shown in Table 4.10.

Table 4.10. Replicate sets of HS-SPME peak areas above pure decane added to 21.7 mL vials

Total Decane Added (*m*moles)	Set	Peak Area[a] (Pure decane) n=3
6	1	$6.38\pm0.50\times10^{5}$
	2	$9.78\pm1.15\times10^{5}$
	3	$3.260\pm0.043\times10^{6}$
30.1	1	$1.044\pm0.094\times10^{6}$
	2	$3.260\pm0.043\times10^{6}$
	3	$1.621\pm0.016\times10^{6}$
60	1	$1.995\pm0.095\times10^{6}$
	2	$1.621\pm0.016\times10^{6}$
	3	$1.686\pm0.054\times10^{6}$
90.6	1	$1.044\pm0.094\times10^{6}$
	2	$1.906\pm0.034\times10^{6}$
	3	$1.995\pm0.095\times10^{6}$
151.3	1	$1.54\pm0.11\times10^{6}$
	2	$1.843\pm0.053\times10^{6}$
	3	$1.534\pm0.038\times10^{6}$
212.9	1	$1.54\pm0.11\times10^{6}$
	2	$1.844\pm0.053\times10^{6}$
	3	$1.634\pm0.048\times10^{6}$

[a]Error bars represent 1 standard deviation of 3 measurements made on the same day.

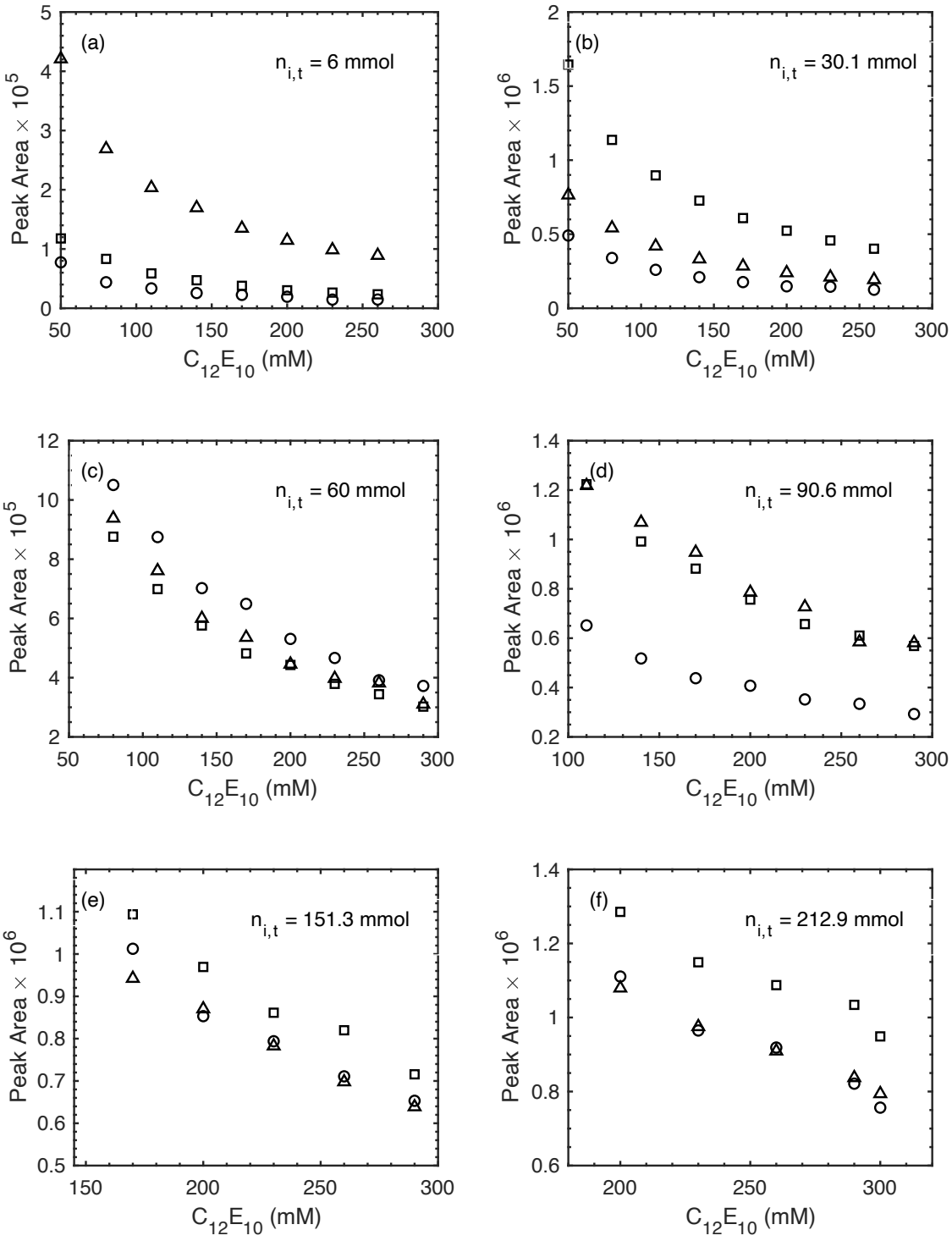

Figure 4.9. Raw peak areas of replicate sets (○, □, Δ) at varying total amounts of decane (a–f) plotted against varying concentrations of $C_{12}E_{10}$ in solution. Liquid volumes were 3 mL and total vial volumes were 21.7 mL

Each replicate set shown in Figure 4.10 was normalized by the average pure decane reference standard given in Table 4.10. The result of these normalizations is shown in Figure 4.10 below.

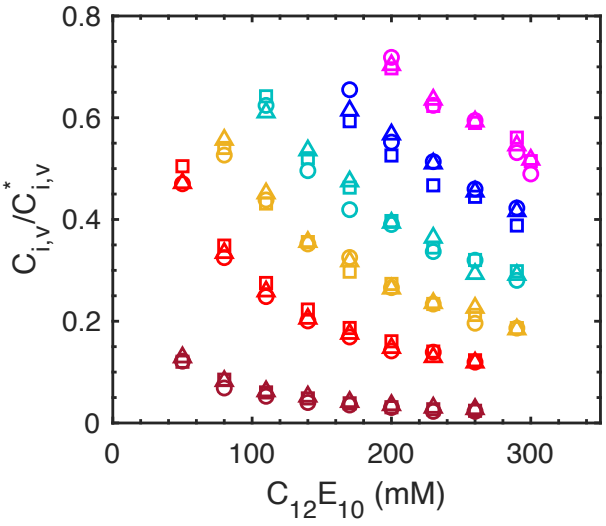

Figure 4.10. Replicate measurements (○, □, Δ) of decane vapor concentration relative to vapor concentrations above pure decane vapor at $n_{i,t}$ equal to 6 μmol (brown), 30.1 μmol (red), 60 μmol (yellow), 90.6 μmol (teal), 151.3 μmol (blue), and 212.9 μmol (magenta). Liquid volumes were 3 mL and total vial volumes were 21.7 mL

Using Equation (4.6), the data in Figure 4.10 was transformed into plots of $(\mu_i - \mu_i^*)/kT$ versus $C_{12}E_{10}$ (mM), which are shown in Figure 4.11. As expected, an increase in the surfactant concentration lowers decane's chemical potential for any given isotherm. Using data from Figure 4.10 we can construct a new figure that is analogous to Figure 4.7, shown in Figure 4.12 below. As before, chemical potential data at the lowest decane concentration data, corresponding to a solute-to-surfactant ratio ρ=0.0076, was fit to $\frac{\mu_i^{th}}{kT} + b$. At this lowest solute concentration, the assumption of an ideal-dilute mixture is best satisfied.

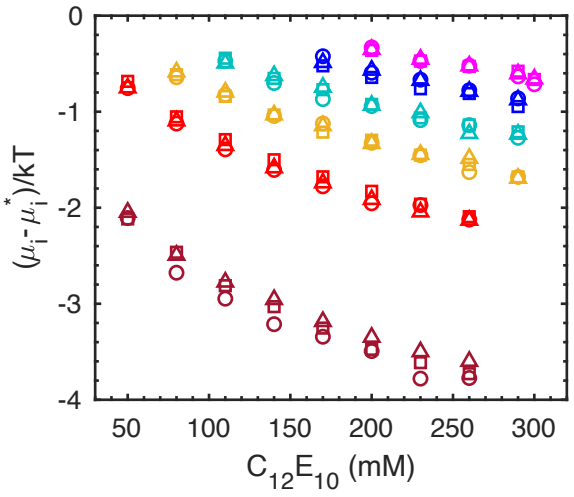

Figure 4.11. Calculated chemical potentials from the solubilization isotherms given in Figure 4.10 at $n_{i,t}$ equal to 6 μmol (brown), 30.1 μmol (red), 60 μmol (yellow), 90.6 μmol (teal), 151.3 μmol (blue), and 212.9 μmol (magenta).

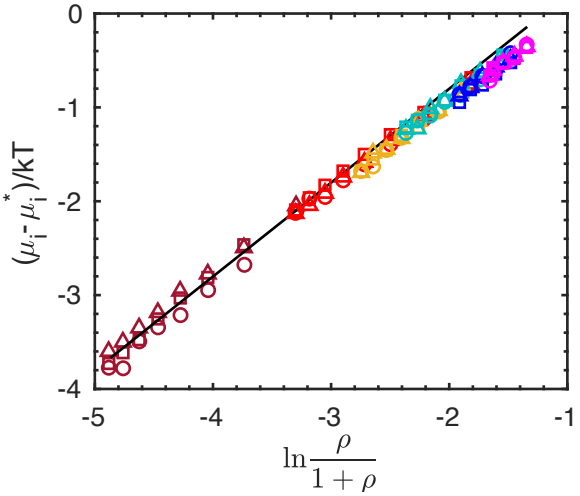

Figure 4.12. Chemical potential of decane for varying ratios of decane to $C_{12}E_{10}$. Black line is described by Equation (4.17) and shifted vertically as described in the text.

Figure 4.12 shows the collapse of data from Figure 4.10 onto a single curve. This parallels our findings given in Figure 4.4, in which changes in relative vapor concentration depend on the relative ratios of solute to surfactant and not their absolute amounts, and is consistent with thermodynamic theory for these mixtures. We also find, however, that the largest values of $\frac{\mu_i - \mu_i^*}{kT}$ in Figure 4.12 start

to fall slightly below the predictions of ideal-dilute solution theory (black line) using our fitted b value. This deviation is consistent with an increase in K_{mw} with increasing solute concentration at higher ρ values, as also seen in Figure 3.9 (Chapter 3). Table 4.11 provides a comparison of b values as calculated from Figure 4.7(d) and Figure 4.12. As noted in Table 4.11, experiments reported in these two figures used slightly different reference standards, as previously discussed in §4.3.1. Thus, exact agreement in b values is not expected due to the resulting small differences in reference vapor concentrations. With this context, we find that the two estimates of $\Delta\mu^{ref}$ for decane are in good agreement, providing further support for this thermodynamic analysis.

Table 4.11. Comparison of chemical potentials relative to infinite dilution

	b	
	$\frac{(\mu_i^{\ominus} - \mu_i^{sat})}{kT}$	$\frac{(\mu_i^{\ominus} - \mu_i^{*})}{kT}$
Decane	18.43	18.37

4.4 Summary

HS-SPME experiments were conducted to study solubilization phenomena for hydrophobic compounds dissolved in aqueous $C_{12}E_{10}$ solutions. Micelle-water partition coefficients were determined for octanol, limonene and decane, and our results show that their values increased with decreases in their respective solute's aqueous solubility. Coupled with this observation, we found that the maximum extent of solubilization appeared to be inversely correlated with solute molecular volume. Our thermodynamic analysis indicates that solute chemical potential is well-predicted from knowing only the total solute-to-surfactant ratio ρ and the partition coefficient K_{mw}. The latter was approximately constant for all ρ values for solutes limonene and octanol, but increased slightly at

higher ρ for decane: specifically for ρ greater than 0.15. Finally, values of our newly defined theoretical reference chemical potential in $C_{12}E_{10}$ solutions appear self-consistent to those derived in our surfactant-free systems, and yield values for the Gibbs energy of dissolution per solute molecule in good agreement with existing literature.

4.5 Nomenclature

$C_{12}E_{10}$ ..... decaethylene glycol monododecyl ether

K_{mw} ..... micelle-water partition coefficient; $x_{i,m}/c_{i,w}$

K_{mw}^{II} ..... micelle-water partition coefficient obtained over entire solute range, up to solubility limit

n_{max} ..... maximum moles of solute that can be dissolved in solution

V_w ..... volume of water

V_t ..... total volume

$c_{i,v}$ ..... concentration of solute in vapor

$c_{i,v}^{sat}$ ..... concentration of solute in saturated vapor

$c_{i,w}$ ..... concentration of solute in water

K_{vw} ..... vapor-water partition coefficient; $c_{i,v}/c_{i,w}$

$c_{s,m}$ ..... concentration of surfactant in micelles

cmc ..... critical micelle concentration

$\bar{v}_w$ ..... molar volume of water

$x_{i,m}$ ..... mole fraction of solute in micelles

$n_{i,t}$ ..... total moles of solute

$n_{i,v}$ ..... moles of solute in vapor

$n_{i,\ell}$ ..... moles of solute in solution

$c_{i,\ell}$ ..... concentration of solute in solution

$x_{i,m}^{sat}$ ..... mole fraction of solute in micelles at saturation

σ_{ow} ..... solubilizate-water interfacial tension

v_o ..... molecular volume of the solute

kT ..... thermal energy

p_{vw} ..... volume-polarity parameter, $\sigma_{ow} v_o^{2/3}/kT$

MW ..... molecular weight of solute

ρ_i ..... density of solute

$\mu_{i,m}$ ..... chemical potential of solute within micelles

$\mu_{i,w}$ ..... chemical potential of solute in water

μ_i ..... chemical potential of solute without phase specificity

$\mu_i^{\ominus}$ ..... solute's ideal-dilute reference chemical potential

p_i ..... solute's vapor pressure

p_i^{sat} ..... solute's vapor pressure above a saturated aqueous solution

p_i^* ..... solute's vapor pressure above pure solute

b ..... $\frac{\Delta\mu^{ref}}{kT} = \frac{\left(\mu_i^{\ominus} - \mu_i^{sat}\right)}{kT}$

B ..... $\frac{\Delta\mu}{RT} = \ln\left(\frac{RTK_{vw}}{p_i^* \bar{v}_W}\right)$

ρ ..... solute-to-surfactant molar ratio

Bibliography

Abe, M., Tokuoka, Y., Uchiyama, H., Ogino, K., 1990. Solubilization of Synthetic Perfumes by Sodium Dodecyl Sulfate. J. Japan Oil Chem. Soc. 39, 565–571. https://doi.org/10.5650/jos1956.39.8_565

Abe, M., Tokuoka, Y., Uchiyama, H., Ogino, K., Scamehorn, J.F., Christian, S.D., 1992. Expansion of mixed anionic-non-ionic micelles caused by solubilization of organic solutes. Colloids and Surfaces 67, 37–43. https://doi.org/10.1016/0166-6622(92)80283-8

Alberts, B., Johnson, A., Lewis, J., Al., E., 2002. Molecular Biology of the Cell, 4th ed. Garland Sciences, New York, NY.

Alexander, N.P., Phillips, R.J., Dungan, S.R., 2021. Multicomponent diffusion of interacting, nonionic micelles with hydrophobic solutes. Soft Matter 17, 531–542. https://doi.org/10.1039/d0sm01406k

Alexander, N.P., Phillips, R.J., Dungan, S.R., 2019. Multicomponent Diffusion in Aqueous Solutions of Nonionic Micelles and Decane. Langmuir 35, 13595–13606. https://doi.org/10.1021/acs.langmuir.9b01823

Armstrong, D.W., Nome, F., 1981. Partitioning behavior of solutes eluted with micellar mobile phases in liquid chromatography. Anal. Chem. 53, 1662–1666. https://doi.org/10.1021/ac00234a026

Arunyanart, M., Cline Love, L.J., 1984. Model for Micellar Effects on Liquid Chromatography Capacity Factors and for Determination of Micelle-Solute Equilibrium Constants. Anal. Chem. 56, 1557–1561. https://doi.org/10.1021/ac00273a005

Baek, K., Lee, H.H., Cho, H.J., Yang, J.W., 2003. Headspace Solid-Phase Microextraction for Determination of Micellar Solubilization of methyl tert-butyl ether (MTBE). Korean J. Chem. Eng. 20, 698–701. https://doi.org/10.1007/BF02706910

Baldwin, R.L., 1986. Temperature dependence of the hydrophobic interaction in protein folding. Proc. Natl. Acad. Sci. U. S. A. 83, 8069–8072. https://doi.org/10.1073/pnas.83.21.8069

Berthod, A., Tomer, S., Dorsey, J.G., 2001. Polyoxyethylene alkyl ether nonionic surfactants: Physicochemical properties and use for cholesterol determination in food. Talanta 55, 69–83. https://doi.org/10.1016/S0039-9140(01)00395-2

Blankschtein, D., Thurston, G.M., Benedek, G.B., 1986. Phenomenological theory of equilibrium thermodynamic properties and phase separation of micellar solutions. J. Chem. Phys. 85, 7268–7288. https://doi.org/10.1063/1.451365

Blankschtein, D., Thurston, G.M., Benedek, G.B., 1985. Theory of phase separation in micellar solutions. Phys. Rev. Lett. 54, 955. https://doi.org/10.1103/PhysRevLett.54.955

Bonsen, P.P.M., de Haas, G.H., Pieterson, W.A., Van Deenen, L.L.M., 1972. Studies on phospholipase a and its zymogen from porcine pancreas IV. The influence of chemical modification of the lecithin structure on substrate properties. Biochim. Biophys. Acta (BBA)/Lipids Lipid Metab. 270, 364–382. https://doi.org/10.1016/0005-2760(72)90200-7

Brady, J.W., 2013. Introductory Food Chemistry. Cornell University Press, Ithaca.

Burns, R.A., Donovan, J.M., Roberts, M.F., 1983. Structural Analysis of Short-Chain Lecithin/Triglyceride Micellar Particles. Biochemistry 22, 964–973.

Burns, R.A., Friedman, J.M., Roberts, M.F., 1981. Characterization of Short-Chain Alkyl Ether Lecithin Analogues: 13C NMR and Phospholipase Studies. Biochemistry 20, 5945–5950. https://doi.org/10.1021/bi00524a004

Burns, Ramon A, Roberts, M., 1981a. Cholesterol Solubilization by Short-Chain Lecithins: Characterization of Mixed Micelles and Cholesterol Oxidase Activity. Biochemistry 20, 7102–7108. https://doi.org/10.1021/bi00528a008

Burns, Ramon A, Roberts, M.F., 1981b. Physical characterization and lipase susceptibility of short chain lecithin/triglyceride mixed micelles. Potential lipoprotein models. J. Biol. Chem. 256, 2716–2722. https://doi.org/10.1016/s0021-9258(19)69674-2

Carvalho, B.L., Briganti, G., Chen, S.H., 1989. Lowering of the miscibility gap in the dioctanoylphosphatidylcholine-water system by addition of urea. J. Phys. Chem. 93, 4282–4286. https://doi.org/10.1021/j100347a073

Chaiko, M.A., Nagarajan, R., Ruckenstein, E., 1984. Solubilization of single-component and binary mixtures of hydrocarbons in aqueous micellar solutions. J. Colloid Interface Sci. 99, 168–182. https://doi.org/10.1016/0021-9797(84)90097-3

Chen, L.J., Lin, S.Y., Huang, C.C., Chen, E.M., 1998. Temperature dependence of critical micelle concentration of polyoxyethylenated non-ionic surfactants. Colloids Surfaces A Physicochem. Eng. Asp. 135, 175–181. https://doi.org/10.1016/S0927-7757(97)00238-0

Chojnacka, A., Gladkowski, W., Kielbowicz, G., Wawrzenczyk, C., 2012. Isolation of egg-yolk phospholipids and enzymatic modification of their acyl chains. Lipid Technol. 24, 33–35. https://doi.org/10.1002/lite.201200171

Chojnacka, A., Gładkowski, W., Kiełbowicz, G., Wawrzeńczyk, C., 2009. Enzymatic enrichment of egg-yolk phosphatidylcholine with α-linolenic acid. Biotechnol. Lett. 31, 705–709. https://doi.org/10.1007/s10529-009-9915-6

Christian, S.D., Tucker, E.E., Lane, E.H., 1981. Precise vapor pressure measurements of the solubilization of cyclohexane by sodium octyl sulfate and sodium octyl sulfate micelles. J. Colloid Interface Sci. 84, 423–432. https://doi.org/10.1016/0021-9797(81)90233-2

Copolovici, L. O., & Niinemets, Ü. (2005). Temperature dependencies of Henry's law constants and octanol/water partition coefficients for key plant volatile monoterpenoids. *Chemosphere*, *61*, 1390–1400. https://doi.org/10.1016/j.chemosphere.2005.05.003

De Haas, G.H., Bonsen, P.P.M., Pieterson, W.A., Van Deenen, L.L.M., 1971. Studies on phospholipase A and its zymogen from porcine pancreas. III. Action of the enzyme on short-chain lecithins. Biochim. Biophys. Acta (BBA)/Lipids Lipid Metab. 239, 252–266. https://doi.org/10.1016/0005-2760(71)90171-8

Dill, K.A., Bromberg, S., 2011. Molecular Driving Forces: Statistical Thermodynamics in Biology, Physics, and Nanoscience. Garland Sciences, London.

Đorđević, V., Balanč, B., Belščak-Cvitanović, A., Lević, S., Trifković, K., Kalušević, A., Kostić, I., Komes, D., Bugarski, B., Nedović, V., 2014. Trends in Encapsulation Technologies for Delivery of Food Bioactive Compounds, Food Engineering Reviews. https://doi.org/10.1007/s12393-014-9106-7

Duan, X., Liu, X., Dong, Yue, Duan, T., Zhang, J., He, S., Yang, F., Dong, Yuming, 2020. A Mixed Micellar Liquid Chromatography with Direct Injection for Rapid Analysis of Eight Sulfonamides in Milk. Food Anal. Methods 13, 1148–1158. https://doi.org/10.1007/s12161-020-01733-3

Eastoe, J., Dalton, J.S., Heenan, R.K., 1998. Dynamic Surface Tensions and Micelle Structures of Dichained Phosphatidylcholine Surfactant Solutions. Langmuir 14, 5719–5724. https://doi.org/10.1021/la980053i

Ettre, L.S., Welter, C., Kolb, B., 1993. Determination of gas-liquid partition coefficients by automatic equilibrium headspace-gas chromatography utilizing the phase ratio variation method. Chromatographia 35, 73–84. https://doi.org/10.1007/BF02278560

Evans, D.F., Allen, M., Ninham, B.W., Fouda, A., 1984. Critical micelle concentrations for alkyltrimethylammonium bromides in water from 25 to 160°C. J. Solution Chem. 13, 87–101. https://doi.org/10.1007/BF00646042

Fieber, W., Frank, S., Herrero, C., 2018. Competition between surfactants and apolar fragrances in micelle cores. Colloids Surfaces A Physicochem. Eng. Asp. 539, 310–318. https://doi.org/10.1016/j.colsurfa.2017.12.031

Gabriel, N.E., Roberts, M.F., 1987. Short-Chain Lecithin/Long-Chain Phospholipid Unilamellar Vesicles: Asymmetry Dynamics, and Enzymatic Hydrolysis of the Short-Chain Component. Biochemistry 26, 2432–2440. https://doi.org/10.1021/bi00383a006

Gossett, J.M., 1987. Measurement of Henry's Law Constants for C1 and C2 Chlorinated Hydrocarbons. Environ. Sci. Technol. 21, 202–208. https://doi.org/10.1021/es00156a012

Hauser, H., 2000. Short-chain phospholipids as detergents. Biochim. Biophys. Acta - Biomembr. 1508, 164–181. https://doi.org/10.1016/S0304-4157(00)00008-3

Hauser, H., Guyer, W., Pascher, I., Skrabal, P., Sundell, S., 1980. Polar Group Conformation of Phosphatidylcholine. Effect of Solvent and Aggregation. Biochemistry 19, 366–373. https://doi.org/10.1021/bi00543a018

Helburn, R., Albritton, J., Howe, G., Michael, L., & Franke, D. (2008). Henry's law constants for fragrance and organic solvent compounds in aqueous industrial surfactants. *Journal of Chemical and Engineering Data*, *53*, 1071–1079. https://doi.org/10.1021/je700418a

Høiland, H., Blokhus, A.M., 2009. Solubilization in Surfactant Systems, in: Birdi, K.S. (Ed.), Handbook of Surface and Colloid Chemistry, Second Edition. Taylor & Francis Group, LLC, Boca Raton, FL, pp. 382–386.

Høiland, H., Ljosland, E., Backlund, S., 1984. Solubilization of alcohols and alkanes in aqueous solution of sodium dodecyl sulfate. J. Colloid Interface Sci. 101, 467–471. https://doi.org/10.1016/0021-9797(84)90058-4

Huang, Y.X., Thurston, G.M., Blankschtein, D., Benedek, G.B., 1990. The effect of salt identity and concentration on liquid-liquid phase separation in aqueous micellar solutions of C8-lecithin. J. Chem. Phys. 92, 1956–1962. https://doi.org/10.1063/1.458026

Iyer, J., Mendenhall, J.D., Blankschtein, D., 2013. Computer simulation-molecular-thermodynamic framework to predict the micellization behavior of mixtures of surfactants: Application to

binary surfactant mixtures. J. Phys. Chem. B 117, 6430–6442. https://doi.org/10.1021/jp4001253

Jabbari, M., Teymoori, F., 2018. An insight into effect of micelle-forming surfactants on aqueous solubilization and octanol/water partition coefficient of the drugs gemfibrozil and ibuprofen. J. Mol. Liq. 262, 1–7. https://doi.org/10.1016/j.molliq.2018.04.054

Järvinen, K., Järvinen, T., Urtti, A., 1995. Ocular absorption following topical delivery. Adv. Drug Deliv. Rev. 16, 3–19. https://doi.org/10.1016/0169-409X(95)00010-5

Jiao, J., 2008. Polyoxyethylated nonionic surfactants and their applications in topical ocular drug delivery. Adv. Drug Deliv. Rev. 60, 1663–1673. https://doi.org/10.1016/j.addr.2008.09.002

Johnson, R.E., Wells, M.A., Rupley, J.A., 1981. Thermodynamics of Dihexanoylphosphatidylcholine Aggregation. Biochemistry 20, 4239–4242. https://doi.org/10.1021/bi00517a044

Kim, S., Shi, Y., Kim, J.Y., Park, K., Cheng, J.X., 2010. Overcoming the barriers in micellar drug delivery: Loading efficiency, in vivo stability, and micelle-cell interaction. Expert Opin. Drug Deliv. 7, 49–62. https://doi.org/10.1517/17425240903380446

Kulikov, D., Verevkin, S.P., Heintz, A., 2001. Enthalpies of vaporization of a series of aliphatic alcohols: Experimental results and values predicted by the ERAS-model. Fluid Phase Equilib. 192, 187–207. https://doi.org/10.1016/S0378-3812(01)00633-1

Lin, T.L., Tseng, M.Y., Chen, S.-H., Roberts, M.F., 1990. Temperature Dependence of the Growth of Diheptanoylphosphatidylcholine Micelles Studied. J. Phys. Chem 94, 7239–7243. https://doi.org/10.1021/j100381a052

Lin, T.L., Chen, S.H., Gabriel, N.E., Roberts, M.F., 1987. Small-angle neutron scattering techniques applied to the study of polydisperse rodlike diheptanoylphosphatidylcholine micelles. J. Phys. Chem. 91, 406–413. https://doi.org/10.1021/j100286a031

Lin, T.L., Chen, S.H., Gabriel, N.E., Roberts, M.F., 1986. The use of small-angle neutron scattering to determine the structure and interaction of dihexanoylphosphatidylcholine micelles. J. Am. Chem. Soc. 108, 3499–3507. https://doi.org/10.1021/ja00272a055

Livney, Y.D., 2015. Nanostructured delivery systems in food: Latest developments and potential future directions. Curr. Opin. Food Sci. 3, 125–135. https://doi.org/10.1016/j.cofs.2015.06.010

Lloyd, N.W., Dungan, S.R., Ebeler, S.E., 2011a. Measuring gas-liquid partition coefficients of aroma compounds by solid phase microextraction, sampling either headspace or liquid. Analyst 136, 3375–3383. https://doi.org/10.1039/c1an15270j

Lloyd, N.W., Kardaras, E., Ebeler, S.E., Dungan, S.R., 2011b. Measuring local equilibrium flavor distributions in SDS solution using headspace solid-phase microextraction. J. Phys. Chem. B 115, 14484–14492. https://doi.org/10.1021/jp206984q

Malliaris, A., 1987. Fluorescence probing in micellar solutions: organic additives in micelles of sodium dodecylsulphate. J. Photochem. 40, 79–85. https://doi.org/https://doi.org/10.1016/0047-2670(87)87046-6

Massaldi, H.A., King, C.J., 1973. Simple Technique to Determine Solubilities of Sparingly Soluble Organics: Solubility and Activity Coefficients of d-Limonene, n-Butylbenzene, and n-Hexyl Acetate in Water and Sucrose Solutions. J. Chem. Eng. Data 18, 393–397. https://doi.org/10.1021/je60059a024

Miller, D.J., Hawthorne, S.B., Gizir, A.M., Clifford, A.A., 1998. Solubility of polycyclic aromatic hydrocarbons in subcritical water from 298 K to 498 K. J. Chem. Eng. Data 43, 1043–1047. https://doi.org/10.1021/je980094g

Muggeo, V.M.R., 2003. Estimating regression models with unknown break-points. Stat. Med. 22, 3055–3071. https://doi.org/10.1002/sim.1545

Nagarajan, R., 2017. Constructing a molecular theory of self-assembly: Interplay of ideas from surfactants and block copolymers. Adv. Colloid Interface Sci. 244, 113–123. https://doi.org/10.1016/j.cis.2016.12.001

Nagarajan, R., 1996. Solubilization in aqueous solutions of amphiphiles. Curr. Opin. Colloid Interface Sci. 1, 391–401. https://doi.org/10.1016/s1359-0294(96)80139-7

Nagarajan, R., Barry, M., Ruckenstein, E., 1986. Unusual Selectivity in Solubilization by Block Copolymer Micelles. Langmuir 2, 210–215. https://doi.org/10.1021/la00068a017

Nagarajan, R., Ruckenstein, E., 2000. Molecular theory of microemulsions. Langmuir 16, 6400–6415. https://doi.org/10.1021/la991578t

Nostro, P. Lo, Murgia, S., Lagi, M., Fratini, E., Almgren, M., Monduzzi, M., Ninham, B.W., Baglioni, P., 2008. Interconnected Networks : Structural and Dynamic Characterization of Aqueous Dispersions of Dioctanoylphosphatidylcholine. J. Phys. Chem. B 12625–12634.

https://doi.org/https://doi.org/10.1021/jp803983t

Pawliszyn, J., 2012. Handbook of Solid Phase Microextraction. Elsevier Inc.

Pawliszyn, J., Pawliszyn, B., Pawliszyn, M., 1997. Solid phase micro extraction (SPME). Chem. Educ. 2, 1–7. https://doi.org/10.1007/s00897970137a

Pennell, K.D., Karagunduz, A., Young, M.H., 2003. Impacts of Surfactant Adjuvants on Pesticide Availability and Transport in Soils, in: Gan, J.J., Zhu, P.C., Aust, S.D., Lemley, A.T. (Eds.), Pesticide Decontamination and Detoxification, Vol. 863. American Chemical Society, pp. 231–245. https://doi.org/10.1021/bk-2004-0863.ch017

Peris-García, E., Rodríguez-Martínez, J., Baeza-Baeza, J.J., García-Alvarez-Coque, M.C., Ruiz-Angel, M.J., 2018. Search of non-ionic surfactants suitable for micellar liquid chromatography. Anal. Bioanal. Chem. 410, 5043–5057. https://doi.org/10.1007/s00216-018-1161-0

Philippe, E., Seuvre, A.M., Colas, B., Langendorff, V., Schippa, C., Voilley, A., 2003. Behavior of flavor compounds in model food systems: A thermodynamic study. J. Agric. Food Chem. 51, 1393–1398. https://doi.org/10.1021/jf020862e

Pino, V., Afonso, A.M., Ayala, J.H., González, V., 2007. Micellar solid-phase microextraction for determining partition coefficients of substituted polycyclic aromatic hydrocarbons in micellar media: Possible prediction of hydrocarbon-micelle behaviour. Anal. Bioanal. Chem. 387, 2271–2281. https://doi.org/10.1007/s00216-006-1029-6

Pino, V., Ayala, J.H., González, V., Alfonso, A.M., 2004. Solid-phase microextraction coupled to gas chromatography/mass spectrometry for determining polycyclic aromatic hydrocarbon-micelle partition coefficients. Anal. Chem. 76, 4572–4578. https://doi.org/10.1021/ac049915c

Roholt, A., Schlamowitz, M., 1961. Studies of the Use of Dihexanoyllecithin and Other as Substrates for Phospholipase A. Arch. Biochem. Biophys. 94, 364–379.

Rumble, J.R., 2021. CRC Handbook of Chemistry and Physics, 102nd ed. CRC Press/Taylor & Francis, Boca Raton, FL.

Saito, Y., Abe, M., Sato, T., 1993. Solubilization Behavior of n-Octane and n-Octanol in Polyoxyethylated Nonionic Micelles. J. Am. Oil Chem. Soc. 70, 717–721.

Smith, F.L., Harvey, A.H., 2007. Avoid common pitfalls when using Henry's law. Chem. Eng. Prog.

103, 33–39.

Song, M., Hu, D., Zheng, X., Wang, L., Yu, Z., An, W., Na, R., Li, C., Li, N., Lu, Z., Dong, Z., Wang, Y., Jiang, L., 2019. Enhancing Droplet Deposition on Wired and Curved Superhydrophobic Leaves. ACS Nano 13, 7966–7974. https://doi.org/10.1021/acsnano.9b02457

Stephenson, B.C., Beers, K.J., Blankschtein, D., 2007. Quantifying the hydrophobic effect. 3. A computer simulation - Molecular-thermodynamic model for the micellization of ionic and zwitterionic surfactants in aqueous solution. J. Phys. Chem. B 111, 1063–1075. https://doi.org/10.1021/jp065699v

Tanford, C., 1973. The Hydrophobic Effect. John Wiley & Sons, New York, NY.

Tausk, R.J.M., Karmiggelt, J. Van, Voordouw, G., Overbeek, J.T.G., 1974a. Physical Chemical Studies of Short–Chain Lecithin Homologues. II. Micellar Weights of Dihexanoyl and Diheptanoyllecithin. Biophys. Chem. 1 1, 184–203.

Tausk, R.J.M., Oudshoorn, C., Overbeek, J.T.G., 1974b. Physical chemical studies of short-chain lecithin homologues: III. Phase separation and light scattering studies on aqueous dioctanoyllecithin solutions. Biophys. Chem. 2, 53–63. https://doi.org/https://doi.org/10.1016/0301-4622(74)80024-4

Tausk, R.J.M., Overbeek, J.T.G., 1974. Physical chemical studies of short-chain lecithin homologues. I. Influence of the chain length of the fatty acid ester and of electrolytes on the critical micelle concentration. Biophys. Chem. 1, 175–183. https://doi.org/10.1016/0301-4622(74)80039-6

Taylor, A.J., 1996. Volatile Flavor Release from Foods during Eating. Crit. Rev. Food Sci. Nutr. 36, 765–784. https://doi.org/10.1080/10408399609527749

Tokuoka, Y., Uchiyama, H., Abe, M., 1994. Solubilization of some synthetic perfumes by anionic-nonionic mixed surfactant systems. 2. J. Phys. Chem. 98, 6167–6171. https://doi.org/10.1021/j100075a020

Tokuoka, Y., Uchiyama, H., Abe, M., Christian, S.D., 1995. Solubilization of Some Synthetic Perfumes by Anionic-Nonionic Mixed Surfactant Systems. 1. Langmuir 11, 725–729.

Tokuoka, Y., Uchiyama, H., Abe, M., Ogino, K., 1992. Solubilization of synthetic perfumes by nonionic surfactants. J. Colloid Interface Sci. 152, 402–409. https://doi.org/10.1016/0021-9797(92)90042-K

Tucker, E. E., & Christian, S. D. (1982). Precise vapour-pressure measurements of the solubilization of benzene by aqueous sodium octylsulphate solutions. *Faraday Symposia of the Chemical Society*, *17*, 11–24. https://doi.org/10.1039/FS9821700011

Tucker, E. E., & Christian, S. D. (1985). Solubilization of benzene by aqueous sodium octylsulfate: Effect of added sodium chloride. *Journal of Colloid and Interface Science*, *104*(2), 562–568. https://doi.org/10.1016/0021-9797(85)90063-3

Tsonopoulos, C., 1999. Thermodynamic analysis of the mutual solubilities of normal alkanes and water. Fluid Phase Equilib. 156, 21–33. https://doi.org/10.1016/S0378-3812(99)00021-7

Vane, L.M., Giroux, E.L., 2000. Henry ' s Law Constants and Micellar Partitioning of Volatile Organic Compounds in Surfactant Solutions. J. Chem. Eng. Data 45, 38–47. https://doi.org/10.1021/je990195u

Villers, D., Platten, J.K., 1988. Temperature dependence of the interfacial tension between water and long-chain alcohols. J. Phys. Chem. 92, 4023–4024. https://doi.org/10.1021/j100325a005

Wang, Y., O'Reilly, J., Chen, Y., Pawliszyn, J., 2005. Equilibrium in-fibre standardisation technique for solid-phase microextraction. J. Chromatogr. A 1072, 13–17. https://doi.org/10.1016/j.chroma.2004.12.084

Welke, B., Ettlinger, K., & Riederer, M. (1998). Sorption of volatile organic chemicals in plant surfaces. *Environmental Science and Technology*, *32*, 1099–1104. https://doi.org/10.1021/es970763v

Yang, C., Chen, F., Luo, S., Xie, G., Zeng, G., Fan, C., 2010. Effects of surfactants and salt on Henry's constant of n-hexane. J. Hazard. Mater. 175, 187–192. https://doi.org/10.1016/j.jhazmat.2009.09.147

Yao, C., Twu, P., Anderson, J.L., 2010. Headspace single drop microextraction using micellar ionic liquid extraction solvents. Chromatographia 72, 393–402. https://doi.org/10.1365/s10337-010-1675-x

Zeppieri, S., Rodríguez, J., López De Ramos, A.L., 2001. Interfacial tension of alkane + water systems. J. Chem. Eng. Data 46, 1086–1088. https://doi.org/10.1021/je000245r

Zhao, T., No, D.S., Kim, B.H., Garcia, H.S., Kim, Y., Kim, I.H., 2014. Immobilized phospholipase A1-catalyzed modification of phosphatidylcholine with n-3 polyunsaturated fatty acid. Food Chem. 157, 132–140. https://doi.org/10.1016/j.foodchem.2014.02.024

Appendix A

In-fibre Standardization Technique for SPME

External calibration curves are a common approach for determining the liquid concentration of analyte in a given sample. Here, standards of known concentration are prepared in vials containing matrices that closely match that of the target sample. A calibration plot of peak area versus the analyte's liquid concentration is then generated. Once the target sample is measured, its peak area is related to its liquid concentration through the calibration plot.

A second analytical technique is to use an internal standard, which may further improve the accuracy and reproducibility of the experiment. Here, the internal standard's physical properties should closely match that of the target analyte. If using a mass spectrometer detector, an ideal choice of an internal standard is to use a deuterated analyte, since (1) its analytical behavior is nearly identical to the analyte of interest and (2) its peak area can be readily screened from the target analyte's peak area in the resulting chromatogram. All samples are then typically spiked with the same known amount of standard which, in turn, acts as baseline 'reference' state. In this way, a secondary calibration curve is created in which ratio of analyte-to-internal standard peak area is then related to the ratio of analyte-to-internal standard liquid concentration. In doing so, the variability of instrument response is partially circumvented, as abnormally high or (low) instrument responses would be captured in both the target analyte and internal standard and their ratios would remain the same. An additional advantage is that day-to-day variability associated with utilizing absolute peak areas is eliminated, since only the ratios are of importance.

To avoid potential complications of matrix effects caused by direct addition of an internal standard to solution, we chose instead to standardize the fiber itself using a procedure similar to that

reported by Wang et al. (2005). Immediately following headspace extraction of the target sample, a second headspace extraction is made above a sample containing the internal standard. For experiments described in §3.3.2, our chosen internal standard was pure camphene. As with limonene, camphene is a monoterpene with similar structural characteristics. Experimentally, this was accomplished using the post-derivatization option within the Gerstel software (12 second extraction). The same vial containing the internal standard was repeatedly measured throughout the duration of the experiment.

Using this procedure, we observed a non-constant baseline of internal standard measurements. Instead, there appeared to be a direct correlation between internal standard and limonene peak areas. Figure A1 below provides additional data taken from our diC_6PC experiments described in §3.3.2. The positive correlation of peak areas appears to show that the secondary extraction is not independent. Due to this apparent trend, we chose not to pursue using internal standard methods in normalizing our data.

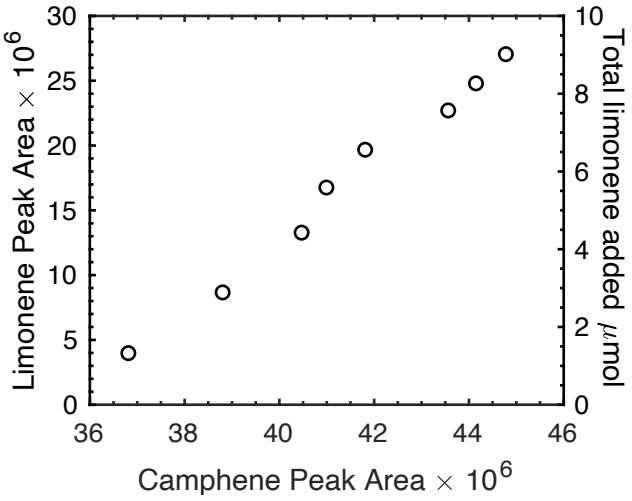

Figure A1. A positive correlation is observed for limonene extractions followed by camphene extractions. V_t was 21.7(±0.2) mL and V_w was 1 mL

Appendix B

Micellar Phase Separation Theory and Fit Parameters Used for Plotting the Phase Diagram for Aqueous diC$_8$PC Solutions

The theory developed by Blankschtein et al. (1985) was used to model the temperature versus mole fraction phase diagram for diC$_8$PC, given in Figure 3.12. This theory incorporates: (1) multiple chemical equilibriums to describe the distribution of aggregates, (2) the entropy of mixing within a solution, and (3) an average mean-field attraction interaction among the aggregates. Using their analysis, they found that a 2nd-order moment linked phase-separation together with self-association behavior.

Then the mole fractions (Z, Y) of the two phases are solved as (Carvalho et al. (1989)):

$$W^5 - \left(\frac{3}{6\gamma - 4}\right)\left(\frac{\gamma C}{k_B T} - 1\right) W^3 - \left(\frac{9}{3\gamma - 2}\right) \exp\left(-\frac{\Delta\mu}{2k_B T}\right) = 0 \qquad B.1$$

$$\begin{pmatrix} Z \\ Y \end{pmatrix} = \frac{1}{4}\left\{ W \pm \left[W^2 - 4\left(\frac{2}{3}W^2 - \left(\frac{1}{3\gamma - 2}\right)(\beta\gamma C - 1)\right)\right]^{\frac{1}{2}}\right\}^2 . \qquad B.2$$

From X-Ray studies of longer chain phospholipids led the authors to choose $\gamma = 30$ (Nagle et al., 1978) leaving only 2 remaining fit parameters, $\Delta\mu/k_B$ and C/k_B, which were found via data fitting techniques. Fit parameters obtained by other research groups are given below.

Table B1. Fit parameters used for creating the diC$_8$PC phase diagram

	$\Delta\mu/k_B$ (K)	C/k_B (K)	γ	T_c (K)[a]
Carvalho et al. (1989)	8600	11.70	30	318.5
Blankschtein et al. (1985)	8100	364/30	30	320
Huang et al. (1990)	8420	357.5/30	30	--

[a] T_c is the reported upper consulate temperature

Appendix C

Critical Micelle Concentrations of Related Surfactants

Table C1. *cmcs* for surfactants presented in Table 4.5 at ambient temperatures (~25°C)

Surfactant	*cmc* (mM)	Reference
diC_6PC	14.6	Tausk et al. (1974)
	13.8	Tausk et al. (1974)
	15.2	Lin et al. (1986)
	16±2	Jonson et al. (1981)
	15	Heerklotz et al. (2001)
diC_7PC	1.42	Tausk et al. (1974)
	1.60	Tausk et al. (1974)
	1.8	Bonsen et al (1972)
	1.9	Heerklotz et al. (2001)
diC_8PC	0.27	Tausk et al. (1974)
	0.25	Tausk et al. (1974)
	0.19	De Haas et al. (1971)
$C_{12}E_6$	0.072	Chen et al. (1998)
	0.087	Corkill et al. (1964)
$C_{12}E_8$	0.084	Chen et al. (1998)
$C_{12}E_9$	0.08	Berthod et al. (2001)
$C_{12}E_{10}$	0.09	Berthod et al. (2001)
$C_{12}E_{12}$	0.1	Berthod et al. (2001)
$C_{12}E_{19}$	—	—
$C_{16}E_{10}$	0.0006	Berthod et al. (2001)
$C_{16}E_{20}$	0.017	Abe et al. (1992)
$C_{16}E_{40}$	—	—
SDS	8.1	Lloyd et al. (2011b)
TTAB	3.79	Evans et al. (1984)